UNIVERSITÀ DI PARMA

UNIVERSITA' DEGLI STUDI DI PARMA

DOTTORATO DI RICERCA IN SCIENZE MEDICO-VETERINARIE

CICLO XXXIII

Indirect oncolysis mediated by Canine Distemper Virus (CDV) Onderstepoort strain affects HIF-1α mediated angiogenesis and triggers mesenchymal to epithelial transition in canine histiocytic sarcoma cells (DH82)

Coordinatore:
Chiar.mo Prof. Gaetano Donofrio

Tutore:
Chiar.mo Prof. Attilio Corradi

Co-Tutore:
Chiar.mo Prof. Wolfgang Baumgärtner

Dottorando: Dr. Federico Armando

Anni Accademici 2017/2018 – 2019/2020

CONTENTS

The researches reported in this PhD thesis were published in international open access peer reviewed scientific journals:

Oxidative Stress in Canine Histiocytic Sarcoma Cells Induced by an Infection with Canine Distemper Virus Led to a Dysregulation of HIF-1α Downstream Pathway Resulting in a Reduced Expression of VEGF-B *In Vitro*

Armando F., Gambini M., Corradi A., Giudice C., Pfankuche V.M., Brogden G., Attig F., von Köckritz-Blickwede M., Baumgärtner W., Puff C.

Viruses 2020, 12, 200; doi:10.3390/v12020200

Mesenchymal to epithelial transition driven by canine distemper virus infection of canine histiocytic sarcoma cells contributes to a reduced cell motility *in vitro*

Armando F., Gambini M., Corradi A., Becker K., Marek K., Pfankuche V.M., Mergani A.E. Brogden G., de Buhr N., von Köckritz-Blickwede M., Baumgärtner W., Puff C.

J Cell Mol Med. 2020; 00:1–17. doi.org/10.1111/jcmm.15585

Federico Armando obtained the permission from the Editors to use any content of the abovementioned pubblications.

ABSTRACT

Histiocytic sarcomas represent malignant tumors, which require new treatment strategies. Canine distemper virus (CDV) is a promising candidate due to its oncolytic features reported in a canine histiocytic sarcoma cell line (DH82 cells). Interestingly, the underlying mechanism might include a dysregulation of angiogenesis. Moreover, tumors undergoing mesenchymal to epithelial transition (MET) are often associated with a favourable clinical outcome. This process is characterized by an increased expression of epithelial markers leading to a decreased invasion and metastatic rate. Based on these informations two main hypothesis have been formulated and addressed in two independent *in vitro* studies. The first *in vitro* study hypothesized that a persistent CDV-Ond infection of DH82 cells induces oxidative stress followed by a massive inhibition of HIF-1α degrading pathways. This in turn leads to cytoplasmic, non-functional accumulation of HIF-1α, which is associated with a reduced expression of HIF-1α downstream targets, such as VEGF-B. The second *in vitro* study hypothesizes that a CDV infection of canine histiocytic sarcoma cells (DH82 cells) triggers the MET process leading to a decreased cellular motility. Within the first *in vitro* study, microarray data analysis, immunofluorescence for 8-hydroxyguanosine, superoxide dismutase 2 and catalase, and flow cytometry for oxidative burst displayed an increased oxidative stress in persistently CDV-infected DH82 cells (DH82Ond pi) compared to controls. The HIF-1 α expression in DH82Ond pi increased, as demonstrated by Western blot, and showed an unexpected, often sub-membranous distribution, as shown by immunofluorescence and immunoelectron microscopy. Furthermore, microarray data analysis and immunofluorescence confirmed a reduced expression of VEGF-B in DH82Ond pi compared to controls. Within the second *in vitro* study, immunofluorescence and immunoblotting were used to investigate the expression of epithelial and mesenchymal markers followed by scratch assay and an invasion assay as functional confirmation. Furthermore, microarray data were analysed for genes associated with the MET process, invasion and angiogenesis. CDV-infected cells exhibited an increased expression of epithelial markers such as E-cadherin and cytokeratin 8 compared to controls, indicating a MET process. This was accompanied by a reduced cell motility and invasiveness. In summary, the first study results suggest a reduced activation of the HIF-1 α angiogenic downstream pathway in DH82Ond pi cells in vitro, most likely due to an excessive, unusually localized, and non-functional expression of HIF-1 α triggered by a CDV-induced increased oxidative stress. Summarized, ,the second study results suggest that CDV infection of DH82 cells triggers the MET process by an increased expression of epithelial markers resulting in a decreased cell motility *in vitro.*

RIASSUNTO

Il sarcoma istiocitico è un tumore maligno che è in forte richiesta di nuove strategie terapeutiche. A tale proposito, il virus del cimurro del cane (CDV) rappresenta un candidato promettente grazie alle sue proprietà oncolitiche riportate in una linea cellulare di sarcoma istiocitico canino (DH82). È degno di nota il fatto che il meccanismo sottostante possa includere l'alterata regolazione dell'angiogenesi. Inoltre, i tumori che vanno incontro alla transizione mesenchimale-epiteliale (MET) sono spesso associati ad un esito clinico favorevole. Questo fenomeno è carattarizzato da una incrementata espressione di markers epiteliali, comportando una diminiuita invasività e capacità metastatica. Sulla base di queste informazioni sono state formulate due ipotesi principali nel corso di due esperimenti *in vitro* indipendenti. Il primo esperimento ipotizza che una infezione persistente delle cellule DH82 con CDV-Ond induce uno stress ossidativo, seguito da una massiva inibizione della degradazione di HIF-1α. Questo a sua volta comporta un accumulo citoplasmatico non funzionale di HIF-1α, il quale è associato con una ridotta espressione dei target finali del pathway di HIF-1α come ad esempio VEGF-B. Il secondo esperimento ipotizza che l'infezione da CDV nelle cellule di sarcoma istiocitico canino scatena il fenomeno della MET comportando una ridotta motilità cellulare. All'interno del primo esperimento, l'analisi dei dati in microarray, immunofluorescenza per 8-idrossiguanosina, superossido dismutasi 2 e catalasi, citometri a flusso per la determinazione del burst ossidativo mostrano un aumentato stress ossidativo all'interno delle cellule persistentemente infettate con CDV-Ond (DH82Ond pi) rispetto ai controlli. L'aumentata espressione di HIF-1α nelle cellule DH82Ond pi, come dimostrato dal western blot, ha rivelato una distribuzione inaspettata e spesso sub-membranaria, come dimostrao dall'immunofluorescenza e l'immunoelettronmicroscopia. Inoltre, microarray e immunofluorescenza confermano la ridotta espressione di VEGF-B nelle cellule DH82Ond pi rispetto ai controlli non infetti. All'interno del secondo esperimento, western blot e immunofluorescenza sono stati usati per investigare l'espressione di markers epiteliali e mesenchimali seguite da uno "scratch assay" e da un "invasion assay" in modo da ottenere una conferma funzionale. Inoltre, il microarray è stato analizzato per geni associati con il fenomeno della MET e invasione ed angiogenesi. Le cellule infettate con CDV mostrarono un'aumentata espressione di markers epiteliali come E-caderina e citokeratina 8 rispetto ai controlli, suggerendo un processo di MET. Tale processo era accompagnato da una ridotta motilità cellulare ed invasività. Riassumendo, i risultati del primo studio suggeriscono una ridotta ativazione dei target del pathway angiogenetico del HIF-1 α *in vitro* nelle cellule DH82Ond pi, probabilmente dovuto ad una eccessiva, insolita e non funzionale espressione di HIF-1 α stimolata da un incrementato stress ossidativo CDV-indotto. Riassumendo, i risultati del secondo studio suggeriscono che l'infezione da CDV stimola il fenomeno della MET grazie ad un' aumentata espressione di markers epiteliali comportando una diminuita motilità cellulare *in vitro.*

1.0 CANINE HISTIOCYTIC DISORDERS

The term “histiocyte” has been generically used to describe cells of dendritic cell (DC) or macrophage lineage. However, histiocytes differentiate from stem cell precursor $CD34^{+}$ into macrophages and numerous DC lineages(1). Interestingly, histiocytic disease are reported to occur with higher frequency in dogs than in cats and the majority of canine histiocytic disease comes from proliferations of cells of various DC lineages (2). Langerhans cells (LCs) are Intraepithelial DCs and the canine histiocytomas originate from cells exhibiting LC differentiation. On the other hand, from the proliferation of activated interstitial DCs arise both the cutaneous histiocytosis and systemic histiocytosis, belonging to the reactive histiocytoses classification (1). Moreover, interstitial DCs may occur in perivascular locations in many different organs, only brain meninges, and brain choroid plexus (3) and the majority of histiocytic sarcomas originate from cells exhibiting interstitial DC differentiation (1).

1.1 Canine cutaneous histiocytoma

Canine Cutaneous histiocytoma (CCH) usually occur as a solitary, benign neoplasm with a rapid growth, alopecic, erythematous, dome-shaped nodule, often with ulceration (4–8). CCH represents one of the few naturally occurring neoplasms that display spontaneous regression(9).Many CCH bearing dogs are less than 3 years old, but these tumors can develop at any age (10,1). CCHs predominantly arise on the head, pinnae and limbs (6,9,11,12). Although it occurs in all breeds, boxers, bulldogs, Scottish terriers, Doberman pinschers, cocker spaniels, and dachshunds are reported to have a significantly higher risk than all other breeds (6,11). These tumors grossly appear as a well-circumscribed lesions of diameter 0.2 - 4 cm (11). Microscopically, they are characterized by non-encapsulated growth of histiocytic cells often with invasion of the overlying epidermis and with secondary epidermal ulceration (11). Although the rapid growth and high mitotic index suggest malignancy, CCH is a benign tumor that occur in spontaneous regression (within a few weeks or months) within the natural course of the disease (4,13,14). Neoplastic cells in CCH are considered to originate from Langerhans cells (LCs) (15). They express CD1a, CD11a/CD18, CD11c/CD18, CD44, CD45, MHC class II and high levels of E-cadherin (1,16).

1.2.0 Canine reactive histiocytoses

Canine reactive histiocytoses are described in dogs and include: i) cutaneous histiocytosis (CH) which is more common and affects the skin extending into draining lymph nodes; and ii) systemic histiocytosis (SH) which is rarer and has similar skin lesions, but can extend into other organs (1). The lesion topography, histiocytic cells immunophenotype and the clinical behavior are similar between CH and SH (17). Microscopically they are characterized by angiocentric infiltrates mainly composed by activated dermal DCs, T cells and neutrophils forming multifocal perivascular cuffs(1). The multifocal lesions tend to be coalescing forming masses, especially in the deep dermis and panniculus. Therefore they have a "Bottom-heavy" appearance pattern, that should be well differentiated by the "top-heavy" pattern of the CCH (1). The etiology and pathogenesis of canine reactive histiocytosis is unknown but an immune dysregulatory mechanisms are likely to be involved in the pathogenesis of this disease indeed it regress with systemic immunosuppressive therapy (17).

1.2.1 Canine cutaneous histiocytosis

Cutaneous histiocytosis (CH) is an inflammatory, lymphohistiocytic, proliferative, reactive disorder that primarily involves skin, subcutis and local lymph nodes but does not extend beyond the local draining lymph nodes (1,18). No clear breed predisposition has been reported (1,18). Lesions consist of multiple (solitary nodules are uncommon) cutaneous and subcutaneous nodules that might also be ulcerated. The most common locations of these lesions are nose, face, neck, trunk, extremities, scrotum, and perineum (1,18). Lesions usually regress spontaneously and appear at new sites simultaneously (1). Microscopically, histiocytic cells, lymphocytes, variable numbers of neutrophils, eosinophils, and plasma cells characterize the perivascular infiltrates typical of this lesion(19).

1.2.2 Canine sistemic histiocytosis

Systemic histiocytosis (SH) is a generalized histiocytic proliferative disease with a marked tendency to involve skin, nasal, ocular mucosae and peripheral lymph nodes (1). This disease was first described in closely related Bernese Mountain Dogs (20), other breeds result to be less commonly affected such as Rottweiler, Labrador Retriever, Basset Hound, Irish Wolfhound

(1). In particular, the SH course is characterize by periods of remission and relapses (1). The disease occurs as multiple cutaneous nodules affecting large areas of the body (1). Microscopically, lesions consist of angiocentric infiltrates of numerous histiocytes and fewer lymphocytes, neutrophils, and eosinophils (20).

1.3 Canine histiocytic sarcoma complex

Canine histiocytic sarcoma (CHS) is a highly malignant neoplasm (21). Given that, interstitial DCs might have a ubiquitous distribution, CHS can potentially arise in any tissue (1). CHS are known to be localized or disseminated (1). Localized CHS arise from a single tissue site or in a single organ while once the neoplastic cells spread beyond the draining lymph node involving distant sites, this should be considered as disseminated CHS (1). CHS complex were first recognized in Bernese Mountain Dogs, in which was apparent a possible familial association (21,22). Besides Bernese Mountain Dogs several others breeds resulted to be predisposed to develop CHS, such as Rottweilers, Flat-Coated Retrievers, Golden Retrievers, and Pembroke Welsh Corgis (17,23). Spleen, liver, lymph nodes, lung, bone marrow, central nervous system, skin, subcutis, and in periarticular and articular tissues of the limbs are the most common sites were CHS lesions are typically found (6).

Grossly, lesions occurs as a solitary or multiple, nodular, white to yellowish, firm masses with a uniform, smooth cut surface and are characterized by an infiltrative growth (1).

Microscopically, neoplasms consist of densely cellular, poorly demarcated sheets of large, highly pleomorphic, often multinucleated cells. Cellular and nuclear atypia are usually marked. The mitotic index is high, often atypical mitoses are also reported (1).

Several chemotherapeutic drugs have been applied for the treatment of HS, such as doxorubicin and paclitaxel (24). Even if is often ineffective, systemic chemotherapy is used for disseminated CHS treatment. On the other hand, localized CHS are usually treated using surgery along with radiation therapy (6).

In the end, localized CHS forms are reported to have a more favorable prognosis, while the disseminated CHS forms bear a poorer prognosis (6). However, usually dogs are euthanized in the early disease course regardless the two CHS forms because of the early aggressive clinical behavior(6).

2.0 VIRAL ONCOLYSIS

Cancer in dogs is the most common cause of natural death (25). Among the more frequently used therapeutical solutions are reported chemotherapy, surgery, radiation therapy, and photodynamic therapy (26). Given that, standard therapy is usually palliative in canine cancer there is a strong need to evaluate alternative approaches. Therefore, the oncolytic virotheraphy might represent a promising approach based on the evidences that oncolytic viruses selectively infect and destroy cancer cells sparing healthy cells (26).

2.1 History of oncolytic virotherapy

Since the early 20th century The possibility to use viruses to eradicate cancer was known (27–29).One of the very first promising result was obtained using a vaccine strain of rabies virus in a clinical study treating 30 patients with melanomatosis, 8 of whom showed a tumor regression (30). Years later, the oncolytic efficacy of several others viruses was tested in humans such as, adenovirus serotype type 4, (31), West Nile virus (strain Egypt 101) (29), mumps, and Newcastle disease virus (NDV) (32,33). Even if these studies were very promising for a pioneeristic approach in cancer therapy, the virotherapy efficacy was unimpressive and many viruses related side-effects caused the end of the trials. Therefore, the interest in viruses as anti-cancer agents dramatically decreased during the following years.

Later in the 1990s, the interest in viruses employed in cancer therapy was recalibrated thanks to the increasing knowledge of the modern biotechnology and the concept of gene therapy (34).

Interestingly, since the beginning of the 21st century several reports suggested that intratumorally or systemically delivered viruses such as Newcastle disease virus (NDV) (35), reovirus (36), lentivirus (37), herpes simplex virus (HSV)(38), enterovirus (39), Sindbis virus (40), Semliki Forest virus (41), Seneca Valley virus (42), vaccinia virus (43), myxoma (44), and raccoonpox virus (45) can show an antitumor activity in different animal models. Oncolytic viruses such as various human and canine adenoviruses, canine distemper virus (CDV) and vaccinia virus strains have been preclinically tested for canine cancer therapy(26).

In contrast to the progress of human oncolytic virotherapy, there are very few clinical trials using oncolytic viruses for canine or feline cancer patients (26,46). However, it is reasonable to expect that the human clinical protocols could be suitable also for those of pet cancer patients considering that several forms of canine or feline neoplasms resemble histologically, genetically and clinically their human counterparts (47–50). Indeed, strong similarities between naturally occurring human and canine cancers have been reported, including colorectal carcinoma, fibrosarcoma, osteosarcoma, soft tissue sarcoma, Non-Hodgkin and Burkitt lymphomas and small lymphocytic lymphoma (51). Moreover, also feline cancers showed similarities in tumor biology and prognosis with human head and neck squamous cell carcinoma and a wide subset of breast cancers (52,53).

Taking into consideration these similarities between human cancers and their animals counterparts, it is reasonable to believe that soon oncolytic virotherapy will be a reality also in veterinary medicine. Moreover, the data from canine studies may be helpful in designing human clinical trials. The translation of oncolytic virotherapy from dogs to humans and the reverse could also be a two-way

street for development of drugs (54).

2.2 Viral oncolysis mechanisms

Oncolytic viruses lead to tumor regression causing cells destruction via several different ways considered as primary and secondary mechanisms (Fig. 1). Among the primary mechanisms, it should be included transcription of viral genome and virus release, which subsequently triggers cellular defense mechanisms causing tumor cell necrosis and apoptosis while among the secondary mechanism, virucidal immune reactions and alterations within the tumor microenvironment such as angiogenesis impairment are reported (55). Interestingly, several studies demonstrated the ability of measles virus to induce apoptotic mechanism within tumor cells (56,57). Moreover, it has been suggested that, depending on the virus strain used, another potential primary mechanism of virus mediate oncolysis might be based on overwhelming budding and release of virions from the infected tumor cell leading to tumor cell lysis (58). In addition to the direct effect on tumor cell, the viral infection might cause tumor cells lysis by the innate and adaptive immune responses following attraction of immune cells. Tumor associated macrophages (TAMs), which according to M1 or M2 polarization possess a bivalent role in relation to tumor development, have been reported to play a pivotal role in cancer development. It is well reported that TAMs within a tumor microenviroment are predominantly polarized towards the M2-phenotype (59–61). Therefore, it has been suggested that using oncolytic viruses for reprograming M2-tumor associated macrophages towards the tumoricidal and angiostatic M1-phenotype might represents a promising secondary effect caused by oncolytic viruses (62,63). Moreover, antiviral cytokines, such as interferon (IFN)-γ and interleukin (IL)-12, are produced in response to pathogen associated molecular pattern (PAMP) and represent strong initiators of an M1 macrophage response (64,65). Therefore, a tumor cells infected by an oncolytic virus produce high levels of IFN-γ and IL-12 that might lead to a M1-macrophage accumulation resulting in tumoricidal factors and proinflammatory cytokines secretion within tumor microenvironment. The same PAMP-induced cytokines may also initiate the down-stream complex interplay between IFN-γ, IL-12, natural killer cells and 'angiotoxic' interferon- γ-inducible protein (IP-10) to eventually depress tumor angiogenesis, thus limit tumor growth, and induce tumor regression, respectively (66–68). To further substantiate the effective anti-tumor capacity of IP-10 ad IL-12 it should be considered that it has been demonstrated that these two chemokine s inhibit basic fibroblast growth factor (bFGF), known as an important pro-angiogenic protein (69,70). Interestingly, another approach that might benefit from the immune response against tumor cells is tumor vaccination or cancer immunotherapy. This technique aim at evoking tumor-specific immunity able to eradicate tumors as well as maintaining memory (28,71,72). Tumor specific immunity may be stimulated either via opsonization of tumor cells by antibodies produced by viral vectors expressing particular tumor specific antigens or by the production of tumor associated antigens (TAAs) within tumor cells or in other cells (34).

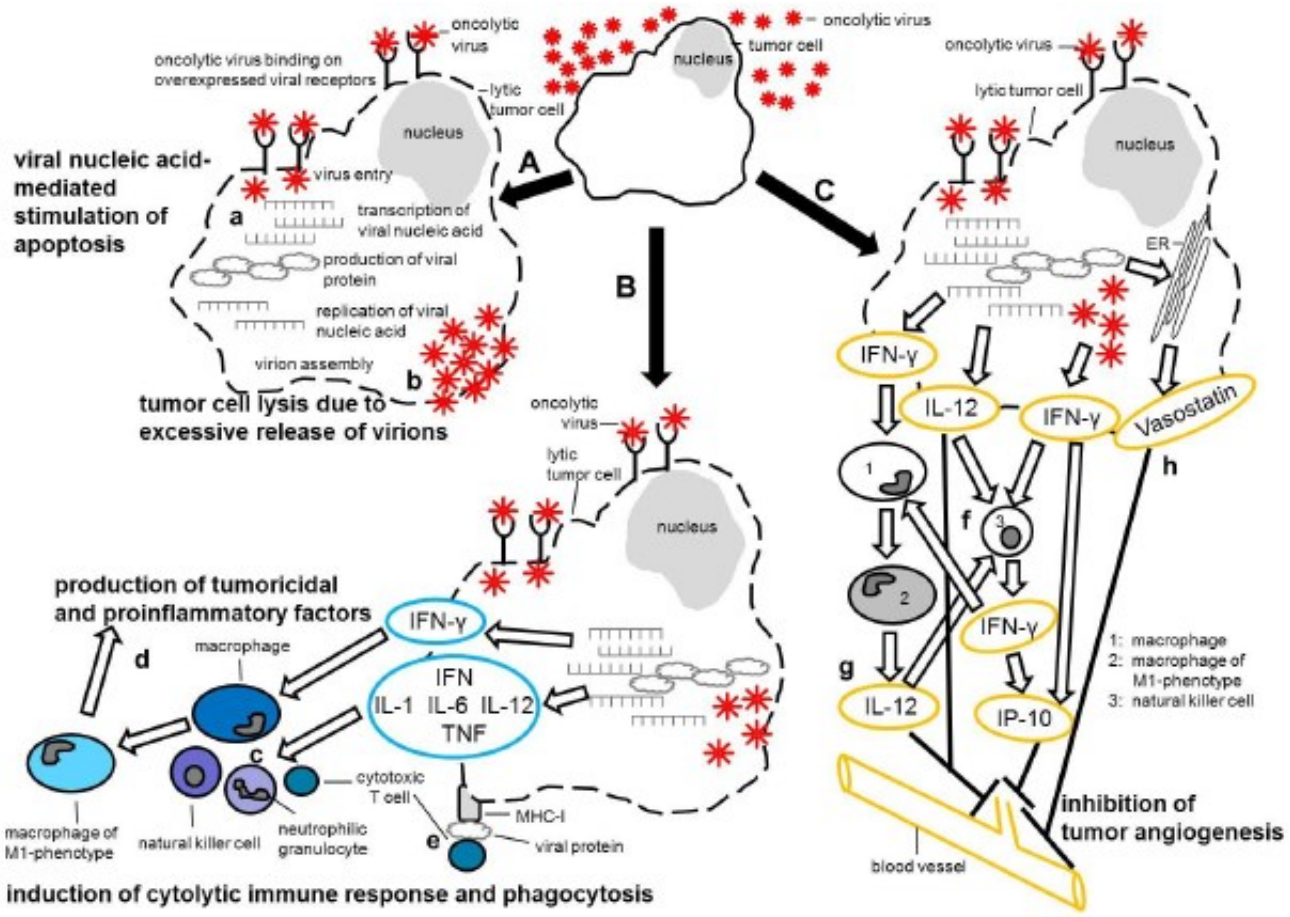

Figure 1: Potential mechanisms leading to tumor cell destruction upon infection with an oncolytic virus. From Lapp et al. 2014.

2.3 *Paramyxoviridae* as oncolytic viruses

Paramyxoviradae include a vast group of viruses with many prototypic members that have been extensively used in cancer targeting such as measles virus, mumps virus and the Newcastle disease virus (NDV) (34).

The first use of NDV as an oncolytic agent in humans began in 1965 with a clinical trial led by Dr's Cassel and Garrett, who treated a patient with cervical carcinoma using the live attenuated 73-T strain (73). Afterwards, another study used a purified poultry vaccine dubbed MTH-68/H based on live attenuated NDV and it was administered intravenously to a total of 14 patients with grade IV glioblastoma multiforme (74). Interestingly, 7 were alive for 8 years after treatment, while 5 died of the cancer and 2 died of other causes. Moreover, based on the promising results obtained from the numerous animal experiments and clinical trials, it seems that NDV is an extremely safe oncolytic agent (28).

Another *paramyxovirus* belonging to genus Rubulavirus that had been tested in humans is Mumps virus. Ninety patients with different malignancies, were treated using Mumps, Urabe strain and have been reported partial or complete responses in 37 cases. Subsequently, more attenuated strains have been developed due to CNS complication in up to 1% of vaccinated individuals caused by the live Urabe vaccine strain (75). Interestingly, another promising mumps virus is the live attenuated vaccine strain S79 that showed significant results as an oncolytic vehicle based on its selective infection of cancer cells *in vitro* and in nude mice (76).

Measles virus (MV), which belongs as well to *paramyxovirus*, have been reported to cause Hodgkin's disease regression in children after a natural infection (77). Since that time, MV has been used to target lymphoid tumors taking advantage of its natural tropism for CD150 or SLAM receptors. Using both a parental virus and a recombinant vector based on the Edmonston B strain, human lymphoma xenografts in SCID mice showed an inhibited growth by either Intrathecal and intravenous injections (78). Interestingly, Peng and colleagues later demonstrated the possibility to also use recombinant measles vectors to preferentially infect and destroy human epithelial ovarian cancer cells *in vivo* via CD46 receptor (79). Afterwards, also other MV vectors have been employed to target and destroy myeloma, cutaneous T-cell lymphomas, and ovarian cancers (80). Is noteworthy that a study described another *paramyxovirus*, namely Senday virus (genus: respirovirus) to be able to infect and kill different cancer types both *in vitro* and *in vivo* in nude mice xenograft model for human fibrosarcoma and colorectal adenocarcinoma (81). In the end we can state that many paramyxoviruses display a remarkable potential as anti-cancer agents showing promising result to be employed in

oncolytic virotherapy.

2.4 Canine distemper virus

Another virus belonging to *paramyxoviridae* family, *morbillivirus* genus that displayed very promising results in oncolytic virotherapy, especially in veterinary medicine, is canine distemper virus (CDV). CDV is an enveloped single stranded RNA virus that is closely related to MV(82). Interestingly, CD46, CD150, and nectin-4 have also been described to be cellular receptors for CDV similar to those one used by MV (83–85). As a consequence, CDV entry into immune cells is controlled by the hemagglutinin glycoprotein interacting predominantly with cellular CD150 as happen also during MV infection (86,87). Thanks to this aforementioned, CDV has been considered for treatment of canine lymphoma. Neoplastic canine B and T lymphocytes over-express signaling lymphocyte activation molecule (SLAM or CD150) on which CDV binds (84,88). Interestingly an attenuated CDV strain was able to infect canine lymphoma cells *in vitro* via bindings CD150 and to induce apoptosis (84)**.** These promising results, even if still preliminary, support the fact on focusing research in CDV for the treatment of canine lymphoma. However, we have also to take into consideration that the biggest problem about the use of CDV in canine clinical trials is about the fact that most of the dogs are vaccinated against CDV. In order to avoid the pre-existing immunity it might be useful to use vectors of non-canine origins or removing from the viral capsid the key neutralizing epitopes of CDV. Morevoer, mucosal or even intratumoral injection or administration of higher virus doses could also be a solution to avoid pre-existing immunity (88). During the last years, the attenuated Onderstepoort vaccine CDV strain displayed also promising results infecting *in vitro* a canine histiocytic sarcoma cell line (DH82) (89,90). Infecting DH82 cells with CDV-Onderstepoort(Ond) it resulted to be a good model for the viral oncolysis investigations (91–93). Specifically, acute infection of DH82 cells with CDV-Ond in vitro resulted in a prominent cell death at 12 days post infection (90), followed by establishment of persistent infection in tumor cells surviving the acute lytic phase (89). Interestingly, subcutaneous xenograft of persistently CDV-Ond infected DH82 cells resulted in a complete tumor regression in a SCID mice model (89). These promising and interesting findings was hypothesized to be related with a likely decrease of tumor associate vascularization, with a not completely understood underlying mechanism. Moreover CDV-Ond demonstrated the ability also to influence the expression of reversion-inducing cysteine-rich protein with Kazal motifs (RECK), matrix metalloproteinases (MMP) −2 and −9 and tissue inhibitors of matrix metalloproteinases (TIMP) −1 and −2, (91) altering cortactin distribution within the cytoskeleton (92). Taken together, these different findings provide strong evidences to confirm CDV-Ond as a promising candidate for oncolytic virotherapy against canine histiocytic sarcomas in dogs allowing also to use it as a model for the corresponding human

disease.

3.0 TUMOR ASSOCIATED ANGIOGENESIS

Tumors, like normal tissues, have a strong need of nutrients and oxygen (O_2) as well as they need to eliminate metabolic wastes and carbon dioxide (CO_2). In order to provide to these necessities the process of angiogenesis generates the tumor-associated neovasculature. Interestingly, an "angiogenic switch" is almost always activated during tumor progression and remains on. This process cause the normally quiescent vasculature to continually sprout new vessels favoring fast tumor growths (94). It has been suggested that this angiogenic switch is orchestrated by compensative different factors that might either induce or stop angiogenesis (95,96). Vascular endothelial growth factors (VEGFs) and thrombospondin-1 (TSP-1) are well known molecules, which induce or inhibit angiogenesis, respectively. Interestingly, VEGF gene expression can be upregulated by oncogene signaling and also by hypoxia(97–99). It was believed that angiogenesis plays an important role only when rapidly growing macroscopic tumors had formed, but nowadays it is well established that angiogenesis also contributes to the microscopic phase of neoplastic progression. During tumor growth, the rapid cellular division can enhance O_2 demand, most likely causing localized hypoxia (100).

In particular, a reduced vascularization within the tumor often leads to intratumoral hypoxia (101) associated with intracellular pathways connected with reactive oxygen species (ROS) scavenging and production. ROS are highly chemically reactive molecules that, when they outnumber the scavenging systems, can alter other cellular macromolecules as lipids and nucleic acid (102–104). Nevertheless, ROS are normally involved in different intracellular signaling pathways (103,104) and play a key role also in several hallmarks of cancer (105). Interestingly, also infection with oncolytic viruses have been reported to increase ROS production, for example CDV infection can increase ROS-induced damage and ROS production both *in vitro* and *in vivo* as already demonstrated for spontaneous CDV infections in dogs (106–110).

3.1 The master regulator of angiogenesis: HIF-1α

The founding member of hypoxia-inducible factor (HIF) family, namely HIF-1α, regulates a vast plethora of genes in response to hypoxia (111–113). HIF proteins belong to the bHLH-PAS (basic helix loop helix-Per/ARNT/Sim) family(114) and consist of 3 α-subunits that are O_2regulated, namely HIF-1α, HIF-2α, and HIF-3α moreover there is a constitutively expressed subunit of the Aryl hydrocarbon nuclear translocator family, including Arnt, Arnt2, and Arnt3. The Prolyl hydroxylase enzymes (PH1-3) regulate HIF pathway activity. In an oxygen and 2-oxoglutarate dependent manner, PHD enzymes hydroxylate HIF-α on 2 conserved proline residues founded in the O2-dependent degradation domain (ODDD). As a consequence, proline hydroxylation allow the binding to the von Hippel–Lindau E3 ubiquitin ligase complex that ubiquitinates HIF-α, in order to target it for proteasomal final degradation. Under Hypoxic conditions HIF-α hydroxylation is attenuated, resulting in an intracellular accumulation (115). Afterwards, HIF-α translocates into the nucleus binding to Arnt and forming a transcriptional complex with p300 and CBP through the HIF-α N- and C-terminal transactivation domain (N-, C-TAD) interactions(116,117). Finally, HIF-α/Arnt complex binds to the hypoxia response elements (HREs)(118). Interestingly, HIF-α phosphorylation can also regulate its stability and activity in a positive or negative manner(119). Several factors might influence HIF-α transcriptional activity, for example SUMO-1 sumoylates Arnt and HIF-1α on conserved lysine residues (120) and S-nitrosylation (on cysteine 522 and 800) increases the binding of HIF-1α with coactivators CBP and p300, increasing HIF-1α transcriptional activity (121). Although low O_2 is reported to be the main HIF activity regulator, it is likely that also other signals influence HIF-α stability and functions. Environmental stress, Ionizing radiation, and angiopoietin-2 induce HIF-1α stabilization through the production of reactive oxygen species (ROS). Primary cellular responses to O_2 are mediated by HIF pathway, which promotes both short and long term adaptation mechanisms to hypoxia. The short term adaptation mechanisms includes for example an upregulation of the vasodilatatory enzyme inducible nitric oxide synthase (iNOS) that contribute to a rapid O_2 increase (122). On the other hand, long term adaptation can be primarily achieved by stimulating angiogenesis. Indeed, the HIF pathway regulates several pro-angiogenic genes such as vascular endothelial growth factor (VEGF), angiopoiein-1, angiopoietin-2, Tie2, platelet derived growth factor (PDGF), basic fibroblasts growth factor (bFGF), and monocyte chemoattractant protein-1 (MCP-1). Moreover, HIF-regulated pro-angiogenic factors execute the HIFspecific angiogenic program by increasing vascular permeability, endothelial cell proliferation, sprouting, migration, adhesion, and tube formation. Interestingly, in absence of additional factors, an ectopic stimulation of the HIF pathway is enough for inducing localized angiogenesis (123). The multitude of pro-angiogenic HIF target genes and

the complex angiogenic process regulated by them make HIF-1α the “master regulator” of angiogenesis (Fig. 2) (124).

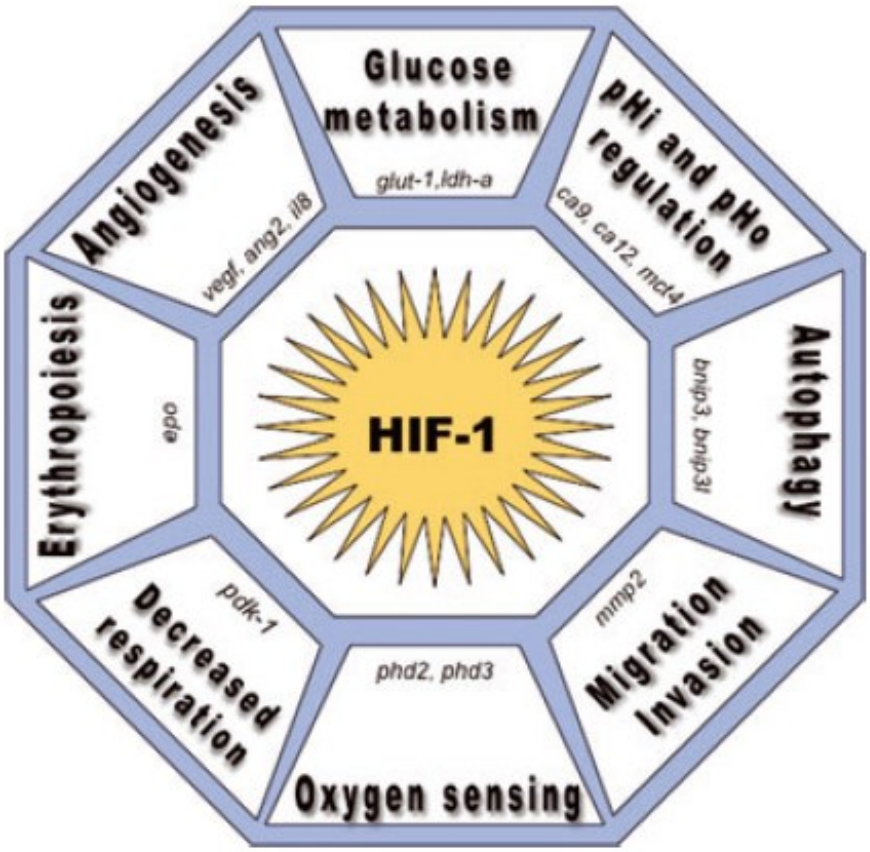

Figure 2 HIF-1α mediates microenvironmental changes and cellular adaptation to tumor hypoxia. From Chiche et al. 2010

3.2 HIF-1α and tumor angiogenesis

During tumor malignant progression, the early phase might be characterized by no angiogenic stimuli resulting in an avascular area where the apoptotic cells are replaced by the fast proliferating ones. Afterwards, the so-called "angiogenic switch" occurs and a state of active vessel growth begin (125). Angiogenesis is considered critical for tumor growth and progression. Interestingly, the early inhibition of angiogenesis impaired tumor progression in several tumor models (126). Despite the intense tumor angiogenetic activity, tumor vessels are leaky, highly irregular, and poorly functioning, leading to a HIF-α stabilization due to hypoxia even in densely vascular tumors. Moreover, other tumor factors related with malignant progression such as Ras pathway hyperactivation, p53 mutation and succinate accumulation could stabilize HIF-α independently of hypoxia (127–129).

The VEGF, Ang-1, Ang-2, and Tie-2 expression, and many others genes, are regulated by HIF-1α and HIF- 2α. Interestingly, was demonstrated that HIF-1α directly regulates VEGF expression *in vivo* in Hepa-1 xenografts, while Hepa-1 cells with defective Arnt resulted in poorly vascularized tumors with a reduced VEGF expression (130). Even if also the other HIF transcriptional targets are important for the complete effect of HIF on vascular biology, VEGF expression is considered the primary effector for the HIF angiogenic properties. Tumor vascular development may involve not only angiogenesis but also vasculogenesis, which is less well understood. Bone-marrow derived cells are recruited to vasculogenesis sites via ligand stromal derived factor–1 (SDF-1) and its cognate receptor C-X-C chemokine receptor 4 (CXCR4) (131). In fact, SDF-1 resulted to be an HIF-1α transcriptional target and a pharmacological inhibition of the SDF-1/CXCR4 signaling led to a decreased vascular regrowth after glioblastoma tumor irradiation (131,132). Is noteworthy that also inhibition of HIF-1α led to a similar result, overall suggesting that hypoxia plays a pivotal role in tumor vasculogenesis.

Moreover, tumor associated macrophages (TAMs) are also recruited in order to increase the active angiogenesis/vasculogenesis promoting tumor invasion and metastasis. TAMs might be recruited into an hypoxic tumor rea by HIF target genes such as, VEGF, FGFS, and MCP-1 (133). HIF-1α regulates the glycolytic phenotype of TAMs and promotes migration, invasion, and aggregation of TAMs at inflammatory sites; therefore, HIF-1α may also play a role in TAM mediated angiogenesis (134).

4.0 Epithelial to Mesenchymal transition (EMT) in carcinomas

Epithelial to Mesenchymal Transition is a cellular mechanism involved in different processes in which epithelial polarized cells are modified by several genetic changes regulated by specific genes in order to obtain a mesenchymal phenotype (135). EMT consist of a E-cadherin suppression and a so-called "cadherin switch", changing to the expression of mesenchymal cadherins such as N-cadherin (136). The main aspect of this process is the E-cadherin inhibition, the major mediator of cell adhesion in adherens Junctions. The main functional difference between epithelial and mesenchymal adherens junctions is their inter-cellular stability: epithelial ones are stable in the range of hours to days, whereas mesenchymal ones are transient (minutes to hours) (137). During EMT process, tight junctions proteins are relocalized and/or degraded. The dissolution of tight junctions during EMT is accompanied by decreased claudin and occludin expression, and the diffusion of zonula occludens 1 (ZO1) from cell–cell contacts (138). EMT can be either total or partial, and there can be subsequent cycles of EMT and its reverse process, MET (mesenchymal to epithelial transition). Research has widely described this event in many different moments of embryogenesis, fibrosis and cancer development (139).

4.1 EMT regulation

EMT "Master gene regulators" include Zeb, TWIST, SNAIL, Slug (140). Interestingly, there are multiple reciprocal networks between transcription factors (TFs) and between TFs and miRNAs, regulating EMT(141). E-cadherin is a protein of the cadherins family, that mediate calcium dependent cell-cell adhesion, functioning as key molecules in the morphogenesis of a variety of organs (142). E-cadherin is typical of epithelial tissues, and behaves as a tumor suppressor gene and plays different roles in regulating cell polarity, differentiation, migration and stem cell-like properties (142,143). E-cadherin is regulated by the gene CDH-1 (135), and one of the main mechanisms for E-cadherin loss involves CDH-1 repression by EMT transcritption factors (144).

4.1.1 Snail

Snail family members are zinc finger transcriptional repressors, including Snail1 (Snail) and Snail2 (Slug); their main role in EMT is the suppression of E-cadherin(145). The gene regulating Snail1 is SNAI1, the activity of which is stimulated for example by NF-kB (146), protein kinase Akt (147), and in some cases erythropoietin (148).

Snail1 and Snail2 are induced by a variety of pathways such as TGF-β(149), Wnt pathways (150,151), reactive oxygen species (152) and hypoxic stress (153,154). There are also Snail2 repressors, as in the case of mammary gland metastasis, where Singleminded-2 (SIM2s) and ELF5, was shown to directly bind to the Snail2 promoter to inhibit its transcription (155,156). Interestingly, both SIM2s and ELF5 are essential for mammary gland ductal development or alveologenesis during pregnancy, and both are frequently lost during breast cancer development (155,156). It is of note that not all Snail family members trigger EMT with the same effectiveness (157). Snail family members not only repress CDH-1 gene but also other epithelial markers, such as claudins 1, 3, 4, 7, occludins, cytokeratins and mucins (158).

4.1.2 Twist-1

Twist-related protein 1 (TWIST1) is a basic helix-loop-helix transcription factor encoded by the TWIST1 gene(159), has a basic domain interacting with core E-box sequence 'CANNTG,' a helix–loop–helix (HLH) domain that mediates homodimerization or dimerization with E12/E47, and a highly conserved C-terminal domain, called "Twist box"(160). Twist is implicated in multiple epithelial cancers through its EMT promoting function, and it was shown to correlate

with poor prognosis and invasiveness(161,162). Interestingly, Twist1 represses E-cadherin not only binding CDH-1, but also inducing Snail1 or Snail2 (163).

4.1.3 Zeb

Zeb family comprises ZEB1 and ZEB2, containing multiple independent domains to interact with other transcriptional regulators (164) and trigger an EMT process by repression of epithelial markers and activation of mesenchymal ones (165,166). ZEB1 and ZEB2 activate N-cadherin and Vimentin expression, mesenchymal phenotype markers, and repress E-cadherin through binding to the E-boxes of CDH-1 promoter region and recruiting corepressors(167). Nicotinamide adenine dinucleotide-dependent histone deacetylase (SIRT1) is recruited by ZEB1 to repress the E-cadherin promoter and induces ZEB and Snail factors but not Twist (168).

4.2 EMT in embryonic life

EMT is an important mechanism in different steps of embryogenesis, as most of the tissues undergo different cycles of EMT and its reverse program, the so-called Mesenchymal to Epithelial Transition (MET) (135). One of the first step of embryonic life is gastrulation, that is the formation of three embryonic germ layers. These are the ectoderm, mesoderm and endoderm, originating from the epiblast, the first epithelial germ layer. In gastrulation the ectoderm is positioned outside, the mesoderm in the middle and the inner layer becomes the endoderm. Thanks to an EMT process, mesodermal and endodermal cells detach from the outer epiblast and are internalized (169). Later on, also other tissues during embryogenesis need EMT to develop properly, as kidneys. In order to obtain a functional kidney, multiple rounds of EMT and MET have to take place (170). Another example of EMT during embryogenesis is in cardiac tissue development, in which some of its main signaling pathways such as Notch, Bmp2 and Wnt/β-catenin, drive a primary EMT (171–174). The cardiac valve formation follows a different path, thanks to a very similar process called Endothelial to Mesenchymal Transition (EndoMT), in which endothelial cells detach from vessels and, to various extents, gain mesenchymal phenotype (175). Interestingly, it has been showed the occurrence of the reverse process, MET, during revascularization of myocardium by cardiac fibroblast after ischemic cardiac injury (176).

4.3 EMT in fibrosis

The role of EMT has been well established in cutaneous wound healing *in vivo*, *in vitro,* and *ex vivo*, as keratinocytes showed degradation of extra-cellular matrix (ECM), expression of fibroblast-specific protein 1 (FSP1) and/or vimentin (177). In an experimentally induced injury of murine lacrimal gland, inflammation induced by interleukin-1 (IL-1) injection triggered the generation and migration of cells with mesenchymal phenotype to the injury site, but these cells subsequently reverted to an epithelial phenotype once repair was complete (178). EMT processes are thought to be involved also in the fibrosis pathogenic mechanism of several different organs, among these we can see kidney and liver (179,180) but research is also focusing heart (181–183) and lung (184).

4.4 EMT in cancer metastasis

One hallmark of EMT is the shift from E-cadherin to N-cadherin expression in the same cell, the so-called “cadherin switch” (185–187). Integrins are the major class of receptors involved in homotypic and heterotypic adhesive events (188), and provide a link between the outside environment and cellular responses related to motility (189–191). Other structures of adhesion are hemidesmosomes, multiprotein complexes present in stratified epithelia, that are altered during EMT (192). Integrins are also able to improve anchorage-independent survival of circulating tumor cells (CTCs) (193). Integrin α6β4, present in hemidesmosomes, interacts with the keratin intermediate filaments instead of actin filaments, and it is the only integrin to do so. Therefore, the lack of polarity in tumor cells is displayed by actin protrusions, which will disassemble the hemidesmosomes and mediate cell migration and invasion (194). After the EMT-associated loss of hemidesmosomes, α6β4-integrin becomes phosphorylated and relocates to an F-actin–rich protrusion, where integrin interacts with actin filaments(192). It has been showed in patients with advanced metastatic Non-Small Cell Lung Cancer (NSCLC) that the majority of isolated or clusters of CTCs showed a dual epithelial–mesenchymal phenotype. This confirms that EMT is a relevant process for invasion and metastasis in these patients(195). In a murine model, the role of Twist in lung cancer showed that interfering with its expression through siRNA3 led to a drastic decrease in the number of metastases but did not prevent them(196). Interestingly, a study in human lobular breast cancer showed that CTCs were predominantly epithelial, while those from HER2+ and triple negative subtypes were mostly mesenchymal; this provided evidence of EMT in human breast cancer specimens (197), consistent with other studies in murine models(198). In another study it was shown that, the inhibition of EMT by overexpressing miR-200 does not affect lung metastasis development, even though EMT plays a role in lung cancer chemotherapy resistance(199). Interestingly, many invasive and metastatic carcinomas have not undergone a complete transition to a mesenchymal phenotype or even lack signs of EMT, and those invasive carcinomas do not invade adjacent connective tissue as individual mesenchymal-like cells, rather invade as multicellular aggregates or clusters (200,201).

4.5 EMT as a prognostic marker

The stage of a cancer is determined by its extent and its spread at the time of diagnosis, which is essential for guiding cancer surveillance and control, possible therapies and prognosis(202). One of the advantages of studying EMT in different stages of cancer and metastasis is to find out whether it is possible to use it as a prognostic marker, and evidences in some cancers suggest that the presence of EMT features can pre-emptively indicate prognosis. In order to create EMT-related prognostic markers, studies focused on EMT regulation (establishing correlations between its master regulators and tumor progression), on the expression of biomarkers (203). In human breast cancers, the loss of E-cadherin expression has been successfully related to poor prognosis (204,205). Interestingly, consistent results have been also published in canine mammary tumors (206,207). Moreover, expression of EMT master regulators Snail1, Slug, Twist can be directly associated to higher mortality and metastasis for hepatocellular and ovarian carcinoma in humans (208–211). In a study focusing on E-cadherin, Vimentin and Twist expressions in bladder cancer, only vimentin appears as an independent predictor for cancer progression and survival in muscle invasive bladder cancer (MIBC) (212,213). An interesting EMT gene signature has been developed for hepatocellular carcinoma (214); in a cohort of 128 hepatocellular carcinoma patients. It has been investigated the prognostic value of four candidate genes: CDH1, inhibitor of DNA binding 2 (ID2), matrix metalloproteinase 9 (MMP9), and transcription factor 3 (TCF3). This four gene-signature was correlated with significantly shorter overall survival, furthermore, tumor stage and this four gene-signature were independent prognostic factors (214). Even though successful results have been published, these markers are still not widely used for prognosis in clinical routine. One of the main problems is that in different locations of a same tumor the expression of EMT marker can differ, because of tumor heterogeneity. Moreover, these studies do not provide clear cut-offs for prognosis, that are present in other prognostic methods instead, like mitotic index, Ki67, Her2 and others (215–217). One possible future application of this wide oncogenomic data set will be the creation of personalized medicine programs, allowing clinicians to obtain a cancer specific and patient specific prognosis (218).

5.0 Mesenchymal to epithelial transition (MET) in sarcomas

The epithelial to mesenchymal transition (EMT) and its reverse process, termed the mesenchymal to epithelial transition (MET), play central roles in embryogenesis (135). EMT is an important process that allows epithelial cells to enhance migratory abilities dissolving intercellular connections, thus acquiring mesenchymal properties (135,219). Whereas EMT has been extensively studied and validated during the last two decades (219,220), the reason why a mesenchymal cells become more epithelial-like in phenotype, came into the research focus only in the last years (219,221,222). Interestingly, there are studies reporting that MET may exist in sarcomas (223–226). For example, the fusion protein SYT-SSX1 is shown to induce MET through snail family zinc finger (SNAI) regulation in synovial sarcomas (225).Moreover, in soft tissue leiomyosarcomas, MET process has been demonstrated using genomic and proteomics analysis, associating it with a better prognosis (226). Altogether, these findings suggest that MET might be a biological process that need to be deeper investigated in order to find useful clinical correlations such as prognostic markers or developing target therapies in tumors of mesenchymal origin (227).

5.1 Epithelial and mesenchymal markers expression in sarcomas

E-cadherin is the most recognized epithelial marker, which play a main role in both EMT and MET phenomena (224,226).

Interestingly, E-cadherin loss not only disrupts intercellular junctions but also leads to a gradual loss of normal cellular architecture(135,192). Cytokeratins, epithelial membrane antigen (EMA), and β-catenin are known to be other molecular markers for epithelial architecture.(135,192). It is noteworthy that the increased expression of typical epithelial markers including E-cadherin, EMA, β-catenin, CD44, cytokeratins, and CD34 is basilar to at least partly define the MET process in sarcomas (225,226,228–232).

On the other hand, the most commonly referred mesenchymal markers are vimentin and N-cadherin. In addition might result useful to consider also α-smooth muscle actin (α-SMA), desmin, α-actin, neuron-specific enolase, fibronectin and synaptophysin (226,228–232). Vimentin is a type-III intermediate filament normally expressed in cells of mesenchymal origin(233). N-cadherin is a transmembrane adhesion glycoprotein whose forced expression leads to downregulation of E-cadherin expression and enhances cancer cell motility and migration in epithelial tumors(226).

Interestingly, many soft tissue sarcomas have been described as exhibiting epithelial differentiation basing on epithelial markers detection [19–21]. Moreover, Ewing sarcomas/primitive neuroectodermal tumours (ES/PNETs), expressing claudin-1, zonula occludens-1 and occludin but not E-cadherin, suggested that this type of tumors are prone to undergo partial epithelial differentiation. Furthermore, both synovial sarcoma and leiomyosarcoma have been demonstrated to undergo MET phenomenon regulated by the SNAI transcription factors (226,234). Moreover, the cadherin-11 (CDH11) expression and autocrine motility factor/ phosphoglucose isomerase (AMF/PGI) were strongly suggestive of MET in osteosarcomas (230,235) . Finally, downregulation of SNAI1 in chondrosarcoma cells leads to an E-cadherin, desmocollin 3, maspin, and 14-3-3σ expression, which suggest a MET phenomenon (228).

5.2 MET signaling pathways

During MET process in sarcomas have been reported several initiating events, as survival signals via receptors such as platelet-derived growth factor receptor (PDGFR), fibroblast growth factor receptor (FGFR), c-MET, transforming growth factor beta-1 (TGF-β1), Insulin-related growth factor 1 receptor (IGF1R) and regulatory kinases such as phosphoinositide 3-kinase (PI3K), AKT, and mammalian target of rapamycin (mTOR) (223,224,234,236). During MET phenomenon, there are classes of molecules that result to be altered in function, distribution, and expression. These classes include growth factors as TGF-β and wnts; transcription factors such as SNAIs, LEF, TWIST, ZEB and nuclear β-catenin; cell to cell adhesion molecules as cadherins and catenins; molecules of the extracellular matrix adhesion such as integrins, focal contact proteins and ECM proteins; and extracellular proteases as matrix metalloproteinases and plasminogen activators (135,223,224,226,234,236). Twist basic helix–loop–helix transcription factor (Twist), SNAIs, and zinc finger E-box binding homeoboxs (ZEBs), which are associated with E-cadherin expression, are transcriptional factors considered key molecules in this process (234). For example, E-cadherin promoter activity can be inhibited either by SNAI1 or Twist bindings on the E2-boxes on the E-cadherin promoter (223,236). On the other hand, there are also different mechanism for E-cadherin expression upregulation in sarcomas such as E-cadherin mutations and epigenetic regulation (222,228). Moreover, the cytosine methylation in chondrosarcomas epigenetically regulates the E-cadherin, desmocollin 3, maspin, and 14-3-3 σ expression. In the end, should be considered also that a marked upregulation of E-cadherin and downregulation of N-cadherin in Saos-2 osteosarcoma cells can be obtained with a soluble low density lipoprotein receptor-related protein 5 (sLRP5) transfection (237).

5.3 MET as a prognostic marker

The promising data on MET in sarcomas might suggests a potential role in the clinical management of sarcomas. Therefore, the epithelial marker expression together with MET phenomena could serve as promising prognostic factors of sarcomas. Even if in a subset of leiomyosarcomas and in children's chordomas E-cadherin expression was associated with longer survival and tumor recurrence (226,238,239), it must be noted that the promising role of these markers have to be validated in strict prospective trials. Nowadays none of the aforementioned markers are used for patient managements yet (227).

5.4 MET as a therapeutic approach

Interestingly, vimentin resulted to be a novel promising anticancer therapeutic target. Withaferin- A is a bioactive compound that may target vimentin at a molecular level eliciting significant apoptosis and vimentin cleavage in those vimentin-expressing tumor cells within soft tissues sarcomas. It has also shown how Withaferin- A blocks the soft tissue sarcomas growth, recurrence and metastasis in xenografts model holding great promise (233). Moreover, important transcription factors regulating the MET process in sarcomas, as SNAI2, might be potential therapeutic targets as well (226). Beside vimentin and transcriptional factors, some other molecules involved in MET associated signaling pathways might also be analyzed to become potential targets. For example, AMF/PGI pathway might represent a promising target in many sarcomas such as lung fibrosarcoma and also osteosarcomas (230,237).

AIM OF THE WORK

Based on the previous findings about the decreased angiogenesis both *in vitro* and *in vivo* accompanied by a tumor regression *in vivo* (89) and the decreased cell motility (92) caused by a persistent infection with CDV, strain Onderstepoort (CDV-Ond) in DH82 cell line, two main hypothesis have been formulated and addressed in two independent *in vitro* studies.

-*IN VITRO* STUDY 1:

The hypothesis behind this study was that a persistent CDV-Ond infection of DH82 cells induces oxidative stress followed by a massive inhibition of HIF-1α degrading pathways. This in turn leads to cytoplasmic, non-functional accumulation of HIF-1α, which is associated with a reduced expression of HIF-1α downstream targets, such as VEGF-B. Based on the aforementioned hypothesis, the aim of the present *in vitro* study was to demonstrate that histiocytic sarcoma cells (DH82 cells) persistently infected with CDV-Ond show: (1) an increased oxidative stress status, (2) an increased HIF-1α protein expression, (3) an unusual intracellular distribution of HIF-1α, and (4) a reduced expression of HIF-1α downstream targets, with a special focus on VEGF-B.

-*IN VITRO* STUDY 2:

The hypothesis underlying the aim of the current study was that a persistent infection of histiocytic sarcoma cells (DH82 cells) with CDV-Ond, triggers the MET process by increasing the expression of epithelial markers resulting in a less invasive phenotype with decreased motility of the neoplastic cells.

EXPERIMENTAL SECTION

INTRODUCTION

Malignant neoplasms represent nowadays one of the most common causes of death in companion animals due to their often rapid and lethal progression (240). Canine histiocytic sarcoma (CHS) is a malignant tumor that may occur in a systemic or localized form with a poor prognosis and limited therapeutic options (241). Patients with CHS often have short survival times due to the high metastatic rate of this neoplasm which is furthermore characterized by a limited and ineffective response to conventional therapies including surgery, chemo- and radiotherapy(241). Therefore, novel and more effective approaches against this neoplasia are highly demanded. With the beginning of the twentieth century the idea took place to employ oncolytic viruses against neoplasms(27). This is based on the observation of the ability of several viruses to preferentially infect and destroy cancer cells using direct and indirect mechanisms (55). A CHS cell line (DH82 cells), which originates from a Golden Retriever with a disseminated histiocytic sarcoma (242–246) has been generated and is being used in various studies. These cells can be infected with CDV-Ond (90,91,93), and have been reported as a promising model for the investigation of viral oncolysis (55,89,91,92,247). Specifically, acute infection of DH82 cells with CDV-Ond *in vitro* resulted in a prominent cell death at 12 days post infection (90), followed by establishment of persistent infection in tumor cells surviving the acute lytic phase(91) . Due to the high percentage of CDV-infected cells in persistently infected DH82 cultures, this model may serve as a starting point for investigations canine distemper virus mediated oncolysis. Though an acute infection, might clinically be more applicable, the use of a persistently infected cells will allow to study in more detail basic mechanisms(89,92). In order to optimize the effectiveness of the CDV virotherapy and to consider it as a complementary option for other therapy, the oncolytic potential of CDV needs to be investigate in more detail. Therefore, the following *in vitro* studies will focus on the influence of the virus abut angiogenesis and cell invasiveness. One essential part of tumor growth is angiogenesis with HIF-1α playing a pivotal role in VEGF mediated neo-angiogenesis in malignancies as well as in cell metabolism (248,249). Moreover, it becomes important to focus on CDV- HIF-1α interactions that might lead to a HIF-1α downstream pathway dysregulation. Increasing knowledge in this field will further allow to understand the mechanism to inhibit cancer associated neo-angiogenesis leading to tumor regression associated with decreased invasion and metastasis. Another important feature of a CDV-induced modification of CHS cells represents the induction of MET. The MET phenomenon in sarcomas is often related with a better clinical outcome and prognosis (227) due to the decreased cell motility and invasive features (227). MET in sarcomas is characterized by an increased expression of epithelial markers with retention of the mesenchymal markers expression (227). A better understanding of the

underlying mechanisms of CDV induced MET in DH82 cells might allow to favor these processes and decrease the invasive and metastatic rate of such tumors. Taken together, the expected down-regulation of the tumor associated angiogenesis and the reduced invasiveness associated with the MET phenomenon, both driven by a CDV infection might give a more precise and accurate idea of the effectiveness of the CDV oncolytic model and its mode of action in fast growing and invasive tumors such as CHS. This will provide further insights into the potential application of this model as a promising candidate for therapeutical alternatives such as tumor virotherapy in dogs with CHS. The current status of the research in this area is based on various observations reported in the last ten years. Interestingly, a xenotransplantation of persistently CDV-infected DH82 cells led to an initial tumor formation followed by a complete spontaneous regression, which was accompanied, by a decreased intratumoral microvessel density and an increased tumor-associated inflammation (89). However, the underlying mechanisms are only partially elucidated so far. It has been shown *in vitro*, that CDV-Ond, possess the ability to modify the expression of reversion-inducing-cysteine-rich protein with Kazal motifs (RECK), matrix proteinases (MMP)-2 and -9 and tissue inhibitors of matrix proteinases (TIMP)-1 and -2 (91). Furthermore, cytoskeletal rearrangements including the alteration of the cortactin distribution, which led to a reduced migratory ability of cells and a reduction of the gene expression involved in angiogenesis are described (89,92) .

MATERIAL AND METHODS

IN VITRO STUDY 1

Cell culture and production of cell pellets

Non-infected DH82 cells were obtained from the European Collection of Authenticated Cell Cultures (ECACC No. 94062922). DH82 cells persistently infected with CDV-Ond (DH82Ond pi) were obtained as follow. DH82Ond pi were generated by infection of passage 104 of DH82 cells with the attenuated Onderstepoort strain of CDV (CDV-Ond) with a multiplicity of infection (MOI) of 1.0. To establish a stable population of persistently infected DH82 cells, which produces infectious virus particles in the culture supernatant, few surviving cells that did not undergo cytolysis were weekly passaged over a total number of 17 passages, which resulted in a stable persistently infected population

These cells were cultured according to standard procedures. Briefly, cells were cultured in minimal essential medium (MEM) with Earle's salts (PAA, Cölbe, Germany) supplemented with 10% fetal calf serum (PAA), 1% penicillin/streptomycin (PAA), and 1% non-essential amino acids (Sigma-Aldrich, Taufkirchen, Germany). Culture flasks were kept at 37°C in the presence of 5% CO_2 in a water saturated atmosphere.

Five formalin-fixed paraffin embedded (FFPE) cell pellets of non-infected DH82 cells and 5 of DH82Ond pi cells were produced.

Briefly, cells were scraped and centrifuged at 250xg for 10 min at 4 °C. Afterwards, the supernatant was removed, cells were washed in PBS and centrifuged again. Following a second wash and centrifugation step, the pellet was fixed in 1.5 ml of 10% non-buffered formalin overnight at 4°C, and processed for routine paraffin embedding.

Microarray data analysis using a manually generated list of gene symbols related to ROS production and scavenging, ER stress and HIF-1α pathway

In a hypothesis-driven approach, an online available microarray data set of quadruplicates of non-infected DH82 and DH82Ond pi cells (ArrayExpress; http://www.ebi.ac.uk/arrayexpress; accession number E-MTAB-3942 (89,250) was investigated for differentially expressed genes related to ROS production and scavenging, ER-stress and HIF-1α pathway, with a special focus on the angiogenic downstream targets of the latter. This choice was justified by the results of the

functional profiling of the same dataset obtained in a previous study, highlighting a down-regulation of the expression of some of the genes correlated with angiogenesis (89). Therefore, in the current work, a list of human and murine genes and proteins was manually generated according to the literature (103,124,248,251–256) and translated into canine orthologous gene symbols using the web-based HGNC database (HGNC Database, HUGO Gene Nomenclature Committee (HGNC), European Molecular Biology Laboratory, European Bioinformatics Institute (EMBL-EBI), Wellcome Genome Campus, Hinxton, Cambridge CB10 1SD, United Kingdom, www.genenames.org (257). After filtration, the raw expression data of the selected genes were compared between non-infected DH82 and DH82Ond pi cells, employing multiple pairwise nonparametric Mann–Whitney U-tests. Statistical analysis was performed with SAS Enterprise Guide (SAS version 9.3; SAS Institute Inc, Cary, NC, USA). Differential expression was defined as the combination of a fold change (FC) filter (FC $\geq$1.5 or $\leq$ -1.5) and of a statistical significance filter (Mann–Whitney U-test; $p \leq 0.05$) (258). To facilitate the interpretation of results, each gene symbol was assigned to at least one of the following functional groups on the basis of the function(s) carried out by its corresponding protein(s): ROS production; ROS scavenging; ER stress; HIF-1α activation, transcriptional activity and regulation; HIF-1α angiogenic downstream pathway.

Immunofluorescence and statistical analysis

Immunofluorescence was performed on FFPE pellets of non-infected and persistently CDV infected DH82 cells. Sections were deparaffinized, rehydrated through graded alcohol and pre-treated for antigen retrieval. Following blocking of unspecific bindings, sections were incubated with primary antibodies for 90 min at room temperature. After 60 min of incubation with the secondary antibody, nuclei were stained with Bisbenzimide (Sigma-Aldrich Chemie GmbH, Taufkirchen, Germany), and the slides were mounted with Dako Flourescence Mounting Medium (Dako North America, Inc., Carpinteria, CA, USA). Each reaction was carried out with corresponding positive controls (Table 1). For negative controls, the first antibody was replaced with rabbit serum, Balb/c ascitic fluid, or goat serum, respectively at corresponding protein concentrations. To verify the persistent infection status of DH82Ond pi cells (which was set as corresponding to a rate of >95% infected cells), an immunolabeling with an anti-CDV nucleoprotein (CDV-NP) antibody (clone D110; kindly provided by Prof. A. Zurbriggen, University of Bern, Switzerland) was performed. Furthermore, pellets were stained with antibodies directed against 8-hydroxyguanosine/8-hydroxydeoxyguanosine (8OHG/8OHdG, in the following paragraphs simply referred to as 8OHdG), a marker of ROS-damaged RNA or

DNA; superoxide dismutase 2 (SOD2) and catalase (CAT), two ROS scavengers; HIF-1α, a transcription factor; wheat germ agglutinin (WGA), a cell membrane marker; CD63, directed against tetraspanin-30 expressed on exosome membranes; and GM-130, a marker for Golgi apparatus. All details regarding the antibodies used are listed in Table 1. For CDV-NP, 8OHdG, SOD2, CAT, HIF-1α, and VEGF-B, the percentage of immunopositive cells for each group (non-infected DH82 cells and DH82Ond pi cells) was assessed manually by counting 5 evenly distributed fields per pellet at a 400x magnification using an inverted fluorescence microscope (Olympus IX-70, Olympus Optical Co. GmbH, Hamburg, Germany) equipped with a Olympus DP72 camera and Olympus cellSens standard software version 2.3. Additionally, for HIF-1α the intracellular protein distribution was assessed and calculated as percentage of cells immunopositive within the nucleus, cytoplasm and membrane. For each marker, after calculation of the median percentage of immunopositive cells per pellet, the normality of distribution of the data referring to non-infected and DH82Ond pi cells was evaluated with the Shapiro-Wilk test and followed by the Mann-Whitney U test for pairwise comparison. The difference of the intracellular distribution of HIF-1α immunopositivity within each group of cells was analyzed with the Kruskall-Wallis test with post-hoc Dunn's test. Statistical significance for each analysis was set at p-value≤0.05. All statistical analyses were performed with GraphPad Prism version 8.0.1 for Windows (GraphPad Software, La Jolla, CA, USA, www.graphpad.com).

Table 1. Details of the antibodies used for the immunostaining performed, including primary antibody, host species, clonality, epitope retrieval method, blocking serum, dilution of primary antibody, secondary antibody and positive control.

Primary Antibody	**Host Species, Clonality**	**Epitope Retrieval**	**Serum Blocking**	**Dilution**	**Secondary Antibody (1:200)**	**Positive Control**
CDV-NP (University of Bern)	Mouse, monoclonal, clone D110	Citrate buffer, microwave (800 W, 20′)	PBST + 3% BSA + 5% goat serum	1:100	GaM-Cy3 or GaM-Cy2	n/a
8OHdG (Abcam, Cambridge, USA)	Goat, polyclonal	Proteinase K	PBST + 3% BSA + 5% horse serum	1:200	DaG-Cy3	Canine pyo-granu-lomatous endo-metritis
SOD2 (Abcam, Cambridge, USA)	Rabbit, polyclonal	Citrate buffer, microwave (800 W, 20′)	PBST + 3% BSA + 5% goat serum	1:200	GaR-Cy2	Canine brain and spinal cord

CAT (Abcam, Cambridge, USA)	Goat, polyclonal	Citrate buffer, microwave (800 W, 20′)	PBST + 3% BSA + 5% horse serum	1:50	DaG-Cy3	Canine spinal cord with fibro-carti-lagineous embolus
HIF-1α (Novus Biologicals, Colorado, USA)	Rabbit, polyclonal	Citrate buffer, microwave (800 W, 20′)	PBST + 3% BSA + 5% goat serum	1:500	GaR-Cy3 or DaR-Cy2	Canine mammary adeno-carcinoma with central necrosis
Wheat germ agglutinin (WGA) AF633 conjugated (Invitrogen, California, USA)	none	Citrate buffer, microwave (800 W, 20′)	n/a	1:20	n/a	n/a
CD63 (Sicgen, Coimbra, Portugal)	Goat, polyclonal	Citrate buffer, microwave (800 W, 20′)	PBST + 3% BSA + 5% horse serum	1:200	DaG-Cy3	MDCK cell pellet
GM-130 (BD Transduction Laboratories, North Carolina, USA)	Mouse, monoclonal, clone 35/GM130 (RUO)	Citrate buffer, microwave (800 W, 20′)	PBST + 3% BSA + 5% goat serum	1:200	GaM-Cy2	n/a
VEGF-B (My Biosource, California, USA)	Rabbit, polyclonal	Citrate buffer, microwave (800 W, 20′)	PBST + 3% BSA + 5% goat serum	1:40	GaR-Cy3	Canine fetal brain, liver and kidney

BSA, bovine serum albumin; CDV-NP, canine distemper virus nucleoprotein; DaG-Cy3, donkey anti goat cyanine 3-conjugated; DaR-Cy2, donkey anti rabbit cyanine 2-conjugated; GaM-Cy2, goat anti mouse cyanine 2-conjugated; GaM-Cy3, goat anti mouse cyanine 3-conjugated; GaR-Cy2, goat anti rabbit cyanine 2-conjugated; GaR-Cy3, goat anti rabbit cyanine 3-conjugated; GM130, Golgi membrane protein of 130 kDa; HIF-1α, hypoxia-inducible factor 1 α; MDCK, Madin-Darby canine kidney cells; n/a, non applied or non applicable; PBST, phosphate buffered saline Tween-20; SOD2, superoxide dismutase 2; VEGF-B, vascular endothelial growth factor-B; WGA, wheat germ agglutinin; 8OHdG, 8-hydroxyguanosine/8-hydroxydeoxyguanosine

Determination of oxidative burst by flow cytometry

Non-infected and persistently CDV-Ond infected DH82 cells were treated with 2′,7′-dichlorofluorosceindiacetate (DCF, final concentration of 10 µM, Sigma Aldrich, D6883) at 37 °C and 5% CO_2 for 20 min. Flow cytometer (Attune® NxT Acoustic Focusing; laser 488nm (50 mW), filter BL-1 = 530/30) analysis was performed measuring mean green fluorescence intensity

(X-Mean of BL-1) as relative ROS production. Respective background controls without DCF were included in all assays. Threshold was adjusted to unstained cells to remove background. Green fluorescence intensity (FITC) of all cells (percentage of positive cells) was recorded by flow cytometry as relative measure of ROS production. The following settings were used: acquisition volume of 100 µl/min, stop at 10,000 events on all counts; instrument settings: FSC 80, SSC 320 BL1 310 (FITC). For quantification of the percentage of positive cells, doublets were excluded by FCS-A versus FSC-H gating (Supplementary Fig. 1) and only FL-1-positive cells (Gate 2) of all singlet cells (Gate 1) were quantified. Statistical analyses of measurements were performed with GraphPad Prism version 8.0.1 for Windows (GraphPad Software, La Jolla California USA, www.graphpad.com) using unpaired t-tests.

Immunoelectron microscopy

To evaluate in more detail the intracellular localization of HIF-1α within DH82Ond pi cells, immunoelectron microscopy was performed using a 10% neutral buffered formalin fixed cell pellets. Thirty µm thick sections were cutted and diluted in cacodylate buffer (Serva Electrophoresis GmbH, Heidelberg, Germany) for one night followed by embedding in LR-White (LR-White Resin, MEDIUM GRADE Acryl Resin, London Resin Company Ltd., Reading, United Kingdom). Ultrathin sections of LR-White embedded samples were immunolabeled with an anti- HIF-1α antibody (1:500 dilution; Novus biologicals) followed by a goat anti-rabbit IgG 10 nm immunogold conjugated secondary antibody (BBI Solutions, Crumlin, United Kingdom). The sections were contrasted with uranyl acetate and lead citrate. Samples were further evaluated using a transmission electron microscope (EM 10A, Carl Zeiss Microscopy GmbH, Jena, Germany) equipped with a 2K-CCD-Camera (TRS) and using Image SP professional software.

Laser scanning confocal microscopy

The intracellular HIF-1α distribution was analyzed by double-labeling immunofluorescence (DL-IF). Therefore, HIF-1α was combined with WGA as a marker for the cell membrane, CD63 as an exosomal marker, GM-130 as a marker for the Golgi apparatus, and CDV-NP. The evaluation was performed using a Leica TCS SP5 AOBS confocal inverted-base fluorescence microscope (Leica Microsystems, Bensheim, Germany) with a conventional galvanometer scanner of the Leica SP5 II tandem scanning system and the Leica Application Suite Advanced Fluorescent Lite 2.0.2 build 2038 (Leica, Biberach, Germany). The microscope was equipped with 3 lasers [405 DIODE (415/2471), ARGON (500/2571) and HeNe 633 (639/2715)], and with HCX PL APO ×40 0.75-1.25 and HCX PL APO ×63 0.75-1.25 oil immersion objectives used for the evaluation

of double-labelling. Settings for each marker were adjusted using respective appropriate control antibodies. Images were analyzed using Leica LAS AF software (version 2.7.3).

Immunoblotting

Cell lysates from non-infected and persistently CDV infected DH82 cells were prepared by freezing and thawing in 1 mL NP-40 buffer (50mM Tris-HCl, 150 mM NaCl, 1% NP-40, 5 mM EDTA) with 50 µL protease inhibitor cocktail (1.48 µM Antipain dihydrochloride, 0.768 µM Aprotinin, 10.51 µM Leupeptin, 1.46 µM Pepstatin A in DMSO, 1mM PMSF, 50 µg/mL Trypsin inhibitor T9128, pH 8.0) (all reagents from Sigma-Aldrich, St. Louis, USA). The correct amount of each cell lysate required for the analysis was calculated based on the protein concentration determined applying the Bradford method. Samples were analyzed by SDS-PAGE on 8% gels and subsequently transferred to a Polyvinylidene fluoride (PVDF) membrane. Immunoblotting was performed using a polyclonal anti- HIF-1α (0.75 µg/mL, Cayman, Ann Arbor, USA) and a monoclonal anti- β -actin (0.2 µL/mL, Santa Cruz, Dallas, USA) antibody, respectively. A polyclonal IgG antibody from rabbit serum served as a negative control (2 µg/mL, Sigma-Aldrich, St. Louis, USA). Secondary anti-rabbit or anti-mouse antibodies conjugated to horseradish peroxidase were used (0.2 µg/mL, ThermoScientific, Schwerte, Germany). Protein bands were visualized using SuperSignal. West Femto maximum sensitivity western blot chemiluminescence substrate (ThermoScientific, Schwerte, Germany) and a ChemiDoc MP Imaging System (Bio-Rad, Hercules, CA, USA). Quantification was performed densitometrically. Obtained results for HIF-1α were displayed as a ratio with the corresponding amount of β-actin. Statistical analyses of obtained ratios were performed with GraphPad Prism version 8.0.1 forWindows (GraphPad Software, La Jolla, CA, USA, www.graphpad.com) using unpaired t-tests.

IN VITRO STUDY 2

Cell culture

Non-infected DH82 cells, a permanent canine histiocytic sarcoma cell line, were obtained from the European Collection of Authenticated Cell Cultures (ECACC No. 94062922). Persistently CDV (strain Onderstepoort)-infected DH82 cells (DH82Ond pi) were produced as previously described for the *in vitro* study 1. Cells were cultured and kept in the same conditions of the *in vitro* study 1. Briefly, cells were cultured in minimal essential medium (MEM) with Earle's salts (PAA, Cölbe, Germany) supplemented with 10% foetal calf serum (PAA), 1% penicillin/ streptomycin (PAA) and 1% non-essential amino acids (Sigma- Aldrich, Taufkirchen, Germany). Culture flasks were kept at standard conditions (37°C with 5% CO2 in a water saturated atmosphere).

Morphological analysis using phase contrast microscopy

The morphology of non-infected DH82 and DH82Ond pi cells was analysed using a phase contrast microscope (Olympus IX-70, Olympus Optical Co. GmbH) equipped with an Olympus DP72 camera and Olympus cell sense standard software version 2.3. Cells were observed at 6 hours, 12 hours, 24 hours, 36 hours, 48 hours, 60 hours, 3 days, 4 days, 5 days, 6 days and 7 days after seeding. Afterwards, cells were counted according to their morphology and grouped in 4 different categories: round-shaped, triangle-shaped, cigar-shaped and slender. For both DH82 and DH82Ond pi cells, 10 T75 flasks each were checked for morphology of the cells at 6h, 12h, 24h, 36h, 48h, 60h, 3 days, 4 days, 5 days, 6 days and 7 days after seeding. At every time point the flasks were observed using a phase contrast microscope (Olympus IX-70, Olympus Optical Co. GmbH, Hamburg, Germany) equipped with an Olympus DP72 camera and Olympus cell sense standard software version 2.3, at a 20x magnification. For every flask having a homogeneously distributed cell growth, 5 pictures were taken at the 4 corners of the flask and one in the middle. The pictures were further analyzed and for every field the presence of the 4 most common morphological cell types was recorded. Cells were classified as 1) round cells of different sizes, 2) triangle shaped cells, presenting a cytoplasm modified in a shape resembling a ”kite”, with a prominently oriented cell protrusion, 3) cigar-shaped cells, presenting an increased longitudinal length, with frequently blunted ends, and resembling a thin cylinder, and 4) slender cells, presenting with a very elongated cytoplasm with frequent cytoplasmic projections and a small cytoplasmic width (Supplementary Fig. 2).

Cumulative population doubling assay

The population doubling assay was performed as by evaluating non-infected DH82 cells and DH82Ond pi cells over 14 weeks. Briefly, cells were seeded into 75-cm^2 flasks (Nunc GmbH & Co. KG, Thermo Scientific, Langenselbold, Germany) and counted at every weekly passage over 14 weeks. Population doubling was determined using the following population doubling (PD) formula: PD = log10 (cells harvested—initial cell number)/log2 (259).Then, the cumulative population doubling was determined by adding the PD of every weekly passage to the previous one. Statistical analysis as well as graphical visualization was performed using GraphPad Prism version 8.0.1 for Windows (GraphPad Software, La Jolla California USA, www.graph pad.com). The values were analyzed with non-parametric Wilcoxon–Mann–Whitney two-sample test, setting the significance level at $P \leq .05$.

Microarray data analysis using a manually generated list of gene symbols related to MET and invasiveness

Data of a previously published microarray dataset of non-infected DH82 and DH82Ond pi cells (ArrayExpress; http://www.ebi.ac.uk/ array express; accession number E-MTAB-3942) (89,92,250) were used to evaluate the potential influence of a persistent CDV infection on genes associated with EMT/MET and cellular motility. In a hypothesis-driven approach, the present study focused on a manually generated list of selected genes associated with EMT/MET, invasion and angiogenesis. Selected gene symbols were based on previously published lists(89,92), which were further modified and extended (Supplementary Table 1). According to the biological function of the corresponding protein(s), each selected gene symbol was assigned to 'EMT/MET' and/or 'invasion and angiogenesis' functional group. Genes were considered as differentially expressed between non-infected DH82 and DH82Ond pi cells combining a fold change (FC) filter (FC ≥ 1.5 or ≤−1.5) (258) with a statistical significance filter (Mann–Whitney *U* test;$P \leq .05$).

Immunofluorescence

Non-infected DH82 and DH82Ond pi cells were seeded at a density of 0.03 * 10^6 cells/0.33 cm^2 into 96 Microwell Nuncplates (Nunc GmbH & Co. KG, Thermo Scientific). All the immunostainings were performed in triplicates with negative controls in duplicates. Three days after seeding, cells were fixed with 4% paraformaldehyde and immunofluorescence was performed according to a 2 days protocol. To verify the persistent CDV infection state of DH82Ond pi cells, an immunolabelling with an anti-CDV nucleoprotein (CDV-NP) antibody

(clone D110; kindly provided by Prof. Dr A. Zurbriggen, University of Bern, Switzerland) was performed. Furthermore, cells were immunolabelled for E-cadherin, β-catenin and cytokeratin 8 as epithelial markers, and for vimentin and N-cadherin as mesenchymal markers. All details regarding the aforementioned antibodies are listed in Table 2. For negative controls, the first antibody was replaced with rabbit serum, Balb/c ascitic fluid or goat serum, respectively, at corresponding protein concentrations. For all the aforementioned markers, the percentage of immunopositive cells was determined for each group (non-infected DH82 cells and DH82Ond pi cells) by counting 5 evenly distributed fields per well, taking pictures at a 400× magnification using a fluorescence microscope (Olympus IX-70, Olympus Optical Co. GmbH) equipped with an Olympus DP72 camera and Olympus cell sense standard software version 2.3. The analysed pictures were taken from areas of different confluence (low, medium, high) for each marker and for both persistently CDV-infected and non-infected DH82 cells. Besides the determination of the overall percentage of positive cells for each marker, the number of positive cells based on the cell shape (round, spindle or multinucleated giant cells) as well as the number of positive cells based on the intracellular localization (membranous, membranous to cytoplasmic, diffusely cytoplasmic, focally cytoplasmic) was additionally evaluated. Membranous staining pattern was considered for cells with a membranous staining only, membranous to cytoplasmic was considered for cells with both membranous and cytoplasmic staining, diffuse cytoplasmic was considered for a diffuse cytoplasmic staining pattern, and focal cytoplasmic was considered for immunolabelings other than diffuse cytoplasmic that involved only one focal area of the cytoplasm. Cell shapes were considered as: round for any roundish cell of any dimension, multinucleated giant cell for cells with more than 2 nuclei and a total size larger than 3 cells, and spindle for those cells other than round and multinucleated giant cells (e.g. cigar-shaped, slender, and triangle-shaped cells as described for the phase contrast microscopy morphological analysis). Statistical analysis as well as graphical visualization was carried out using GraphPad Prism version 8.0.1 for Windows (GraphPad Software, La Jolla California USA, www.graph pad.com. The values were analysed with Student's *t* test, setting the significance level at $P \leq .05$.

Table 2: Details of the antibodies and the lectin used for the immunostaining including primary antibody, host species, clonality, blocking serum, dilution of primary antibody and secondary antibody.

Primary antibody	Host species, clonality	Serum blocking	Dilution	Secondary antibody (1:200)
Beta catenin (Sicgen)	Goat, polyclonal	Horse serum	1:100	DaG-Cy3
Cytokeratin 8 (Invitrogen)	Rabbit, polyclonal	Goat serum	1:200	GaR-Cy3 / GaR-AF 488*
E-cadherin (BD transduction lab)	Mouse, monoclonal clone 36/E-Cadherin (RUO)	Goat serum	1:200	GaM-Cy2 / GaM AF488**
N-cadherin (Proteintech)	Rabbit, polyclonal	Goat serum	1:100	GaR-Cy3
Vimentin (Dako)	Mouse, monoclonal clone V9	Goat serum	1:100	GaM-Cy2 / GaM AF488**
CDV-NP (University of Bern)	Mouse, monoclonal clone D110	Goat serum	1:100	GaM-Cy2
WGA - AF633 conjugated (Invitrogen, California, USA)	None	n/a	1:20	n/a

Legend: CDV-NP, canine distemper virus nucleoprotein; DaG-Cy3, donkey anti goat cyanine 3-conjugated; GaM AF488, goat anti mouse Alexa Fluor 488-conjugated; GaM-Cy2, goat anti mouse cyanine 2-conjugated; GaR-AF488, goat anti rabbit Alexa Fluor 488-conjugated, GaR-Cy3, goat anti rabbit cyanine 3-conjugated; n/a, non applied or non applicable, WGA – AF633, wheat germ agglutinin – Alexa Fluor 633 conjugated.

*GaR-Cy3 was used for single-labeling stain, and GaR-Cy2 for double-labeling stain.

**GaM-Cy2 was used for single-labeling stain, and GaM-AF488 for double-labeling stain.

Immunofluorescence double labelling, laser scanning confocal microscopy, and 3D reconstruction

E-cadherin, cytokeratin 8 and vimentin were further analysed with laser scanning confocal microscopy to allow a better characterization of the intracellular localization of these markers. Firstly, confocal microscopy was used to evaluate cells stained with single-labelling immunofluorescence for E-cadherin and cytokeratin 8. Then, to allow a better characterization of the spatial distribution of E-cadherin, cytokeratin 8 and vimentin within the cell volume, double-labelling immunofluorescence was performed combining each marker with wheat germ agglutinin (WGA), which was used to stain cell membrane and Golgi apparatus. Double staining

immunolabellings with WGA were performed as previously described in the *in vitro* study 1 with variations. Non-infected DH82 and DH82Ond pi cells were seeded at a density of 0.03*106 cells/0.33cm2 into 96-Well Plates, No. 1.5 Coverslip, 5 mm Glass Diameter, Uncoated (Mat Tek life sciences). All the immunostainings were performed in triplicates with negative controls in duplicates. 3 days after seeding, cells were fixed with 4% paraformaldehyde for 20 minutes at room temperature (RT), followed by serum blocking using PBS–triton (PBST) + 5% normal goat serum + 3% bovine serum albumin (BSA) for 15 minutes at RT. Primary antibodies were diluted in PBST + 3% BSA as follows: cytokeratin 8, 1:200; vimentin, 1:100; and E-cadherin, 1:200; and were incubated at RT for 90 minutes. Afterwards secondary fluorescence conjugated antibodies were diluted 1:200 in PBST + 3% BSA and subsequently incubated for 120 minutes at RT. Goat-anti-mouse (GAM) labeled with Alexa Fluor (AF) 488 (Dianova) was used for vimentin and E-cadherin while goat-anti-rabbit (GAR)-AF 488-conjugated (Invitrogen) was applied for cytokeratin 8. After washing the wells for 5 minutes with PBST, the Alexa Fluor 633-conjugated lectin WGA (Wheat Germ Agglutinin - AF633 conjugated, Invitrogen) was incubated for 120 minutes, followed by washing with bi-distilled water and bisbenzimide (Sigma-Aldrich Chemie GmbH) nuclear counterstaining. For negative controls, the first antibody was replaced with rabbit serum (cytokeratin 8) or Balb/c ascitic fluid (vimentin, E-cadherin) at corresponding protein concentrations. Details about the antibodies are listed in Table 2. Cells were analysed using a Leica TCS SP5 AOBS confocal inverted-base fluorescence microscope (Leica Microsystems, Bensheim, Germany) with a conventional galvanometer scanner of the Leica SP5 II tandem scanning system and the Leica Application Suite Advanced Fluorescent Lite 2.0.2 build 2038 (Leica, Biberach, Germany). The microscope was equipped with 3 lasers [405 DIODE (415/2471), ARGON (500/2571) and HeNe 633 (639/2715)], and with HCX PL APO ×40 0.75-1.25 and HCX PL APO ×63 0.75-1.25 oil immersion objectives used for the evaluation of the single and double-labelling immunofluorescence, respectively. Settings for each marker and each stain (ie single- or double-labelling) were adjusted using the corresponding appropriate controls. For the single-labelling stains, images were analysed using Leica LAS 244 AF software (version 2.7.3). For the 3D reconstructions of the double-labelling immunofluorescences, z-stacks were collected and analysed with LAS X 3D version 3.1.0 software from Leica. The specific number of z-stack frames (0.13 µm steps) ranged from 65 to 151 (the specific number of frames for each z-stack is reported in the caption of the corresponding figure). For each z-stack set, the background was set to black by standard software settings. Subsequently, top view and section view of the 3D reconstructions were created for each staining. Section view allowed to analyse protein localization within the cells.

Immunoblotting

Immunoblotting of non-infected and persistently CDV-infected DH82 cells was comparatively carried out in three independent samples for each cell type. Cell lysates from non-infected and persistently CDV infected DH82 cells were prepared by freezing and thawing in 1 ml NP-40 buffer (50mM Tris-HCl, 150 mM NaCl, 1% NP-40, 5 mM EDTA, 50 µl protease inhibitor cocktail (1.48 µM Antipain dihydrochloride, 0.768 µM Aprotinin 1.46 µM, 10.51 µM Leupeptin, 1.46 µM Pepstatin A in DMSO, 1 mM PMSF, 50 µg/ml Trypsin inhibitor T9128, pH 8.0), all reagents from Sigma-Aldrich, St. Louis, USA). Following cell lysis, the correct amount of each sample required for the analysis was calculated based on the protein concentration as determined applying the Bradford method. Samples were analyzed by SDS-PAGE on 8% gels and subsequently transferred to a Polyvinylidene fluoride (PVDF) membrane. Immunoblotting was performed using as primary antibodies polyclonal anti-β-catenin (1:500, Sicgen) and anti-CK8 (1:2000, Invitrogen), and monoclonal anti-β-actin (1:200, Santa Cruz, Dallas, USA) and anti-E-cadherin (1:200, BD transduction laboratory) antibodies. Polyclonal IgG antibody from rabbit serum served as a negative control (2 µg/ml, Sigma-Aldrich, St. Louis, USA). Secondary anti-rabbit, anti-goat or anti-mouse antibodies conjugated to horseradish peroxidase were used (0.2 µg/ml, ThermoScientific, Schwerte, Germany). Protein bands were visualized using SuperSignal™ West Femto maximum sensitivity western blot chemiluminescence substrate (ThermoScientific, Schwerte, Germany) and a ChemiDoc MP Imaging System (Bio-Rad, Hercules, USA). To ensure that the observed differences actually reflected differences in the protein expression, β-actin was set as a house-keeping protein to allow the investigation of the relative expression of β-catenin, E-cadherin and CK8 following densitometric analysis and using β-actin for normalization. Therefore, the differential expression of the β-actin gene and protein between non-infected and persistently CDV-infected DH82 cells was evaluated with microarray data and densitometry of Western blot bands, respectively. Specifically, for the microarray data analysis a combination of a fold change (FC) filter (FC $\geq$ 1.5 or $\leq$−1.5) with a statistical significance filter (Mann–Whitney *U* test; $P \leq .05$) was applied. Then, for each cell lysate the protein amount of β-catenin, E-cadherin and CK8 was quantified densitometrically and obtained results were shown as a ratio with the corresponding amount of β-actin. Statistical analysis was carried out using GraphPad Prism version 8.0.1 for Windows (GraphPad Software, La Jolla California USA, www.graph pad.com). The overall values of β-actin as well as the values of the ratios of β-catenin, E-cadherin and CK8 to β-actin were analysed with unpaired *t* test, setting the significance level at $P \leq .05$. Further information is available as supplementary material.

Scratch assay and invasion assay

For the scratch assay, non-infected DH82 and DH82Ond pi cells were seeded in 3 wells each at a density of 0.3 * 10^6 cells/1.9 cm^2 into 24 well/plates (Nunc GmbH & Co. KG, Thermo Scientific) with 1 ml of minimal essential medium (MEM) with Earle's salts (PAA, Cölbe, Germany) supplemented with 10% fetal calf serum (PAA), 1% penicillin/streptomycin (PAA) and 1% non-essential amino acids (Sigma-Aldrich, Taufkirchen, Germany). Three days after seeding and cultivation under standard conditions (37°C with 5% CO_2 in a water saturated atmosphere) cells reached 99% of confluence. The monolayer of cells was then scratched in a straight line with a p1000 pipette tip. Medium and cellular debris were then slowly removed, and fresh culture medium was gently added. Pictures were taken at the same position for every time point using a phase contrast microscope (OlympusIX-70, Olympus Optical Co. GmbH) equipped with an Olympus DP72 camera and Olympus cell sense standard software version. The aforementioned software was used to define and calculate the cell-free area of the scratch. Following the scratch (time point 0), the measurement of the wound area was performed after 6 and 24 hours. The percentage of scratch closure was calculated according to the following formula: (Area T0 – Area Tx)/Area T0. For the invasion assay, non-infected DH82 and DH82Ond pi cells were seeded in 6 wells each at a density of 0.04 * 10^6 cells/0.33 cm^2 into 96 well/plates (Nunc GmbH & Co. KG, Thermo Scientific) with 200 µl of MEM with Earle's salts (PAA, Cölbe, Germany) supplemented with 10% foetal calf serum (PAA), 1% penicillin/streptomycin (PAA) and 1% non-essential amino acids (Sigma-Aldrich). After seeding, cells were incubated under standard conditions (37°C with 5% CO_2 in a water saturated atmosphere). When the cells reached the desired confluence (80%-100%) 3 days after seeding, the cell monolayer was scratched creating a linear wound with a p100 pipette tip. Medium and cellular debris were gently removed and replaced by Matrigel matrix (Corning, New York, USA) diluted at a concentration of 3 mg/ml in culture medium. After gelification of the Matrigel matrix following incubation at 37°C, 5% CO_2 for 2 hours, the Matrigel layer was covered with 50 µl of MEM with Earle's salts (PAA, Cölbe, Germany) supplemented with 1% penicillin/streptomycin (PAA), and 1% non-essential amino acids (Sigma-Aldrich), and the plates were re-incubated under standard conditions. Cell invasion through Matrigel was evaluated 6, 24 and 144 hours after gelification of the matrix. For each well, a picture was taken at the same position for every time point using a phase contrast microscope (Olympus IX- 70, Olympus Optical Co. GmbH) equipped with an Olympus DP72 camera and Olympus cell sense standard software version. Pictures were analyzed with Fiji (ImageJ 1,52p) to define and calculate the cell-free area of each picture. Specifically, after 8bit conversion and automatic adjustment of brightness/contrast of the picture followed by an

automatic subtraction of background staining, the threshold was set to 0 and 194 and cell-covered area was determined with the analyze particle function using an overlay mask. The percentage of cell-free area was then calculated according to the following formula: 100 – cell-covered area, with the latter corresponding to the percentage value automatically determined by Fiji. The percentage of variation of the cell-free area was then calculated according to the following formula: (|Area T0 – Area Tx|)/Area T0 * 100, with Tx alternatively referring to the 6 hours or the 24 hours time point. For both the scratch and the invasion assay, statistical analysis as well as graphical visualization was carried out using GraphPad Prism version 8.0.1 for Windows (GraphPad Software, La Jolla California USA, www.graph pad.com). The data obtained by the scratch assay and the invasion assay were compared between persistently infected and non-infected cells using a two-way ANOVA, setting the significance level at $P \leq .05$.
Pictures were analyzed with Fiji [https://imagej.net/Fiji] to define and calculate the cell-free area of each picture. Specifically, the following macro applied to each picture:

```
run("8-bit");
//run("Brightness/Contrast...");
run("Enhance Contrast", "saturated=0.35");
run("Apply LUT");
run("Subtract Background...", "rolling=50 light");
setAutoThreshold("Default");
//run("Threshold...");
setThreshold(0, 194);
//setThreshold(0, 194);
setOption("BlackBackground", false);
run("Convert to Mask");
run("Analyze Particles...", "pixel show=[Overlay Masks] display summarize in_situ");
run("Labels...", "color=white font=9");
```

Afterwards, the percentage of cell-free area was calculated according to the following formula: 100 – cell-covered area, with the latter expressed as a percentage automatically calculated by Fiji. The percentage variation of the cell-free area was then calculated according to the following formula: (|Area T0 – Area Tx|)/Area T0*100, with Tx referring to of the time points evaluated

RESULTS

IN VITRO STUDY 1

Persistent CDV infection of DH82cells leads to an increased level of intracellular ROS associated with increased catalase and superoxide dismutase 2 protein expression

The infection status of DH82Ond pi cells was assessed via immunofluorescence staining for CDV-NP (Supplementary Figure 3). While immunoreactivity for CDV-NP of non-infected DH82 cell pellets was negative in all cells, DH82Ond pi cell pellets showed a median percentage of 99.65% (range: 99.05–100.00%) infected cells. On a molecular level, a manually generated list of 235 canine gene symbols associated with ROS production and scavenging, ER stress and the HIF-1α pathway was analyzed using a microarray dataset of DH82 and DH82Ond pi cells. This investigation resulted in a list of 230 genes present within the available data set (Supplementary Table 2). Using the combination of a statistical significance filter (Mann–Whitney U-test; $p \leq 0.05$) and a fold change (FC) filter ($FC \geq 1.5$ or ≤ -1.5), 57 genes were differentially expressed. Specifically, 31 canine genes showed a down-regulation, whereas 26 genes were up-regulated (Table 3). When specifically analyzed according to the functional grouping, 12 genes related to ROS production were up-regulated, while nine were down-regulated (Table 3). Among the group of genes related to ROS scavenging, five genes were up- and five were down-regulated (Table 3). Specifically, neutrophil cytosolic factor 4 (NCF4) and thioredoxin interacting protein (TXNIP), belonging to ROS production and ROS scavenging functional groups, respectively, were the two most markedly up-regulated genes among the entire set examined. Taken together, these findings should be cautiously interpreted as an increased transcription of genes which corresponding proteins are involved in increasing intracellular oxidative stress (103,254,260,261). Among the group of genes related to ER-stress (partially overlapping with both ROS production and ROS scavenging functional groups), 12 genes were up-regulated while 14 were down-regulated. Specifically, among the genes included in the ER stress functional group, the xanthine dehydrogenase (XDH) was up-regulated, while among down-regulated genes were included 3 (PDIA3, PDIA4 and PDIA6) out of 4 genes related to protein disulphide isomerases, one (ERO1L) out of two genes related to endoplasmic reticulum oxidoreductines, and two (CANX and DDIT3) out of three genes previously related to ER-stress induced by acute infection with CDV (251). Taken together, these results can be cautiously interpreted as indicative

of a reduced transcription of genes that are reported to correlate with ER-stress (251,262–265). The hypothesized increased oxidative stress in DH82Ond pi cells compared to non-infected DH82 cells was further investigated by means of immunoreactivity for 8OHdG, SOD2 and CAT, as displayed in Figure 1, as well as by determination of oxidative burst by flow cytometry. Immunofluorescence for 8OHdG lacked a significant difference (p = 0.5476) in the percentage of positive cells between non-infected (median = 96.80%, range: 94.58–100.00%) and DH82Ond pi pellets (median = 99.33%, range: 95.94–99.79%) (Figure 3). Immunofluorescence for SOD2 displayed a significantly (p = 0.0079) increased percentage of positive cells in DH82Ond pi pellets (median = 20.39%, range: 7.75–27.30%) compared to non-infected DH82 pellets (median = 0.00%, range: 0.00%–0.47%) (Figure 3). Immunofluorescence for CAT revealed a significantly (p = 0.0079) increased percentage of positive cells in DH82Ond pi pellets (median = 81.29%, range: 72.92%–90.58%) compared to non-infected DH82 pellets (median = 37.27%, range: 19.61%–39.94%) (Figure 3). The determination of oxidative burst by flow cytometry demonstrated a significantly (p = 0.0017) increased ROS production among DH82Ond pi cells compared to non-infected DH82 cells (Figure 4). Despite a lack of difference in ROS-induced nucleic acid damage as determined by immunofluorescence of 8OHdG, these results are collectively indicative of an increased oxidative stress in DH82Ond pi cells compared to non-infected DH82 cells, which might lead to an increased level of HIF-1α and subsequently to an inhibition of its degradation.

Table 3. Summary of canine gene symbols related to ROS production and scavenging, ER-stress and HIF-1α pathway, differentially expressed between non-infected and persistently canine distemper virus infected DH82 cells, according to the combination of a fold change (FC) filter (FC ≥ 1.5 or ≤ −1.5) and of a statistical significances filter ($p \leq 0.05$).

Canine Gene Symbol	Gene Name	Functional Group	Fold Change	*p*-Value	References
VEGF-B	vascular endothelial growth factor B	HIF-1a downstream	−593.197	<0.001	(103,248,253–255)
THBS2	thrombospondin 2	HIF-1a downstream	−451.295	<0.001	(124)
EDN1	endothelin 1	HIF-1a downstream	−47.795	<0.001	(124)
CXCR4	chemokine (C-X-C motif)	HIF-1a	−13.485	<0.001	(248)

	receptor 4	downstream			
SERPINE1	serine (or cysteine) peptidase inhibitor, clade E, member 1	HIF-1a downstream	−13.116	<0.001	(124,254)
COX7B2	cytochrome c oxidase subunit VIIb2	ROS production; ER stress	−6.015	<0.001	(103,106,255)
ITPR3	inositol 1,4,5-triphosphate receptor, type 3	ER stress	−4.646	<0.001	(252)
THBS1	thrombospondin 1	HIF-1a downstream	−4.461	<0.001	(124)
ERO1L	ERO1-like (*S. cerevisiae*)	ROS production; ER stress	−3.995	<0.001	(252)
Cxcl12	chemokine (C-X-C motif) ligand 12	HIF-1a downstream	−3.683	<0.001	(248)
NT5E	5'-nucleotidase, ecto (CD73)	HIF-1a downstream	−3.041	<0.001	(248)
CANX	calnexin	ER stress	−2.780	<0.001	(251)
TXNRD3	thioredoxin reductase 3	ROS scavenging	−2.464	<0.001	(103,248)
NDUFAF2	NADH dehydrogenase (ubiquinone) 1 alpha subcomplex, assembly factor 2	ROS production; ER stress	−2.292	<0.001	(103,248)
NDUFAB1	NADH dehydrogenase (ubiquinone) 1, alpha/beta subcomplex, 1, 8kDa	ROS production; ER stress	−2.261	<0.001	(103,248)
DDIT3	DNA-damage-inducible transcript 3	ER stress	−2.087	<0.001	(251)
EGLN1	Egl nine homolog 1 (*C. elegans*)	HIF-1a transcription & regulation	−1.976	0.001	(124,251,253,256)

PRDX6	peroxiredoxin 6	ROS scavenging	−1.895	<0.001	(103,248)
EGLN3	egl nine homolog 3 (*C. elegans*)	HIF-1a transcription & regulation	−1.875	0.004	(124,251,253,256)
SDHD	succinate dehydrogenase complex, subunit D, integral membrane protein	ROS production; ER stress	−1.857	<0.001	(103,248)
FGF2	fibroblast growth factor 2 (basic)	HIF-1a downstream	−1.842	0.003	(124)
PDIA6	protein disulfide isomerase family A, member 6	ROS production; ER stress	−1.801	<0.001	(252)
VHL	von Hippel-Lindau tumor suppressor, E3 ubiquitin protein ligase	HIF-1a transcription & regulation	−1.771	0.005	(124,251,253,256)
SOD1	superoxide dismutase 1, soluble	ROS scavenging	−1.712	<0.001	(103,248)
PDIA4	protein disulfide isomerase family A, member 4	ROS production; ER stress	−1.678	0.010	(252)
ADM	adrenomedullin	HIF-1a downstream	−1.665	<0.001	(124)
GSS	glutathione synthetase	ROS scavenging; ER stress	−1.648	0.001	(252)
NDUFC2	NADH dehydrogenase (ubiquinone) 1, subcomplex unknown, 2, 14.5kDa	ROS production; ER stress	−1.630	0.001	(103,248)
GCLM	glutamate-cysteine ligase, modifier subunit	ROS scavenging; ER stress	−1.565	<0.001	(252)

PDIA3	protein disulfide isomerase family A, member 3	ROS production; ER stress	−1.533	0.001	(252)
CD274	CD274 molecule	HIF-1a downstream	−1.515	0.025	(248)
PDGFRL	platelet-derived growth factor receptor-like	HIF-1a downstream	1.554	0.004	(248)
UQCR11	ubiquinol-cytochrome c reductase (6.4kD) subunit	ROS production; ER stress	1.563	0.002	(103,248)
UQCRC2	ubiquinol cytochrome c reductase core protein 2	ROS production; ER stress	1.590	0.021	(103,248)
NDUFS1	NADH dehydrogenase (ubiquinone) Fe-S protein 1, 75kDa (NADH-coenzyme Q reductase)	ROS production; ER stress	1.622	<0.001	(103,248)
NCF2	neutrophil cytosolic factor 2	ROS production	1.639	0.004	(103)
UQCRC1	ubiquinol-cytochrome c reductase core protein 1	ROS production; ER stress	1.678	<0.001	(103,248)
ITPR1	inositol 1,4,5-triphosphate receptor, type 1	ER stress	1.844	0.001	(252)
NDUFS7	NADH dehydrogenase (ubiquinone) Fe-S protein 7, 20kDa (NADH-coenzyme Q reductase)	ROS production; ER stress	1.846	<0.001	(103,248)
LONP1	lon peptidase 1, mitochondrial	ER stress	1.850	0.001	(252)
CCL2	chemokine (C-C motif) ligand 2	HIF-1a downstream	1.866	<0.001	(103,124)
HMOX1	heme oxygenase (decycling) 1	ROS scavenging	1.940	<0.001	(103)

NDUFA10	NADH dehydrogenase (ubiquinone) 1 alpha subcomplex, 10, 42kDa	ROS production; ER stress	2.009	<0.001	(103,248)
PDGFA	platelet-derived growth factor alpha polypeptide	HIF-1a downstream	2.089	<0.001	(248)
PPID	peptidylprolyl isomerase D (cyclophilin D)	ER stress	2.286	<0.001	(103,248)
NDUFV3	NADH dehydrogenase (ubiquinone) flavoprotein 3	ROS production; ER stress	2.362	<0.001	(103,248)
ALOX5AP	arachidonate 5-lipoxygenase-activating protein	ROS production	2.509	<0.001	(255)
COX17	COX17 homolog, cytochrome c oxidase assembly protein	ROS production; ER stress	2.557	0.001	(103,106,255)
CAT	Catalase	ROS scavenging	3.584	<0.001	(103,248)
NQO1	NAD(P)H dehydrogenase, quinone 1	ROS scavenging	3.868	<0.001	(103)
XDH	xanthine dehydrogenase	ROS production; ER stress	3.913	0.002	(103,252,255)
KITLG	KIT ligand	HIF-1a downstream	4.174	<0.001	(248)
LOC100856470	peroxiredoxin-2-like	ROS scavenging	5.351	<0.001	(103,248)
TEK	endothelial-specific receptor tyrosine kinase	HIF-1a downstream	5.639	<0.001	(124,248,254)
PDGFC	platelet derived growth factor C	HIF-1a downstream	6.578	<0.001	(248)
TXNIP	thioredoxin interacting protein	ROS scavenging	11.227	0.001	(103)
NCF4	neutrophil cytosolic factor	ROS	67.304	<0.001	(103,254)

	4, 40kDa	production	

Green labeling refers to down-regulated genes; red refers to up-regulated genes. ER, endoplasmic reticulum; HIF-1α, hypoxia-inducible factor 1α; ROS, reactive oxygen species. “HIF-1α transcription & regulation” is the abbreviation for “HIF-1α activation, transcriptional activity and regulation” functional group; “HIF-1α downstream” is the abbreviation for “HIF-1α angiogenic downstream pathway” functional group

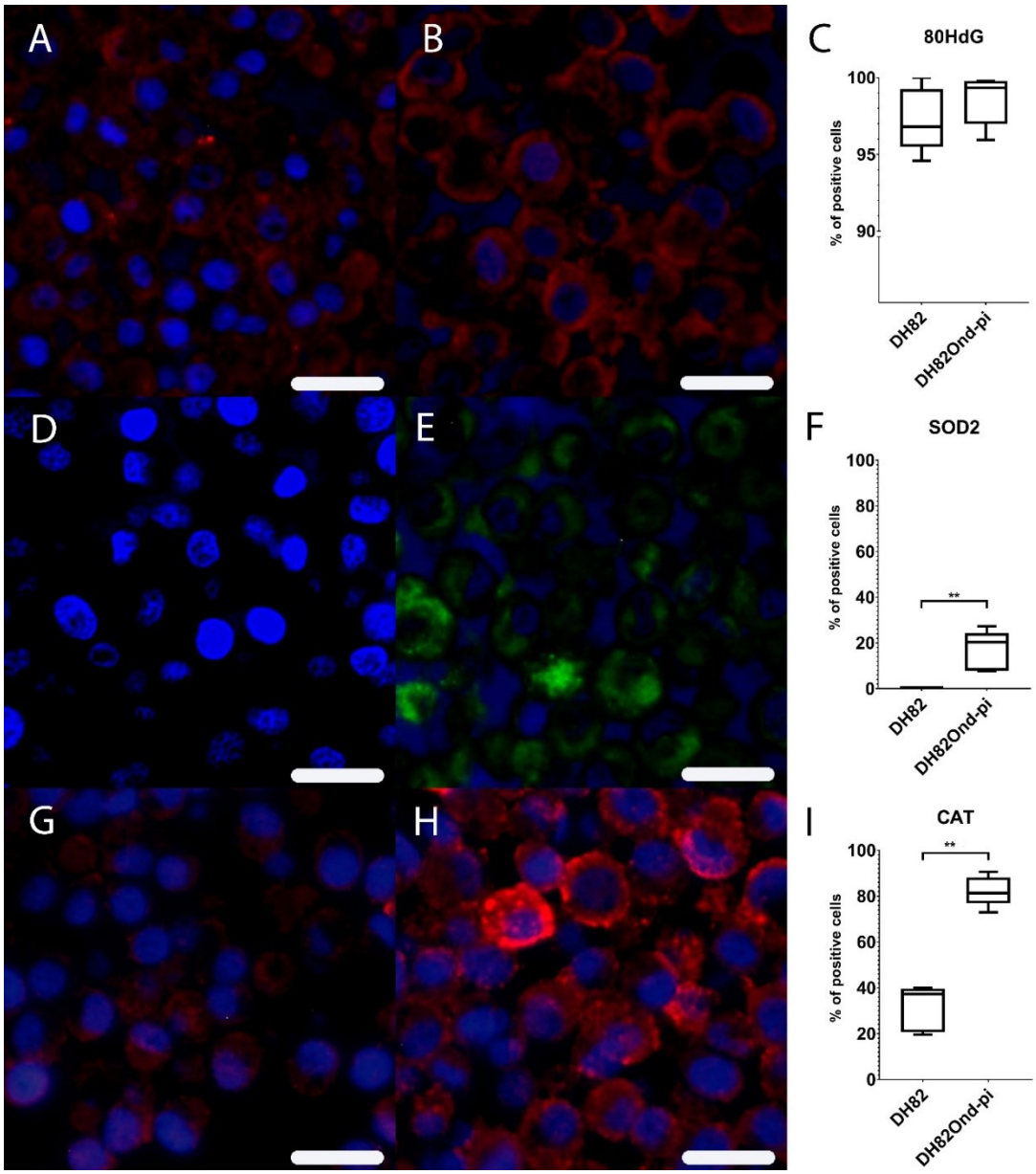

*Figure 3: Immunofluorescence analysis revealed a lower expression of markers associated with oxidative stress in non-infected (A,D,G) compared to persistently canine distemper virus (CDV) infected (B,E,H) DH82 cells. Staining for 8OHdG (Cy3, red) and bisbenzimide (nuclei, blue) revealed a similar expression in non-infected (A) and persistently CDV-infected (B) DH82 cells as graphically shown in (C). Staining for superoxide dismutase (Cy2, green) and bisbenzimide (nuclei, blue) showed a significantly lower expression in non-infected (D) compared to persistently CDV-infected DH82 (E) cells as graphically depicted in (F). Staining for catalase (Cy3, red) and bisbenzimide (nuclei, blue) demonstrated a significantly lower expression in non-infected (G) compared to persistently CDV-infected (H) DH82 cells as graphically shown in (I). Bar = 20µm. (C), (F) and (I) display box and whisker plots with median values, quartiles and maximum and minimum values. Significant differences ($p \leq 0.05$, Mann–Whitney U-test) are labeled by asterisks (** $p \leq 0.01$). From Armando et al 2020*

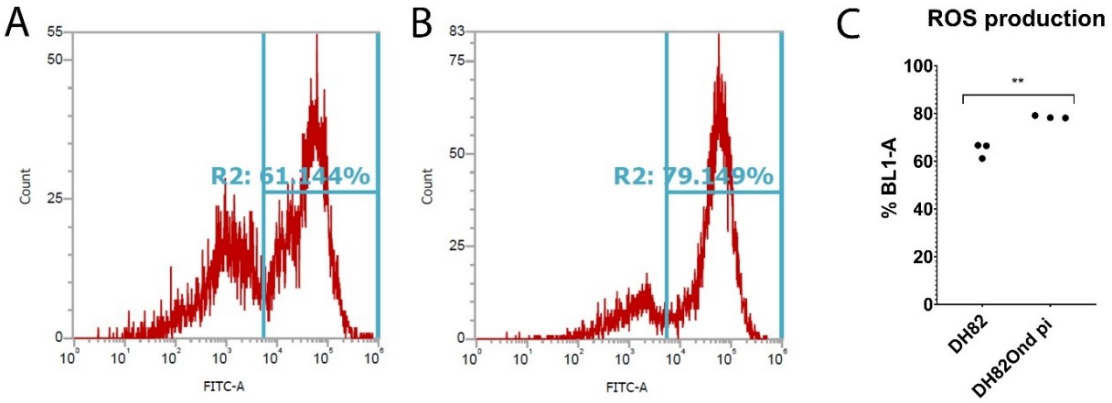

*Figure 4: Determination of oxidative burst by fluorescence activated cells sorting (FACS) in non-infected (A) and persistently canine distemper virus (CDV) infected (B) DH82 cells. The percentage of cells positive for ROS-formation was measured by flow cytometry (BL-1) using a DCF fluorescence probe. (C) BL-1 positive cells revealed a significantly increased ROS production among persistently CDV-infected DH82 cells compared to non-infected controls. All data are shown as dot plots with means ± standard error of mean. Significant differences ($p \leq 0.05$, unpaired t-test) are labeled by asterisks (** $p \leq 0.01$). From Armando et al 2020*

DH82Ond pi are characterized by an increased HIF-1α protein expression associated with an altered intracellular distribution

Among the gene symbols referring to the functional group "HIF-1α activation, transcriptional activity and regulation", three out of 15 genes were down-regulated (Table 3). Specifically, down-regulated gene symbols were those referring to two (ENGL1 and ENGL3) out of three prolyl hydroxylases and to von Hippel-Lindau (VHL) protein, while HIF-1α gene symbol (HIF1A) did not show any significant change (Supplementary Table 2). Immunoreactivity for HIF-1α revealed a significant ($p = 0.0079$) higher percentage of positive DH82Ond pi cells (median = 36.95%, range 28.83%–39.99%) compared to non-infected DH82 cells (median = 2.53%, range: 2.24%–9.51%), as shown in Figure 5. In non-infected DH82 cells, HIF-1α was mainly expressed within nucleus (median = 43.69%, range: 4.76%–69.49%) and cytoplasm (median = 30.38%, range: 20.31%–95.24%) and only to a lesser extent in the membrane (median: 20.75%, range: 0.00%–35.94%), without significant differences (p ranging from 0.1980 to >0.9999) between the three localizations. Interestingly, DH82Ond pi cells displayed a significantly higher HIF-1α expression in the membrane (Figure 5) compared to nuclear ($p = 0.0486$; membrane median = 64.74%, membrane range: 22.80%–85.02%; nuclear median = 14.06%, nuclear range: 4.20%–29.05%) but not to cytoplasmic localizations ($p = 0.0710$; cytoplasm median = 21.01%, cytoplasm range: 10.78%–25.58%). Additionally, the membranous immunopositivity for HIF-1α in DH82Ond pi cells was significantly ($p = 0.0317$) higher when compared to the corresponding localization in non-infected DH82 cells. HIF-1 α immunoblotting confirmed the significantly increased protein

expression ($p = 0.0027$) in DH82Ond pi cells when compared to the non-infected DH82 cells (Figure 6). Summarized, these results are indicative of an increased level of HIF-1α in DH82Ond pi, which is most likely due to a decreased cytoplasmic degradation. To further characterize the intracellular localization of HIF-1α, immunoelectron microscopy and laser scanning confocal microscopical analysis of double stainings were performed.

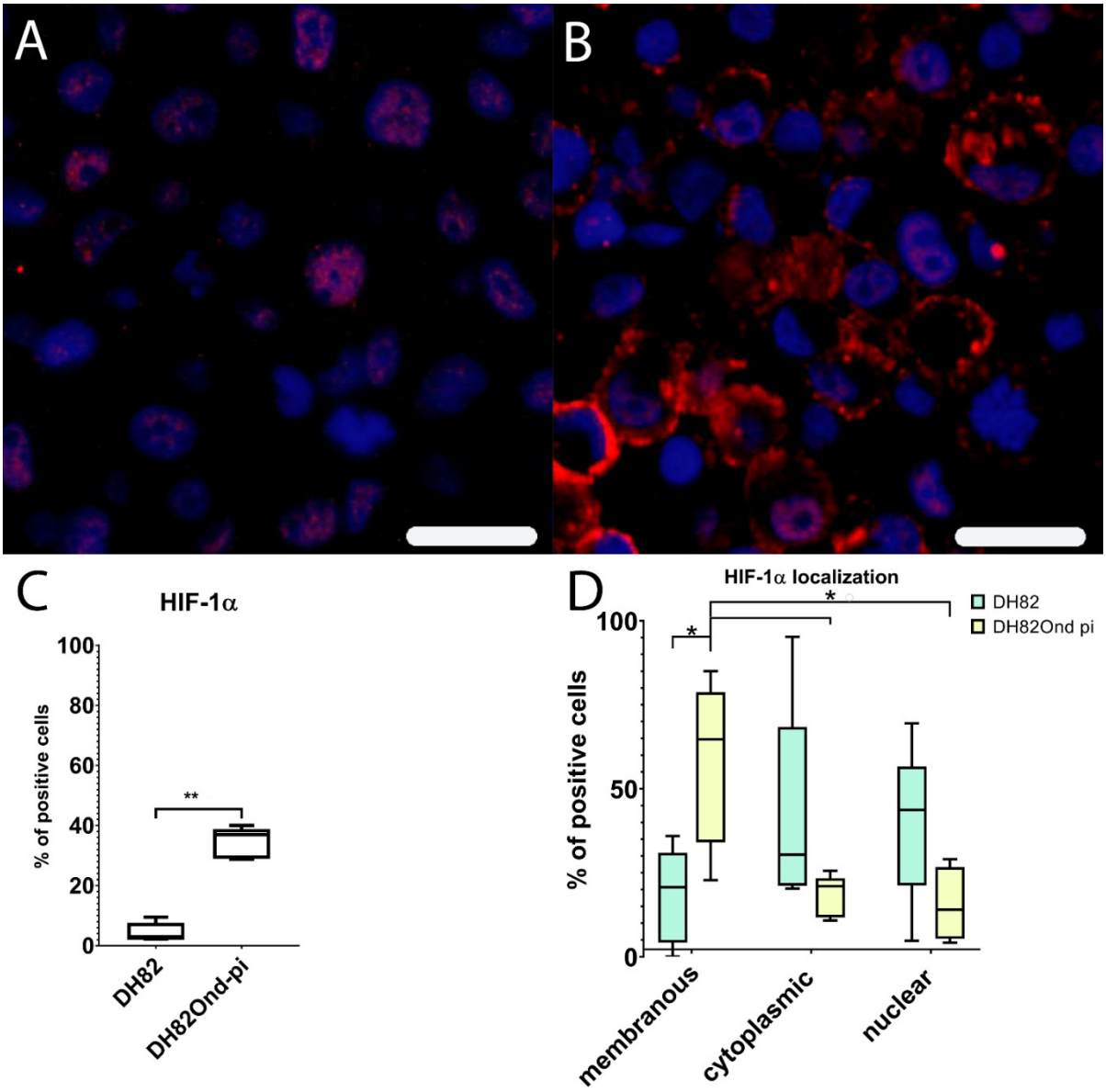

Figure 5: Immunofluorescence analysis for HIF-1α expression (Cy3, red; bisbenzimide, blue, nuclei) reveals a lower membranous expression in non-infected (A) compared to persistently canine distemper virus (CDV) infected (B) DH82 cells. Non-infected DH82 cells frequently displayed a nuclear immunolabeling (A) whereas a frequent membrane-associated staining was observed in persistently CDV-infected DH82 cells (B). Bar = 20µm. HIF-1α shows a significantly increased percentage of positive cells in persistently CDV-infected DH82 cells compared to non-infected controls (C). (D) Within non-infected DH82 cells, HIF-1α was present within nucleus and cytoplasm without significant differences between the localizations. In contrast, persistently CDV-infected DH82 cells displayed a significantly higher membranous HIF-1α expression compared to nuclear ($p = 0.0486$) but not to cytoplasmic ($p = 0.0710$) localizations. Additionally, the membranous immunopositivity for HIF-1α in persistently CDV-Ond infected DH82 cells was significantly higher compared to the corresponding localization in non-infected controls. Box and whisker plots display median and quartiles with maximum and minimum values. Significant differences ($p \leq 0.05$, Mann–Whitney U-test (C,D) and Kruskall-Wallis test with post-hoc Dunn's test (D)) are labeled by asterisks ($p \leq 0.05$ and ** $p \leq 0.01$). From Armando et al 2020*

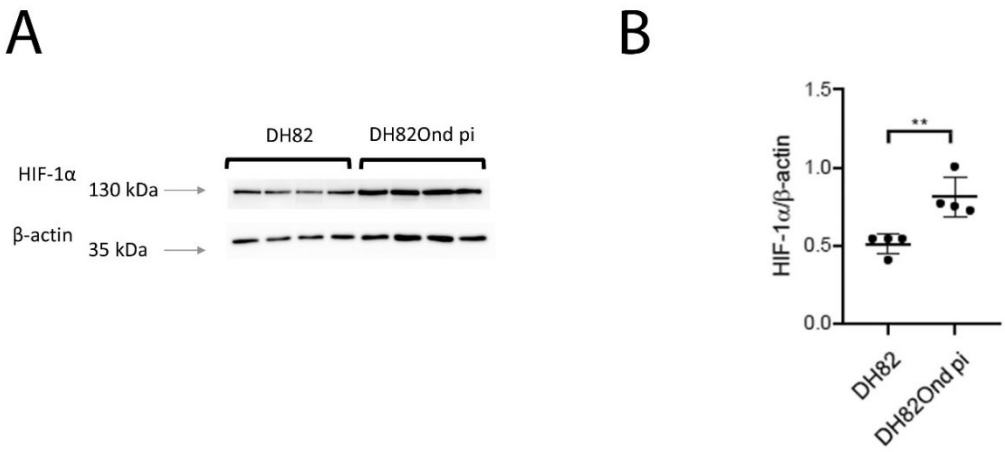

*Figure 6: Immunoblotting with anti-HIF-1α and anti-β-actin antibodies revealed a single band of approximately 130 kDa and 43 kDa, respectively, when compared to the corresponding marker lengths of 130 kDa and 35 kDa (arrows, A). (B) Band intensities and sizes of both HIF-1α and beta-actin were quantified and their ratio determined, revealing a significant increase of HIF-1α in persistently canine distemper virus (CDV)-infected DH82 cells compared to non-infected controls. Dot plots display means and standard deviation. Significant differences ($p \leq 0.05$, unpaired t-test.) are labeled by asterisks (** $p \leq 0.01$). From Armando et al 2020.*

DH82Ond pi show an unusual mainly sub-membranous distribution of HIF-1α

Ultrastructural investigation of DH82Ond pi by immunoelectron microscopy for HIF-1α revealed that this protein was mostly localized in the sub-membranous compartment as well as within variably sized, round, moderately to highly electrondense vesicles (Figure 7). Based on the assumptions that many viruses have been shown to induce an increased production of $CD63^+$ exosomes (266), and that viral proteins can be stored within endolysosomal system (267), DL-IF for HIF-1α in association with different markers was performed and evaluated by laser scanning confocal microscopy. To verify the specificity of the membranous staining, DL-IF for HIF-1α in association with WGA was performed, confirming a membranous to sub-membranous localization of HIF-1α without overlapping co-staining of the two markers (Supplementary Figure 4). To investigate whether HIF-1α was associated with exosomes, DL-IF in association with CD63 was performed, revealing an occasional co-localization of the two markers (Figure 8). To exclude an HIF-1α storage within the Golgi apparatus, DL-IF in association with GM-130 was performed, clearly showing that HIF-1α was not localized within this cell organelle (Supplementary Figure 4). Finally, to analyze whether HIF-1α was associated with CDV-NP, DL-IF in association with CDV-NP was performed, revealing a marked and diffuse co-localization of the two markers (Figure 8). In summary, these results confirmed an unexpected localization of HIF-1α in the sub-membranous compartment of DH82Ond pi cells, being occasionally associated with $CD63^+$ exosomes and more frequently with CDV-NP. To investigate

if this unusual localization of HIF-1α can affect the expression of its angiogenetic downstream molecules with a special focus on VEGF-B, further microarray data and immunofluorescence analyses were performed.

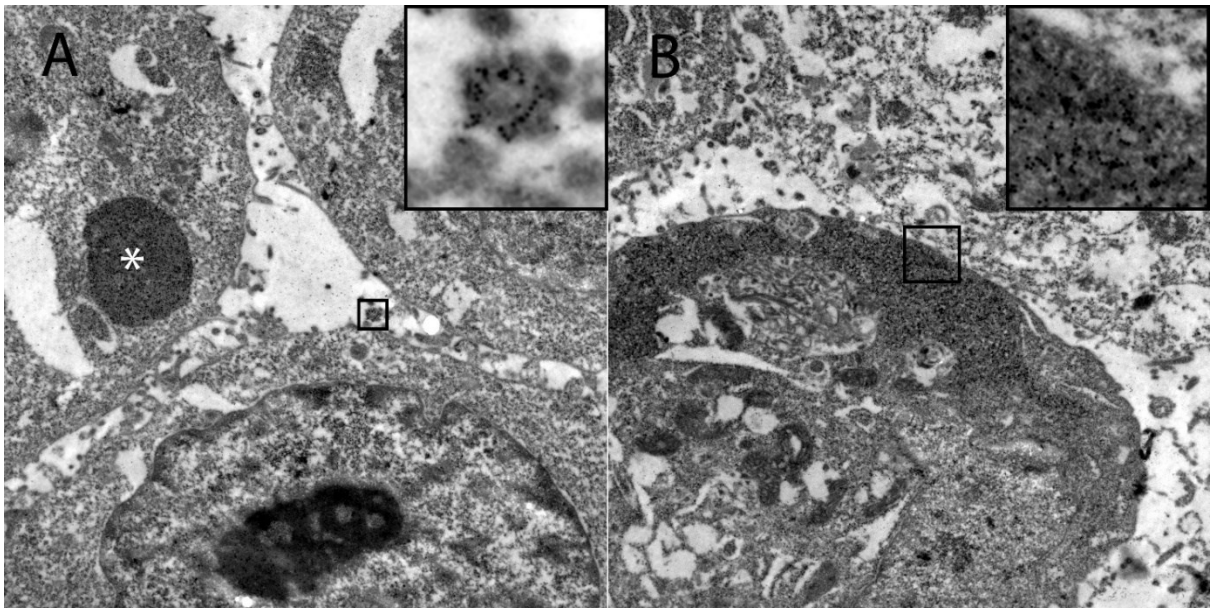

Figure 7: Demonstration of the intracellular HIF-1α localization in persistently canine distemper virus infected DH82 cells as determined by immunoelectron microscopy. (A) HIF-1α was found within variably sized, round, moderately to highly electrondense vesicles (insert) and in large moderately electrondense vacuoles (*). Additionally, HIF-1α was detected often in the sub-membranous area of the cytoplasm (insert; B). Magnification 9000×. From Armando et al. 2020.

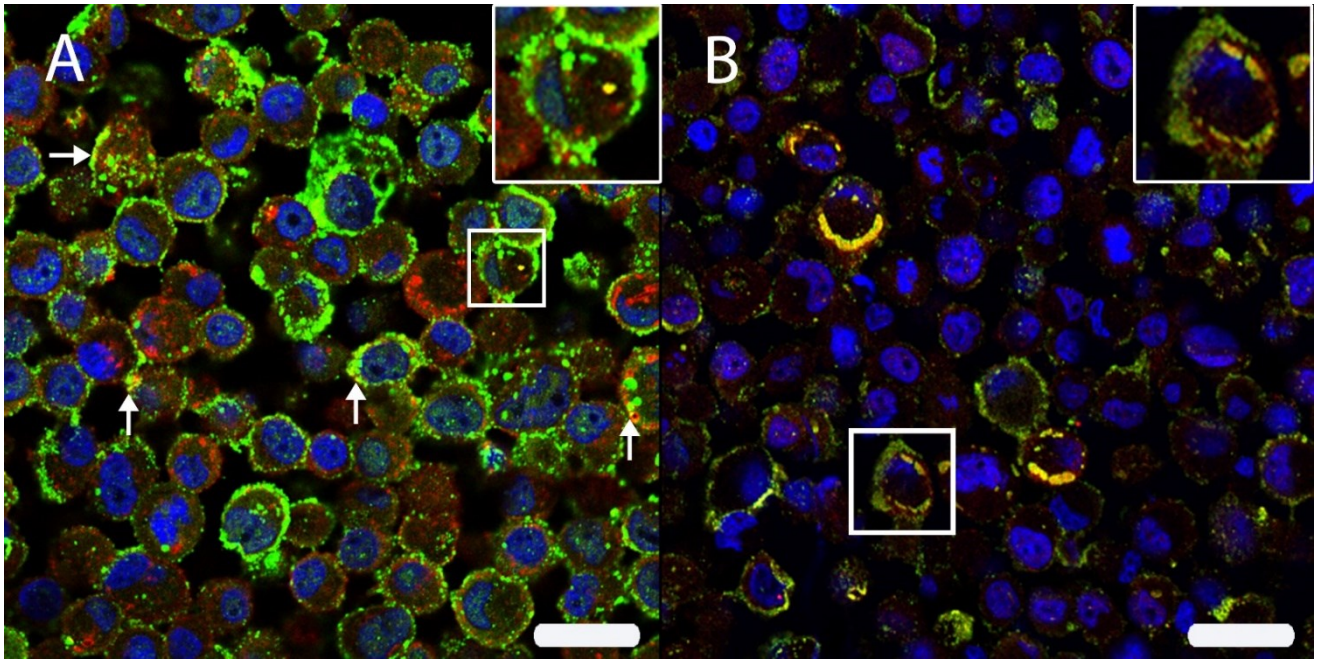

Figure 8: (A) The intracellular HIF-1α localization was analyzed by double immunofluorescence with HIF-1α (Cy2, green) and CD63 (Cy3, red) in persistently canine distemper virus (CDV)-infected DH82 cells. Both proteins were localized within cell membranes and cytoplasm. Interestingly, an occasional co-expression (yellow) was noted (arrows; insert) using scanning confocal laser microscopy. (B) A double labeling directed against HIF-1α (Cy3, red) and the CDV nucleoprotein (CDV-NP; Cy2, green) revealed a frequent co-localization (yellow) beneath the cell membrane and within the perinuclear area (insert) of persistently CDV-infected DH82 cells. Nuclei were stained with bisbenzimide (blue). Bar = 20 µm. From Armando et al. 2020.

Unexpected intracellular HIF-1α localization is associated with a dysregulated expression of angiogenetic downstream targets

Among the gene symbols referring to the functional group "HIF-1α angiogenic downstream molecules", six out of 45 genes were up-regulated, whereas 11 genes were down-regulated (Table 3). Specifically, down-regulated gene symbols included those related to the expression of angiogenetic and anti-angiogenetic macromolecules which transcription is directly induced by the activation of the HIF-1α downstream pathway (i.e. vascular endothelial growth factor B—VEGFB; thrombospondin 2—THBS2; endothelin 1—EDN1/ET1; serine peptidase inhibitor E—SERPINE1; thrombospondin 1—THBS1; chemokine ligand 12—Cxcl12; CD73—NT5E; basic fibroblast growth factor 2—FGF2, adrenomedullin—ADM; CD274). Immunofluorescence for VEGF-B revealed a significantly ($p = 0.0079$) decreased percentage of immunopositive cells in DH82Ond pi pellets (median = 20.17%, range: 11.52%–22.18%) compared to non-infected DH82 pellets (median = 71.41%, range: 64.00%–82.76%), as shown in Figure 9. Taken together, these results are indicative of a reduced activation of the HIF-1α angiogenic downstream pathway. This

is most likely due to an excessive, unusually localized, and non-functional protein expression of HIF-1α, which might be the consequence of a decrease in its cytoplasmic degradation following a virus-induced increased oxidative stress.

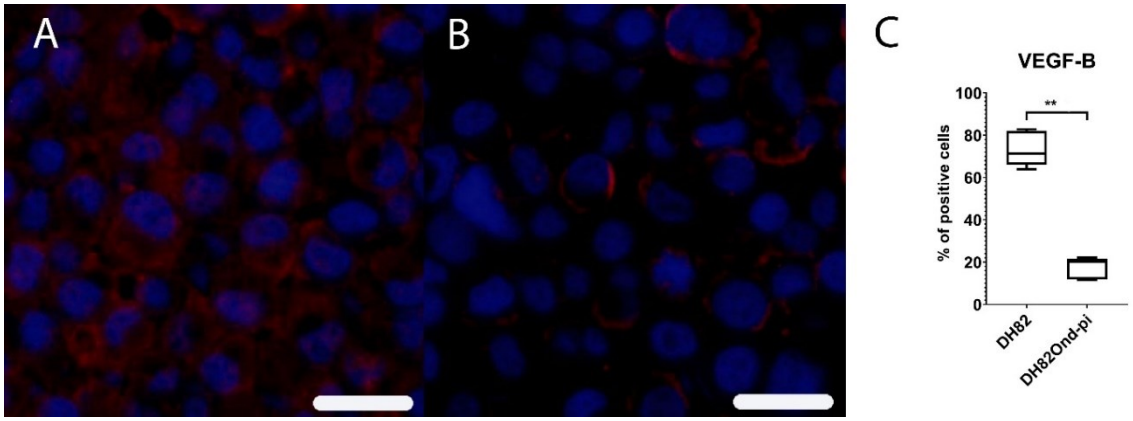

*Figure 9: Immunofluorescence analysis for vascular endothelial growth factor B (VEGF-B, Cy3, red) revealed a high expression of this marker in non-infected DH82 cells (A), whereas a low expression was present in persistently canine distemper virus (CDV)-infected DH82 cells (B); Bar = 20 µm. This statistically significant difference is graphically shown in (C). Box and whisker plots display median and quartiles with maximum and minimum values. Significant differences ($p \leq 0.05$, Mann–Whitney U-test) are labeled by asterisks (** $p \leq 0.01$). From Armando et al 2020.*

IN VITRO STUDY 2

Persistent CDV-Ond infection of DH82 cells leads to morphological changes while growth features remain unaltered

The infection status of DH82Ond pi cells was assessed via immunofluorescence staining for CDV-NP. While immunoreactivity for CDV-NP of DH82Ond pi cells showed an average of 97.5% infected cells (median: 97.5%; range: 96%-99%), all non-infected DH82 cells were negative (Supplementary Figure 3). The cumulative population doubling assay did not show any difference ($p = 0.6347$) between non-infected and persistently CDV-Ond infected DH82 cells (Supplementary Figure 5). Interestingly, both non-infected and persistently CDV-infected DH82 cells displayed morphological changes dependent of the time point post-seeding. DH82Ond pi cells exhibited an increased percentage of round cells starting at 3 days post-seeding accompanied by a decrease of the others 3 morphological phenotypes (triangle, cigar and slender) as shown in (Supplementary Figure 6). From 5 to 7 days post-seeding, round cells predominated among DH82Ond pi cells. Non-infected DH82 cells showed a highly pleomorphic phenotype during the first 2 days post-seeding with an increased presence of the triangle and cigar-shaped phenotypes. From days 5 to 7 post-seeding, there was a mild increase in the percentage of round cells but with a constant presence of the 3 other morphological phenotypes, resulting in a moderately to highly pleomorphic appearance of non-infected cultures at all time points investigated (Supplementary Figure 7). Summarized, these results highlighted that a persistent CDV infection of DH82 cells did not alter cell growth features but led to morphological changes. Assuming that morphological alterations of the cell shape are a feature of MET associated with changes in epithelial and mesenchymal markers; further investigations were performed to verify the occurrence of this phenomenon in non-infected and persistently CDV- Ond infected DH82 cells.

DH82Ond pi cells display an increased expression of epithelial markers on a protein level

Immunofluorescence of DH82Ond pi cells displayed an increased number of cells expressing β-catenin (Figure 10 A-C; mean = 33%; median = 32%; range: 28%-34%) compared to non-infected controls (mean = 18%; median = 17%; range: 12%-29%). However, this in- crease was not statistically significant ($p = 0.0792$). The expression of β-catenin showed no significant differences between the different cell phenotypes and with respect to the localization within the cells (Figure 10 D-E). Immunoreactivity for E-cadherin (Figure 10 F-H) revealed a significantly ($p = 0.0139$) increased number of immunopositive DH82Ond pi cells (mean = 59%; median = 58%; range: 51%-67%) compared to non-infected controls (mean = 34%; median = 29%; range: 24%- 49%). When evaluated based on the different cell phenotypes, no statistical differences were detected between non-infected and DH82Ond pi cells (Figure 10 I). Non-infected DH82 cells displayed a significantly ($p = 0.0016$) higher 'membranous to cytoplasmic' ex- pression of E-cadherin (Figure 10 J). On the other hand, DH82Ond pi cells exhibited an increased focal cytoplasmic E-cadherin expression compared to non-infected controls, despite not reaching statistical significance ($p = 0.0846$). The unexpected E-cadherin localization was firstly verified by laser scanning confocal microscopy of single-la- belling immunofluorescence stains (Figure 10 G, insert). Furthermore, 3D reconstructions obtained from double-labelling immunofluorescence combining E-cadherin with WGA (Figure 11 A-C) confirmed that E-cadherin within DH82Ond pi cells often localized in a cytoplasmic immunopositive focal area of variable size, which surrounded the Golgi apparatus without localizing within the latter. On the other hand, non-infected controls showed also a membranous to cytoplasmic E-cadherin expression pattern, confirming the results observed with single-labelling immunofluorescence (Figure S6). Immunolabelling for cytokeratin 8 (Figure 10 K-M) lacked a significant difference ($p = 0.0688$) in the percentage of positive cells be- tween DH82Ond pi (mean = 45%; median = 49%; range: 38%-50%) and non-infected controls (mean = 33%; median = 33%; range: 28%- 39%). Evaluation based on the different cell phenotypes revealed no statistically significant differences in the expression of cytokeratin 8 between DH82Ond pi and non-infected controls (Figure 10 N). However, DH82Ond pi cells displayed a significantly ($p < 0.0001$) higher 'membranous to cytoplasmic' expression of this protein com- pared to non-infected controls (Figure 1O), while the diffuse cytoplasmic localization did not reach statistical significance ($p = 0.8340$). Interestingly, cytokeratin 8 displayed a focal cytoplasmic expression that was significantly ($p < 0.0001$) more often observed in non-infected controls compared to persistently CDV-infected DH82

cells (Figure 10 O). Similarly to E-cadherin, the focal cytoplasmic localization of this marker in non-infected DH82 cells was initially confirmed by laser scanning confocal microscopy of single-labelling immunofluorescence stains (Figure 10 K, insert). Further analyses employing 3D reconstructions of double-labelling immunofluorescence combining cytokeratin 8 and WGA (Figure 11 D-F) confirmed a focal cytokeratin 8 localization within non-infected DH82 cells, revealing a variably sized and shaped immunopositive area located near the nucleus and the Golgi apparatus. Occasionally, also a membranous to cytoplasmic expression of the protein was detected in non-infected controls. DH82Ond pi cells were analyzed accordingly confirming a membranous to cytoplasmic expression of cytokeratin 8, which was frequently arranged in variably sized aggregates (Supplementary Figure 8). Additional single-labelling immunofluorescence pictures displaying the intra- cellular distribution of β-catenin, E-cadherin and cytokeratin 8 in non-infected and persistently CDV-infected DH82 cells at different confluences are available as (Supplementary Figure 9). In order to confirm the immunofluorescence results, an immunoblotting for all the investigated epithelial markers was performed (Figure 12 A). Beta-actin was used as a house-keeping protein, lacking differential expression at both the gene (fold change: 1.06; p value < 0.001) and the protein level ($p = 0.8446$) between non-infected and DH82Ond pi cells. DH82Ond pi cells contained a significantly higher amount of E-cadherin ($p = 0.0192$) compared to non-infected controls (Figure 12 B). In addition, a similar higher amount of cytokeratin 8 expression was observed in DH82Ond pi cells compared to non-infected controls ($p = 0.0376$). The β-catenin expression was higher in DH82Ond pi compared to non-infected DH82 cells (Figure 12 B) although this increase did not reach statistical significance ($p = 0.0956$). Further investigations were performed to evaluate the expression of the typical mesenchymal markers (N-cadherin, vimentin) in non-infected and DH82Ond pi cells.

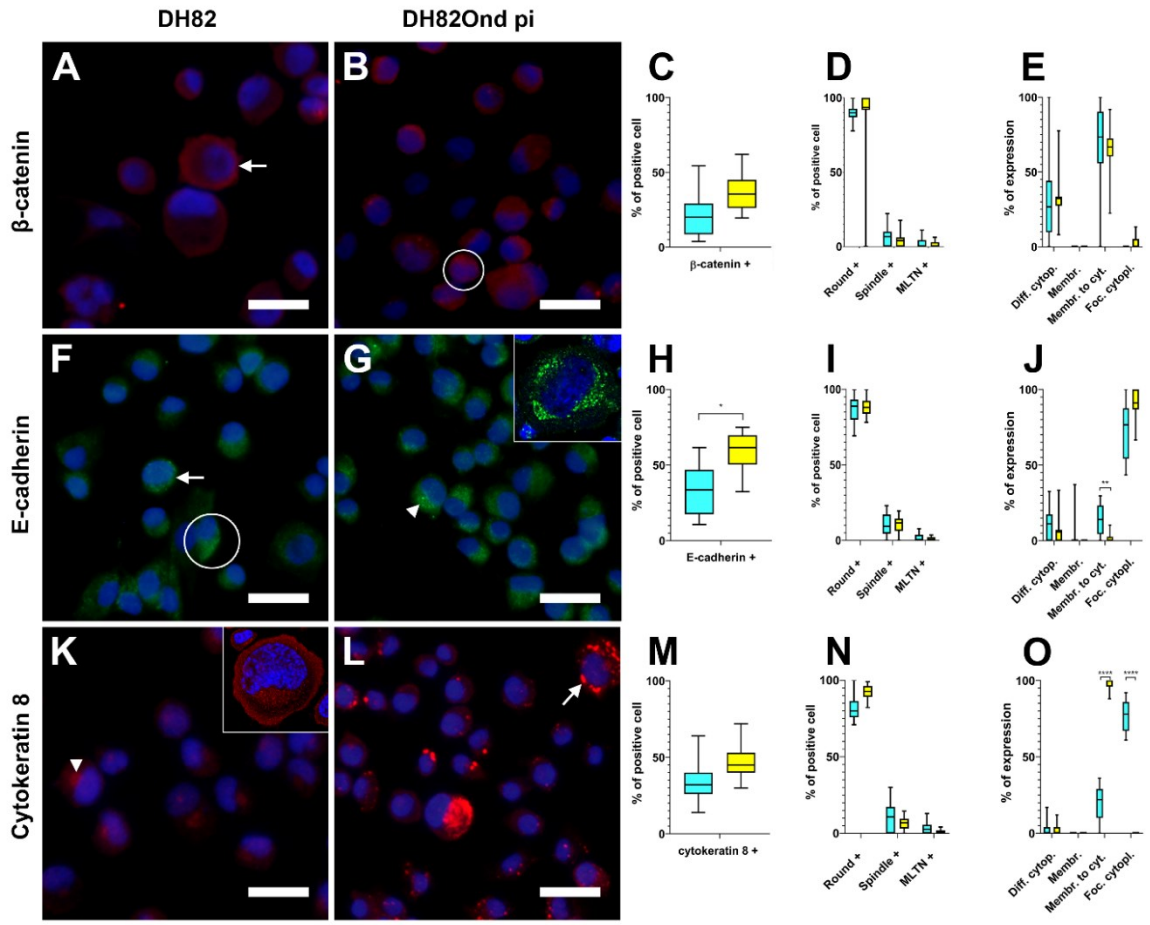

Figure 10: Immunofluorescence for epithelial markers in non-infected (A, F, K) and persistently CDV-infected DH82 cells (B, G, L). Nuclei were labeled with bisbenzimide (blue). Graphs show immunofluorescence results for epithelial markers analyzed in non-infected and persistently CDV infected DH82 cells according to overall percentage of positive cells for each marker (C, H, M), cellular morphology (D, I, N) and intracellular localization (E, J, O). Staining for β-catenin (Cy3, red) revealed that both non-infected (A) and persistently CDV-infected DH82 cells (B) expressed this protein, with an intracellular distribution pattern mainly ranging from "membranous to cytoplasmic" (A, arrow) to and diffuse cytoplasmic (B, encircled). β-catenin expression was increased in DH82Ond pi compared to non-infected controls, but did not reach statistical significance (C). No differences in β-catenin expression were detected neither according to cell morphology (D) nor in intracellular distribution (E). Staining for E-cadherin (Cy2, green) showed the expression of this protein in both non-infected (F) and DH82Ond pi cell (G), with an intracellular distribution pattern ranging from "membranous to cytoplasmic" (A, arrow) to diffuse (A, encircled) and focal cytoplasmic (B, arrowhead), as confirmed by laser scanning confocal microscopy (G, insert). A significantly higher number of DH82Ond pi cells expressed E-cadherin compared to non-infected controls (H). The expression of E-cadherin did not differ between non-infected and infected cells based on different morphologies (I). Non-infected DH82 cells showed a significantly higher "membranous to cytoplasmic" expression of E-cadherin compared to DH82Ond pi cells (J). Staining for cytokeratin 8 (Cy3, red) demonstrated that both non-infected (K) and persistently CDV-infected DH82 cells (L) expressed this protein, with an intracellular distribution pattern mainly ranging from focal cytoplasmic (K, arrowhead) as confirmed by laser scanning confocal microscopy (K, insert), to "membranous to cytoplasmic" (L, arrow). DH82Ond pi cells displayed an increased expression of cytokeratin 8, despite not statistically significant (M). The expression of cytokeratin 8 displayed no

significant differences between non-infected and infected cells based on different morphologies (N). DH82Ond pi cells showed a significantly higher "membranous to cytoplasmic" expression of cytokeratin 8 while non-infected controls exhibited a significantly higher focal cytoplasmic expression (O). Bar=20µm, Box and whisker plots with median values, quartiles and maximum and minimum values. Significant differences (p≤0.05, Student´s t test) are labeled by asterisks. Graph legend: light blue = DH82 cells; yellow = DH82Ond pi cells; Diff. cytopl. = diffuse cytoplasmic; Membr. = membranous; Membr. to cyt. = membranous to cytoplasmic; Foc. cytopl. = focal cytoplasmic; MLTN + = positive multinucleated tumor cells. From Armando et al 2020.

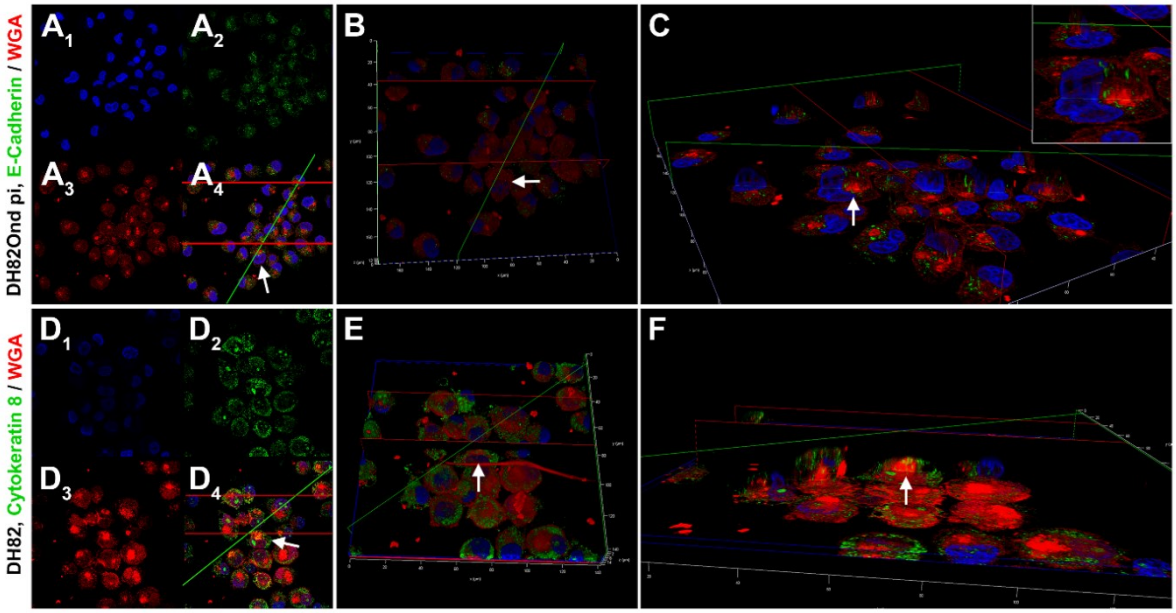

Figure 11: 3D reconstructions from double labeling immunofluorescence of DH82Ond pi and non-infected DH82 cells stained for E-cadherin / WGA (A-C) and cytokeratin 8 / WGA (D-F), respectively. (A) 2D pictures of DH82Ond pi cells from z-stacks obtained with laser scanning confocal microscopy. The single channel view are: nuclei in blue , stained with bisbenzimide (A1); E-cadherin in green, stained with Alexa Fluor 488 (A2); and WGA in red, conjugated with Alexa Fluor 633 (A3). In addition, the picture shows a merged 3 channels view (A4). (B) Top view of the 3D reconstruction obtained from the z-stack in A, with the total cell volume represented by WGA in red. E-cadherin was only occasionally expressed on the cell surface. (C) Section-view of the 3D reconstruction in B, showing the model sectioned along the green and red planes to better display the E-cadherin expression (green) within the cell volume (red). The protein was frequently localized in a focal area near the nucleus surrounding the Golgi apparatus (C, insert), mainly not extending to intermingle with the cell membrane. Each arrow represents the same cell from the z-stack picture to the 3D section-view. 3D reconstruction of DH82Ond pi double immunolabeling for E-cadherin / WGA was obtained by 135 z-stack frames (0.13 µm steps). (D) 2D pictures of non-infected DH82 cells from z-stacks obtained with laser scanning confocal microscopy. The single channel view are: nuclei in blue, stained with bisbenzimide (D1), cytokeratin 8 in green, stained with Alexa Fluor 488 (D2); and WGA in red, conjugated with Alexa Fluor 633 (D3). In addition, the picture shows a merged 3 channels view (D4). (E) Top view of the 3D reconstruction obtained from the z-stack in D, with the total cell volume represented by WGA in red. Cytokeratin 8 expression was also detected on the cell surface, supporting the evidnce of a "membranous to cytoplasmic" distribution pattern. (F) Section-view of the 3D reconstruction in E, showing the model sectioned along the green and the red planes to better display cytokeratin 8 expression (green) within the cell volume (red). The protein mainly showed a focal cytoplasmic, variably extended expression near the nucleus, occasionally localizing above the Golgi apparatus and extending to intermingle with the cell membrane. Each arrow represents the same cells from the z-stack picture to the 3D section-view. 3D reconstruction of non-infected DH82 double immunolabeling for cytokeratin 8 / WGA was obtained by 154 z-stack frames (0.13 µm steps). From Armando et al 2020.

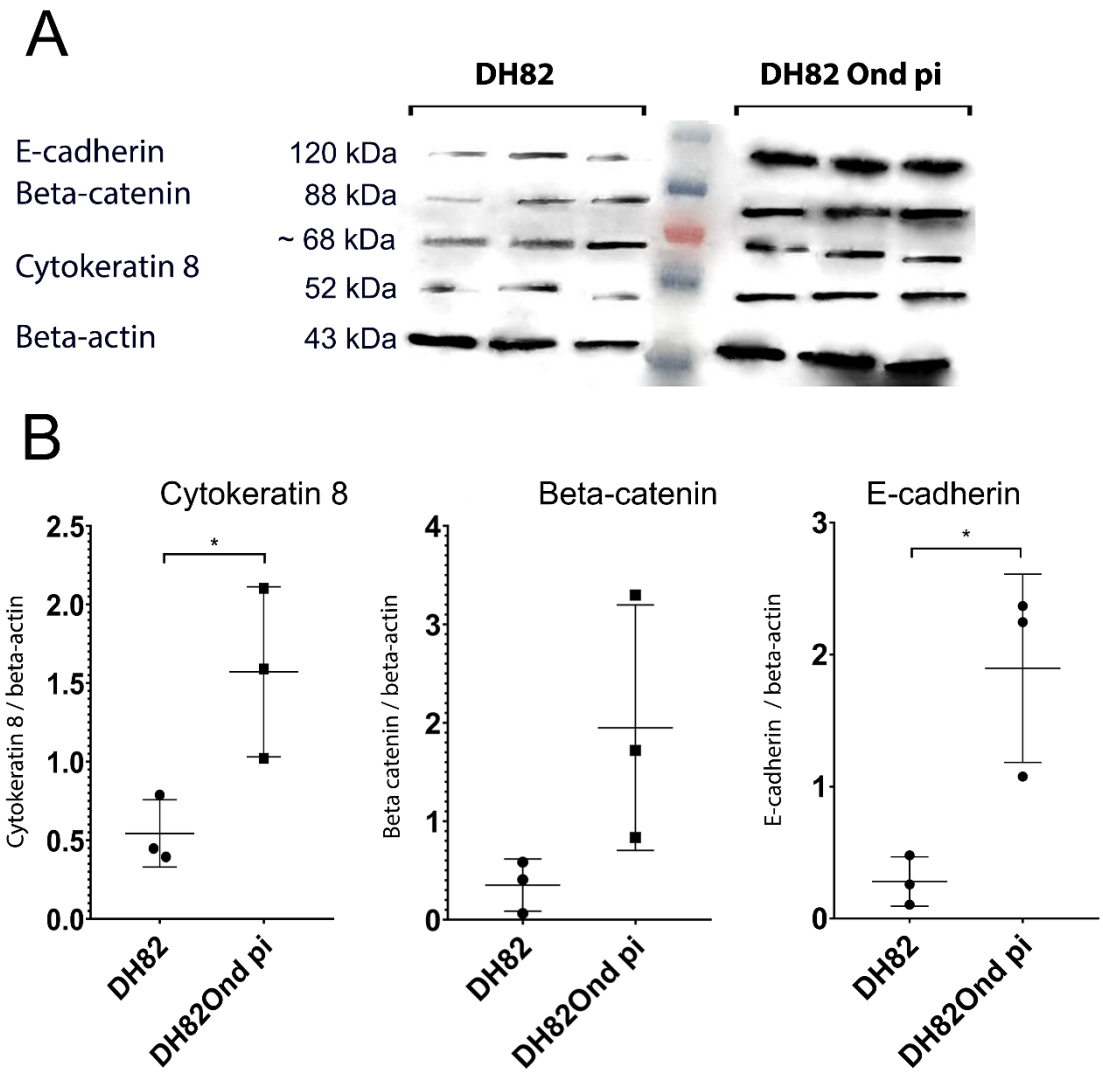

Figure 12: Immunoblotting with anti-cytokeratin 8, anti-β catenin, anti-E-cadherin and anti-β-actin antibodies revealed bands of 52 kDa, 88 kDa, 120 kDa, and 43 kDa, respectively (A). Band sizes and intensities of the aforementioned markers were quantified densitometrically and compared as ratios to β-actin, which was used as a control protein considered that its expression displayed no statistical differences between non-infected and persistently CDV-Ond infected DH82 cells within the densitometric analyses. DH82Ond pi cells displayed a significantly higher amount of cytokeratin 8 and E-cadherin compared to non-infected controls, while β-catenin failed to reach the level of significance. Both non-infected and DH82Ond pi cells displayed bands of unspecific origin of ~68kDa (B). Dot plots show means and standard deviation. Statistically significant differences are labeled by asterisks (p≤0.05). From Armando et al 2020.

DH82Ond pi cells retain mesenchymal marker expression

Mesenchymal marker immunolabelling was analysed as shown in Figure 13. The number of cells expressing N-cadherin (Figure 13 A-C) did not differ significantly ($p = 0.0975$) between non-infected (mean = 16%; median = 17%; range: 11%-21%) and persistently CDV-infected (mean = 8%; median = 7%; range: 5%-13%) DH82 cells. Interestingly, non-infected DH82 cells showed a significantly ($p = 0.0185$) higher number of spindle-shaped cells expressing N-cadherin (Figure 13 D) compared to DH82Ond pi. On the other hand, in DH82Ond pi cells this protein was predominantly expressed in cells with a round morphology, which were significantly more abundant ($p = 0.0156$) compared to the same phenotype among non-infected cells. Non-infected cells demonstrated a significantly higher membranous N-cadherin expression (Figure 13 E) compared to DH82Ond pi cells ($p = 0.0139$). In contrast, persistently CDV-infected DH82 cells exhibited a significantly higher 'membranous to cytoplasmic' expression of N-cadherin compared to non-infected controls ($p = 0.0139$). Non-infected (mean = 98%; median = 99%; range: 97%-99%) and persistently CDV-infected (mean = 98%; median = 98%; range: 97%- 99%) DH82 cells (Figure 13 F-H) lacked a significant difference in the percentage of vimentin-expressing cells ($p = 0.7137$). When evaluated on the basis of the different cell phenotypes, the number of round cells expressing vimentin was significantly ($p = 0.0076$) higher among DH82Ond pi cells compared to non-infected controls. In contrast, non-infected DH82 cells revealed a significantly higher number of vimentin-positive spindle-shaped cells ($p = 0.0016$) compared to DH82Ond pi cells (Figure 13 I). A significantly ($p = 0.0132$) higher percentage of non-infected DH82 cells displayed a diffuse cytoplasmic vimentin expression compared to DH82Ond pi cells (Figure 13 J). In contrast, a significantly ($p = 0.0035$) higher percentage of DH82Ond pi cells showed a focal cytoplasmic expression of vimentin compared to non-infected controls. In order to confirm this finding, a 3D reconstruction from a double-labelling immunofluorescence combining vimentin and WGA was obtained (Figure 14). The 3D reconstructions revealed that non-infected DH82 cells with a round morphology displayed a variably sized and shaped focal immunopositive area located near the nucleus and the Golgi apparatus, which did not expand to the cell membrane. In contrast, spindle-shaped cells exhibited a diffuse cytoplasmic staining that extended until immediately below the cell membrane (Figure 14 A-C). Similar to non-infected cells with a round morphology, DH82Ond pi cells often displayed a focal immunoreactivity not expanding to the cell membrane (Figure 14 D- F). Additional single-labelling immunofluorescence pictures displaying the intracellular distribution of N-cadherin and vimentin in non-infected and persistently CDV-infected DH82 cells at different confluences

are available as (Supplementary Figure 10).

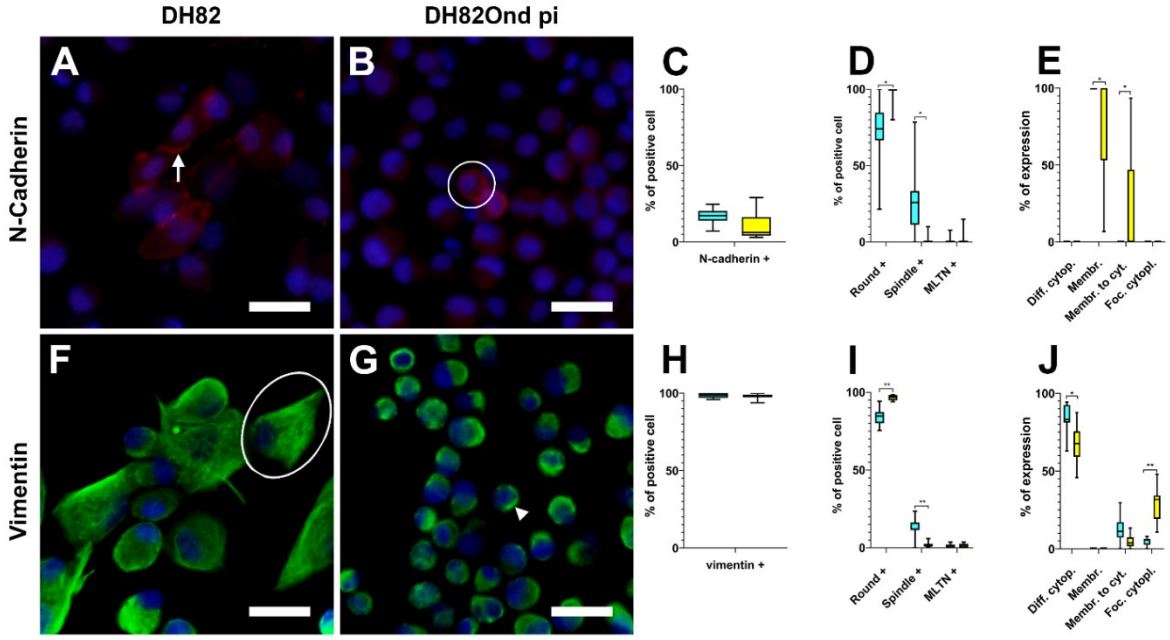

Figure 13: Immunofluorescence results for mesenchymal markers analyzed in non-infected (A,F) and persistently CDV infected DH82 cells (B,G) according to overall percentage of positive cells for each marker (C, H), cellular morphology (D, I) and intracellular localization (E, J). Nuclei were labeled with bisbenzimide (blue). Staining for N-cadherin (Cy3, red) revealed that both non-infected (A) and persistently CDV-infected (B) DH82 cells, with an intracellular distribution pattern ranging from purely membranous (A, arrow) to "membranous to cytoplasmic" (B, encircled). No significant differences in the number of cells expressing N-cadherin were detected between non-infected and persistently CDV infected DH82 cells (C). DH82Ond pi cells showed a significantly higher number of round cells expressing N-cadherin while non-infected controls displayed a significantly higher number of spindle shaped cells expressing this marker (D). Non-infected DH82 cells displayed a significantly higher expression of N-cadherin in a membranous localization while persistently CDV-infected DH82 cells showed a significantly increased "membranous to cytoplasmic" expression of this marker (E). Both non-infected (F) and DH82Ond pi cells (G) expressed vimentin (Cy2, green), with a diffuse cytoplasmic (F, encircled) to focal cytoplasmic (G, arrowhead) localization of this protein. Vimentin lacked a significant difference in the number of cells expressing the protein regardless of the infection state (H). The number of spindle-shaped cells expressing vimentin was significantly higher in non-infected DH82 cells while DH82Ond pi cells showed a significantly higher number of positive round-shaped cells (I). On the other hand, DH82Ond pi cells exhibited a significantly increased focal cytoplasmic expression while non-infected controls showed a significantly higher cytoplasmic expression of this protein (J). Bar=20µm, Box and whisker plots with median values, quartiles and maximum and minimum values. Significant differences ($p \leq 0.05$, Student´s t test) are labeled by asterisks. Graph legend: light blue = DH82 cells; yellow = DH82Ond pi cells; Diff. cytopl. = diffuse cytoplasmic; Membr. = membranous; Membr. to cyt. = membranous to cytoplasmic; Foc. cytopl. = focal cytoplasmic; MLTN + = positive multinucleated tumor cells. From Armando et al 2020.

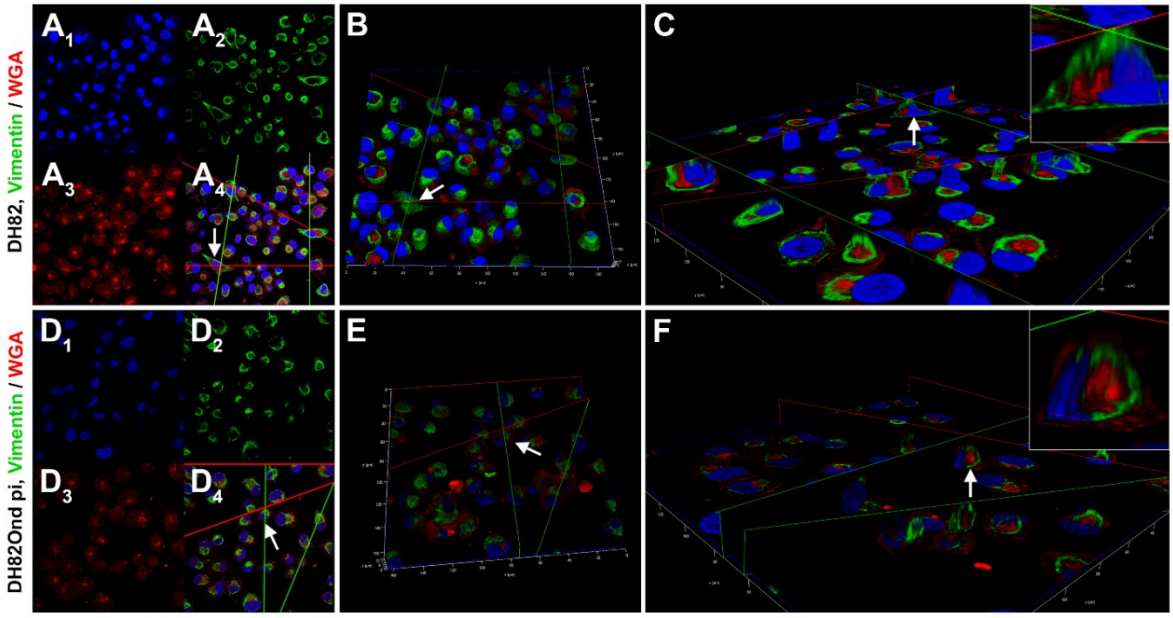

Figure 14: 3D reconstructions from double labeling immunofluorescence of non-infected DH82 (A-C) and DH82Ond pi (D-F) cells stained for vimentin and WGA. (A) 2D pictures of non-infected DH82Ond cells from z-stacks obtained with laser scanning confocal microscopy. The single channel view are: nuclei in blue, stained with bisbenzimide (A1); vimentin in green, stained with Alexa Fluor 488 (A2); and WGA in red, conjugated with Alexa Fluor 633 (A3). In addition, the picture shows a merged 3 channels view (A4). (B) Top view of the 3D reconstruction obtained from the z-stack in A, with the total cell volume represented by WGA in red. Especially within spindle-shaped cells, vimentin was diffusely detected in the cytoplasm. (C) Section-view of the 3D reconstruction in B, showing the model sectioned along the green and red planes to better display the vimentin expression (green) within the cell volume (red). Especially in the spindle-shaped cells, the protein widely occupied the cytoplasm extending up to immediately below the cell membrane (C, insert). On the contrary, within the majority of round cells the vimentin signal was detected as a focal cytoplasmic expression. Each arrow represents the same cells from the z-stack picture to the 3D section view. 3D reconstruction of non-infected DH82 double immunolabeling for vimentin / WGA was obtained by 80 z-stack frames (0.13 µm steps). (D) 2D pictures of DH82Ond pi cells from z-stacks obtained with laser scanning confocal microscopy. The single channel view are: nuclei in blue, stained with bisbenzimide (D1); vimentin in green, stained with Alexa Fluor 488 (D2); and WGA in red, conjugated with Alexa Fluor 633 (D3). In addition, the picture shows a merged 3 channels view (D4). (E) Top view of the 3D reconstruction obtained from the z-stack in D, with the total cell volume represented by WGA in red. Vimentin was expressed as a focal cytoplasmic staining (green), without extending to the cell borders. (F) Section-view of the 3D reconstruction in E, showing the model sectioned along the green and red planes to better display the vimentin expression (green) within the cell volume (red). The cut section confirmed that vimentin expression is characterized by a focal, variably sized, green signal near the nucleus and surrounding Golgi apparatus, which did not expand up to the cell membrane of the round-shaped cells (F, insert). Each arrow represents the same cells from the z-stack picture to the 3D section-view. 3D reconstruction of DH82Ond pi double immunolabeling for vimentin / WGA was obtained by 115 z-stack frames (0.13 µm steps). From Armando et al 2020.

Molecular expression of mesenchymal and epithelial markers in DH82Ond pi is suggestive of MET

Selection of gene symbols and proteins associated with EMT/MET, invasion and angiogenesis resulted in a manually generated list of 84 canine gene symbols (Supplementary Table 1). Among the selected gene symbols, 38 were differentially expressed between DH82Ond pi cells and non-infected controls. When specifically analyzed according to the functional grouping, 18 genes related to EMT/MET were down-regulated while 11 were up-regulated (Table 4). Among the epithelial markers previously investigated, only cytokeratin 8 gene symbol was up-regulated in DH82Ond pi cells. Interestingly, among the up-regulated genes also TWIST1 was included, one of the most important transcription factors involved in the activation of the EMT/MET process (89,268,269). Additionally, the gene symbol of myoferlin (MYOF), another protein associated with the expression of epithelial and mesenchymal markers(270,271) was down-regulated. This observation might further correlate with the down-regulation of fibronectin-1 (FN1). Summarized, a higher percentage of DH82Ond pi cells expressed typical epithelial markers compared to non-infected controls. Additionally, the expression of typical mesenchymal markers was maintained in both non-infected and persistently CDV-infected DH82 cells. Taken together, these results are indicative of a virus-induced mesenchymal to epithelial transition process in canine histiocytic sarcoma cells. Considered that the MET process is known to reduce the invasiveness and angiogenesis in many types of sarcomas (227), further investigations regarding gene symbols associated with invasion and angiogenesis within the microarray dataset, and functional analyses of cell motility and invasiveness were performed.

Table 4 : Manually-generated list of canine gene symbols associated with epithelial to mesenchymal/mesenchymal to epithelial transition (EMT/MET), invasion, and angiogenesis, differentially expressed in non-infected and persistently canine distemper virus infected DH82 cells. Microarray data were obtained from a previously published dataset [13,14], and were filtered according to a combination of the fold change (FC ≥ 1.5 or ≤ -1.5) and the level of significance (p≤0.05). Down-regulated genes are highlighted in green, while up-regulated genes are labeled in red.

Canine gene symbol	Gene name	Functional group	Fold change	p-value	References
TUBA4A	Tubulin, alpha 4a	Invasion and angiogenesi	-196.54	<0.001	(272)

		s			
LAMA3	Laminin α3	Invasion and angiogenesis	-52	<0.001	(124)
WLS	Wntless	EMT/MET	-51.94	<0.001	(231,273,274)
ITGA7	Integrin α7	Invasion and angiogenesis	-30.73	<0.001	(124)
CXCR4	Chemokine (C-X-C motif) receptor 4	Invasion and angiogenesis	-13.68	<0.001	(124)
LTBP1	Latent transforming growth factor beta binding protein 1	EMT/MET	-10.72	<0.001	(275)
CLTCL1	Clathrin, heavy chain-like1	EMT/MET	-8.998	<0.001	(276)
IGF2R	Insulin-like growth factor 2 receptor	Invasion and angiogenesis ; EMT/MET	-7.35	<0.001	(124,227,277)
IGFBP7	Insulin-like growth factor binding protein 7	Invasion and angiogenesis ; EMT/MET	-6.16	<0.001	(124,227,277)
BHLHE41	Basic helix loop helix e41	EMT/MET	-4.32	<0.001	(269)
RAB6B	RAB6B, member RAS oncogene family	EMT/MET	-3.57	<0.001	(278)
CAV1	Caveolin 1	EMT/MET	-3.381	<0.001	(279)
RASA1	RAS p21 protein activator (GTPase activating	EMT/MET	-3.3	<0.001	(278)

	protein) 1				
TGFB2	Transforming growth factor, beta 2	EMT/MET	-3.2	<0.001	(280)
CAV2	Caveolin 2	EMT/MET	-3.03	<0.001	(281)
FN1	Fibronectin 1	EMT/MET	-2.7	<0.001	(227)
ITGA6	Integrin α6	Invasion and angiogenesis	-2.6	<0.001	(124)
ITGB1	Integrin, beta 1	Invasion and angiogenesis ; EMT/MET	-2.54	<0.001	(124)
RAB13	RAB13, member RAS oncogene family	EMT/MET	-2.38	<0.001	(278)
LEF1	Lymphoid enhancer-binding factor 1	EMT/MET	-2.29	<0.001	(231,273,274)
FZD2	Frizzled family receptor 2	EMT/MET	-1.99	<0.001	(231,273,274)
MYOF	Myoferlin	Invasion and angiogenesis ; EMT/MET	-1.9	<0.001	(270,271,282)
FGF2	Fibroblast growth factor 2 (basic)	Invasion and angiogenesis	-1.842	0.003	(124)
LRP1	low density lipoprotein receptor-related protein 1	Invasion and angiogenesis	-1,721	0.002	(124)
AMFR	autocrine motility factor receptor, E3 ubiquitin	Invasion and angiogenesis	-1.528	0.0422	(124)

ILK	protein ligase integrin-linked kinase	Invasion and angiogenesis	-1.51	0,0257	(124)
PDGFRL	Platelet-derived growth factor receptor-like	EMT/MET	1.554	0.004	(248)
TGFBR1	Transforming growth factor, beta receptor 1	EMT/MET	1.7	<0.001	(227)
CSNK1G1	Casein kinase 1, gamma 1	EMT/MET	1.844	<0.001	(231,273,274)
GSK3B	Glycogen synthase kinase 3 beta	EMT/MET	2.44	0,0781	(231,273,274)
CD44	CD44 molecule (Indian blood group)	EMT/MET	2.65	<0.001	(227)
SENP7	SUMO/sentrin specific peptidase 7	EMT/MET	2.66	<0.001	(269)
TWIST1	Twist1	EMT/MET	3.03	<0.001	(227)
CTNND1	catenin (cadherin-associated protein), delta 1	EMT/MET	3.06	<0.001	(227)
TGFBI	Transforming growth factor, beta-induced	EMT/MET	6.46	<0.001	(227)
KRT8	Keratin 8	EMT/MET	18.38	<0.001	(227)
CDH2	Cadherin 2, type 1, N-cadherin (neuronal)	EMT/MET	77.29	<0.001	(227)

MET in DH82Ond pi cells is associated with a decreased cell motility and invasiveness

Analysis of the aforementioned microarray dataset revealed that among 19 selected genes classified within the functional group 'invasion and angiogenesis', all 13 differentially expressed gene symbols between DH82Ond pi and non-infected controls were down-regulated (Table 4). This observation is suggestive of a reduced activation of intracellular pathways associated with tumor invasion, and/or angiogenesis which might be the consequence of the activation of a MET process. To further investigate the functional relevance of the molecular and protein expression findings, a scratch and an invasion assay were performed with persistently CDV-Ond infected DH82 cells and non-infected controls. To assess cell motility, the percentage of wound closure was measured at 6 and 24 hours after scratching of a monolayer of each cell population (Figure 15). After 6 hours, no significant differences ($p = 0.1161$) were found in the percentage of wound closure in non-infected DH82 compared to DH82Ond pi cells. To assess cell invasiveness, the percentage of cell-free area was evaluated at 6, 24 and 144 hours after scratching of a monolayer of each cell population followed by covering with Matrigel matrix (Figure 16). Already after 6 hours, non-infected DH82 cells showed a tendency to move towards the periphery of the well forming cellular aggregates. On the contrary, DH82Ond pi cells maintained an arrangement in a monolayer, associated with a weak tendency to move towards the scratch. Nonetheless, no significant differences ($p = 0.7591$) were found in the percentage of cell-free area of non-infected compared to DH82Ond pi cells at this time point. After 24 hours, non-infected DH82 cells were mostly arranged in large peripheral aggregates projecting upward through the Matrigel matrix. This observation was associated with a significantly ($p < 0.0001$) higher percentage of cell-free area compared to DH82Ond pi cells, which kept their monolayer arrangement associated with a mild tendency to invade the scratch. After 144 hours, both non-infected DH82 and DH82Ond pi cells showed clear signs of cellular necrosis characterized by cell shrinkage and by the accumulation of abundant cellular debris within each well. Therefore, the evaluation of the cell- free area at this time point was excluded from the statistical analysis. These data indicated that non-infected DH82 cells have a higher migration and invasion potential as demonstrated by a faster wound closure and by the ability to migrate through the Matrigel to form aggregates. Summarized, it could be assumed that a MET induced by the CDV infection contributes to a decreased cell motility of DH82 cells in vitro.

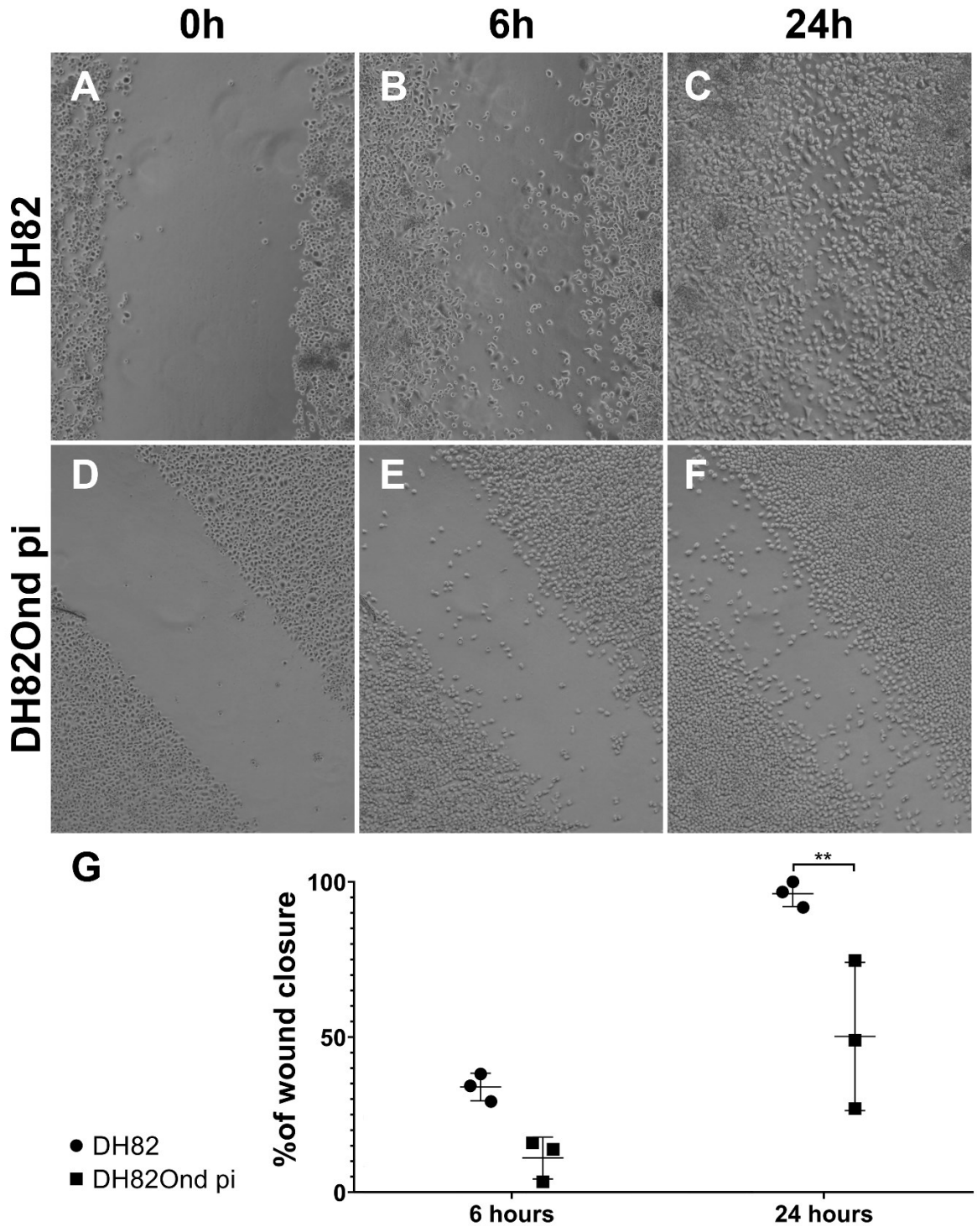

Figure 15: Representative pictures of the scratch assay at time point 0h (A, D), 6h (B, E) and 24h (C, F) in non-infected DH82 (A, B, C) and persistently CDV-infected DH82 cells (D, E, F). The percentage of closure of the scratch in non-infected DH82 (B) and DH82Ond pi (E) was not significantly different after 6h as shown in (G). The wound closure at 24h after the scratch was significantly higher in non-infected DH82 (C) compared to persistently CDV infected DH82 cells (F) as shown in (G). From Armando et al 2020.

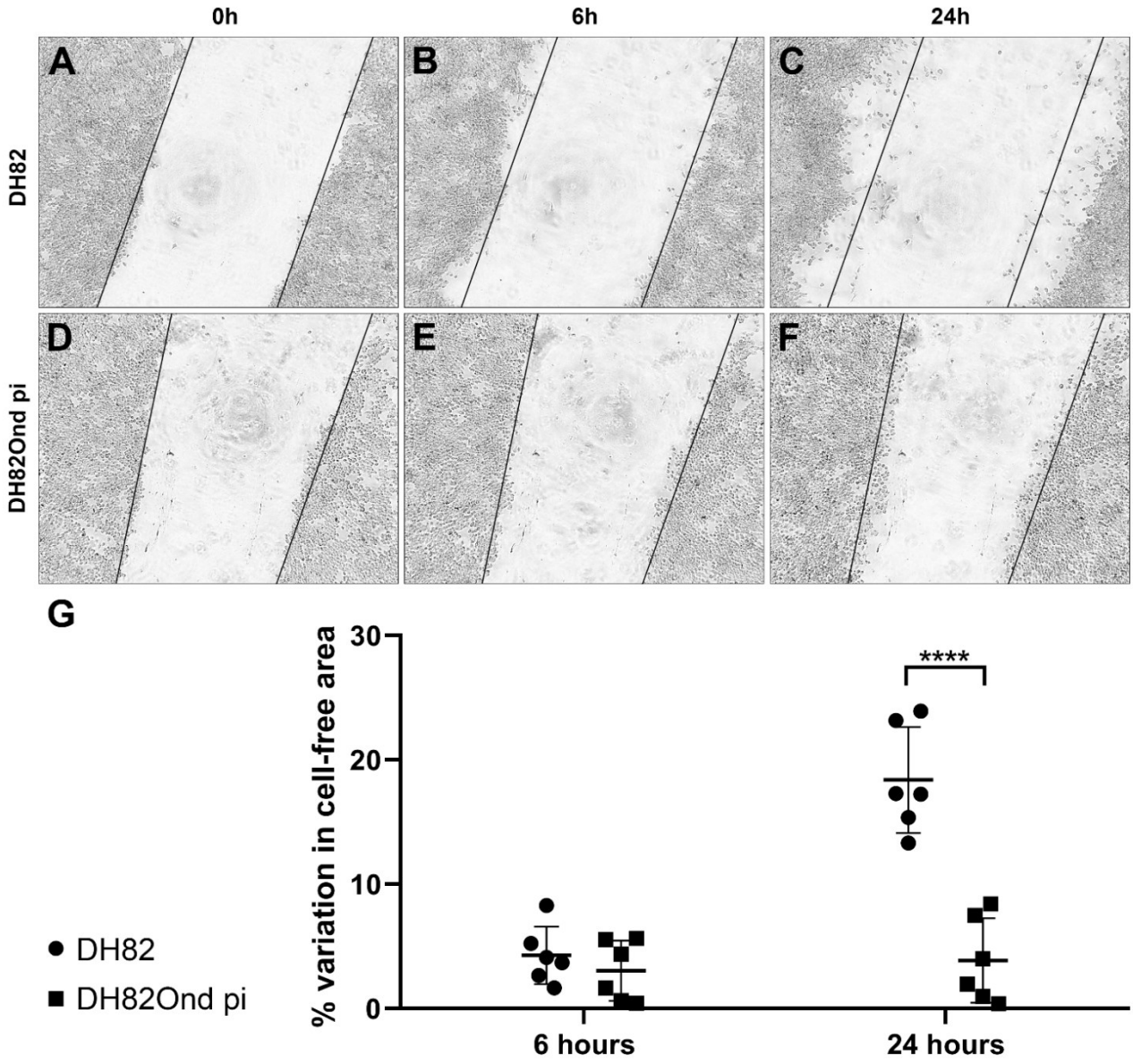

Figure 16: Representative pictures of the invasion assay at time point 0h (A, D), 6h (B, E) and 24h (C, F) in non-infected DH82 (A, B, C) and persistently CDV-infected DH82 cells (D, E, F). Non-infected DH82 cells showed a tendency to move toward the periphery of the well forming cell aggregates that projected upward through the Matrigel matrix (B, C), while DH82Ond pi cells retained a monolayered growth pattern, associated with a weak tendency to move towards the scratch. The percentage of cell-free area in non-infected DH82 (B) and DH82Ond pi (E) was not significantly different after 6h as shown in (G). on the contrary, after 24 hours a significantly higher percentage of cell-free area was observed in non-infected controls (C) compared to persistently CDV-infected DH82 cells (F) as displayed in (G), suggesting a reduced invasive potential for the latter. From Armando et al 2020.

DISCUSSION

IN VITRO STUDY 1

Canine histiocytic sarcoma cells (DH82) persistently infected with CDV-Ond display a complete spontaneous tumor regression when xenotransplanted subcutaneously into Scid mice (89). Considered that DH82Ond pi cells did not show any difference in growth and apoptotic rate compared to non-infected controls in vitro and during the initial phase after transplantation in vivo(89,91,92), it was assumed that tumor regression of DH82Ond pi xenotransplants was not caused primarily by direct virus-induced cell death alone. Indeed, it seems more likely that secondary effects of the viral infection on the tumor microenvironment (55,283), as similarly reported for Reoviruses (237), account for the complete regression. Specifically, it was estimated that regression of DH82Ond pi xenotransplants might be related to alterations in cancer-associated angiogenesis (89). Therefore, the aim of the present in vitro study was to investigate in more detail pathways potentially involved in this regression process, taking advantage of the absence of the confounding effects correlated with ongoing tumor cell death associated with acute CDV-Ond infection (90). Furthermore, to restrict the complex interactions that occur within a living organism, a less complex, highly standardized in vitro model is assumed to facilitate the analysis of specific intracellular pathways. Interestingly, the so-called “angiogenic switch” has been reported to be one of the most important hallmarks of cancer (151,284), thus playing a central role for tumor development and expansion. In this context, the present study focused on pathways correlated with increased levels of intracellular ROS. These highly reactive molecules have been reported both as fundamental intermediates in physiological intracellular signaling transduction (103,104), as well as in the regulation of different cancer hallmarks(248,255,285). Specifically, together with hypoxia, ROS represent one of the major activators of HIF-1α (124,248,253,255,285), a transcription factor involved in the regulation of a wide plethora of cancer features such as invasion, metastasis, and angiogenesis (105,248,253,254,284,285). In the context of the aforementioned considerations, the present study was further directed to investigate the impact of a persistent CDV-Ond infection of DH82 cells on cellular oxidative stress. CDV has been reported as being able to trigger an increase in ROS intracellular levels, with the subsequent induction of oxidative stress in different kinds of cells such as microglia, in vitro as well as in vivo (106–110). Similarly, the present study revealed increased ROS levels in DH82Ond pi cells, as demonstrated by an increased oxidative burst, as well as

suggested by increased gene transcription of TXNIP and NCF4. Specifically, the upregulation of both genes might correlate with an increased intracellular oxidative stress. Indeed, NCF4 encodes for p40phox, a protein that is involved in NADPH oxidase 2 activation (103,284,260). Additionally, thioredoxin-binding protein 2, encoded by the TXNIP gene, is an important inhibitor of the thioredoxin ROS scavenging system (103,261). On the other hand, ROS-induced nucleic acid damage did not differ in DH82Ond pi cells compared to non-infected controls. This observation might be interpreted as indicative of an increased oxidative stress associated with the neoplastic nature of DH82 cells rather than an effect of the viral infection. Similarly, increased intracellular ROS levels are described in the literature as a common feature of cancer cells (248,255,285). In addition, DH82Ond pi cells displayed an increased expression of SOD2 and CAT compared to non-infected controls. The overexpression of these scavenging enzymes involved in ROS detoxification have been correlated with an increased oxidative stress in neoplastic (248,255,285) as well as in inflammatory conditions (286). The results obtained by microarray analysis of genes correlated with ER stress (103,106,255,251,252) are consistent with a reduced transcription of genes correlated with this process. The data in the present study might be interpreted as suggestive of an acquired ability of DH82 cells to adapt to the persistent infection with CDV-Ond. However, a marked protein overexpression of ER-stress markers such as calnexin, calreticulin and CHOP/GADD 153 have been observed in Vero cell and primary rat neurons 36 h post-infection with recombinant A75/17-V CDV (106). On the other hand, the aforementioned lack of differences in growth and apoptotic rate between non infected and DH82Ond pi cells (91,92) is in line with the hypothesis that a persistent infection with CDV-Ond might be associated with the activation of adaptive and pro-survival pathways to contrast prolonged oxidative stress, as reported in recombinant HeLa cells expressing silkworm storage protein 1 (262). The hypothesis of the present study is further supported by the finding of an increased expression of ROS-scavenging enzymes in DH82Ond pi cells at both a molecular and protein level, highlighting the plasticity of cancer cells in actively contrasting excessively severe alterations in their redox potential (255,285). The expression of HIF-1α was subsequently investigated due to the observation that increased oxidative stress is associated with an increased HIF-1α stabilization and activation (124,248,253,255,285). Hypoxia has been widely reported as the most powerful inductor of HIF-1α transcriptional activity (124,248,253); however, in the present study, cells were cultivated under normoxic conditions. Therefore, hypoxia could be excluded as the cause of the increased HIF-1α protein expression observed in our in vitro model. Consequently, it seems more plausible that the increased expression of HIF-1α in DH82Ond pi cells was induced by the increased oxidative stress level compared to non-infected controls. The down-regulation of 2 PHDs as well as of VHL on a molecular level, in association with a lacking regulation of HIF-1α opposed

to an increased expression of the corresponding protein, could imply that the increased protein expression of HIF-1α in DH82Ond pi cells does not refer to an increased synthesis, but rather to an inhibition of the degradation pathway. Correspondingly, ROS have been reported to be directly involved in the inhibition of the aforementioned cytoplasmic enzymes (i.e., PHDs and VHL) responsible for HIF-1α hydroxylation and ubiquitination which prelude the rapid degradation of HIF-1α itself by the proteasome 26s (124,248,253). In addition to the overall increased expression of HIF-1α, the present study revealed an unusual localization of the transcription factor in the sub-membranous compartment and, to a lesser extent, within cytosolic vesicles. Further investigations aiming to better characterize the aforementioned vesicles, revealed a co-localization of HIF-1α expression with CD63, a marker for the tetraspanin-30 expressed by exosomal membranes (287). Interestingly, the presence of HIF-1α within CD63+ exosomes has previously been reported in Epstein-Barr virus-infected NP69 cells (266). On the other hand, HIF-1α only occasionally co-localized with $CD63^{+}$ exosomes, while it frequently overlapped with the localization of CDV-NP. The measles virus N-protein, which is closely related to CDV-NP (288), is transported within the cell through the endolysosomal system(267), also rendering this a possible mechanism for the canine counterpart. Furthermore, this observation displays an interesting basis for future investigations on the exact sub-cellular localization of HIF-1α within DH82Ond pi cells. Microarray data analysis aiming to investigate the molecular consequences of the unusual localization of HIF-1α and a prospective loss of function of its transcriptional activity, revealed a significant down-regulation of different genes involved in the HIF-1α angiogenic downstream pathway,which was further substantiated by a significantly reduced expression of VEGF-B on a molecular and protein level. Though VEGF-B is nowadays recognized as not being directly involved in angiogenesis, this growth factor has been reported as an indirect enhancer of VEGF-A (a well-known inducer of angiogenesis), as well as a key promoter of survival of different cell types (including endothelial cells, pericytes and smooth muscle cells) in several pathological conditions (289–291). As already reported in the literature (91), the markedly reduced expression of VEGF-B in DH82Ond pi cells did not affect cellular growth nor the apoptotic rate (92). Interestingly, DH82Ond pi cell xenotransplants displayed a significantly reduced microvessel density compared to non-infected controls (89). According to the results of the present study, it can be assumed that HIF-1α might represent an important mediator of the oncolytic effects described for the in vivo model of DH82Ond pi xenotransplants as reported previously in another viral oncolysis model (292).

IN VITRO STUDY 2

The aim of the current study was to investigate the impact of CDVOnd infection on DH82 cells, a histiocytic sarcoma cell line, on the induction of mesenchymal to epithelial transition, and if this process resulted in a decreased motility of the neoplastic cells. In the present study, as detected with immunofluorescence and confirmed by immunoblotting, E-cadherin was significantly over-expressed in DH82Ond pi cells compared to non-infected controls. This observation was further substantiated by an increased protein expression of cytokeratin 8 in DH82Ond pi compared to non-infected DH82 cells. Additionally, the expression of β-catenin was also increased in persistently CDV-infected DH82 cells, although no significant differences were noted. Taken together, these results are indicative of the occurrence of MET in DH82 cells that might be the direct consequence of the infection with CDV-Ond. In the literature, the expression of epithelial markers in several types of sarcomas has been correlated with the development of MET (225,227,234,238,293–295). This event has been associated with a better clinical outcome (220,269), suggesting an emerging role of MET in sarcomas as a potential biological and positive prognostic factor related with reduced invasiveness and metastatic rate(169). In this context, the CDV-driven MET process observed in the current study could represent a promising hint for the use of CDV-Ond as an oncolytic virus, in addition to the already reported antitumoral effects associated with the viral infection such as the alteration of MMP expression, cortactin distribution, and tumor-associated vascularization and angiogenesis (89,92,93). Despite the promising consequences of MET, the underlying mechanisms have been only marginally detailed so far (169). Nonetheless, additional molecules other than epithelial and mesenchymal markers have been correlated with MET, such as myoferlin (270). In the current study, DH82Ond pi cells showed a significant down-regulation of the myoferlin gene (MYOF) compared to non-infected DH82 cells. A depletion of this molecule in breast cancer has been associated with a reversion of the EMT process, affecting tumor invasiveness (270,271,282). Specifically, the associated increase of expression of E-cadherin and reduced levels of fibronectin and vimentin highlighted that MYOF plays an important role in EMT/MET phenomenon(270). These data are partially in line with the results obtained in the current study, in which the down-regulation of MYOF was associated simultaneously with a down-regulation of the fibronectin gene (FN1) and with an increased protein expression of E-cadherin. TWIST represents another important regulator of the MET process (169,268), which directly interacts with the expression of genes associated with the epithelial and mesenchymal phenotype. TWIST can down-regulate the E-cadherin and activate the transcription of genes such as N-cadherin and vimentin, which are associated with a mesenchymal phenotype (268). Interestingly, the mRNA data

from the current study displayed an increased expression of TWIST together with an up-regulation of N-cadherin. However, at the protein level, DH82Ond pi cells displayed an increased E-cadherin protein expression while a high expression of N-cadherin was present only at the mRNA level. This might be attributed to an incomplete MET status, in which DH82Ond pi cells might be still in a hybrid transient phase with a so-called 'metastable phenotype'(296). Similarly, the expression of both E-cadherin and N-cadherin at the protein level has been reported for circulating breast cancer cells, expressing mixed epithelial and mesenchymal characteristics in a hybrid state (197). Additionally, the discrepancies observed in the current study between the mRNA amount and the expression of the corresponding protein might be related to the intervention of miRNAs, which play a well-known role in the EMT and MET process (192), being able to directly influence the expression of E-cadherin and N-cadherin. However, the role of miRNAs in the MET process in DH82Ond pi cells should be taken in consideration for future investigations. Compared to non-infected controls, DH82Ond pi cells over-expressing E-cadherin showed more frequently an unexpected localization of this protein in a focal area of the cytoplasm around the nucleus and the Golgi apparatus, despite not reaching statistical significance. Interestingly, E-cadherin cytoplasmic internalization and other post-translational modifications of the EMT/MET effectors might be involved in the uncommon expression of this epithelial marker at the perinuclear level (268). In the current study, cytokeratin 8 also displayed a different intracellular localization depending on the cellular infection status. Notably, non-infected DH82 cells were characterized by a significantly more frequent cytoplasmic expression of cytokeratin 8, which was focally arranged around the nucleus and the Golgi apparatus, whereas DH82Ond pi cells showed a pronounced expression of variably sized aggregates of this protein within the cytoplasm and intermingled with the cell membrane. Interestingly, the MET process seems to be associated with a decreased cell motility in DH82Ond pi cells. Indeed, as already reported, a knockdown of cytokeratin 8 and 18 in neoplastic epithelial cells was associated with a significantly increased cancer cell motility and invasiveness (297). In addition, cytoplasmic expression of cytokeratin 8 is linked to a general inhibition of the migratory potential, while a perinuclear localization is related to an increased tumor cell motility (298). Similar results were obtained in the present study, which revealed an up-regulation of cytokeratin 8 within DH82Ond pi cells compared to non-infected controls The observation of cytokeratin 8 mainly in a 'membranous to cytoplasmic' localization in DH82Ond pi cells might be one factor leading to the reduced cell motility observed in the scratch and in the invasion assay. In contrast, an increased perinuclear expression of cytokeratin 8 in non-infected DH82 cells was associated with an increased cell motility in both functional assays applied. Furthermore, intermediate filaments and specifically cytokeratins are involved in cell adhesion, localization of the organelles, and changing of cellular shape (299). This might be

correlated with the more homogeneous round cellular shape of DH82Ond pi cultures compared to non-infected controls, with the latter characterized by a more pleomorphic phenotype. The hypothesis of a reduced cell motility due to a rearrangement of intermediate filaments during the MET process might be further supported by the fact that a reduced expression of vimentin is also associated with a reduced cell motility during MET (300). In the present study, a similar number of cells expressed vimentin regardless of the infection status. However, DH82Ond pi and non-infected DH82 cells showed a higher number of positive round and spindle cells, respectively. This finding was mirrored by the fact that DH82Ond pi and non-infected DH82 cells showed a more frequent focal and diffuse cytoplasmic distribution of vimentin, respectively, which was confirmed by 3D reconstructions. Taken together, these results suggest that the different intracellular distribution of vimentin between DH82Ond pi and non-infected controls might be correlated to the predominant cellular phenotype among each cell population, rather than to the infection status. Nevertheless, the predominant cellular phenotype among each cell population seems to be dependent on the infection status, thus suggesting an indirect role of the virus in the intracellular redistribution of vimentin. Interestingly, a spontaneous CDV infection of canine brain cells has also been reported to modify cytoskeletal proteins such as vimentin and glial fibrillary acid protein (GFAP) *in vivo* (301). Considered that the literature highlighted the fundamental influence of the cell shape on motility (299,302), virus-induced morphological and structural (i.e. intermediate filament rearrangement) modifications might be the cause of the observed alterations in cell motility and invasiveness.

CONCLUSIONS

Summarized, the results of the *in vitro* study 1 are indicative of a reduced activation of the HIF-1α angiogenic downstream pathway in DH82 cells persistently infected with CDV-Ond compared to non-infected controls. This is most likely due to an excessive, unusually localized, and non-functional expression of HIF-1α, which might be the consequence of a decreased cytosolic degradation of this transcriptional factor following a virus-induced increased oxidative stress. Future studies are warranted to better characterize the localization of HIF-1α and the exosomes in which it is contained, as well as to verify the presence of an increased oxidative stress and an aberrant HIF-1α localization in DH82Ond pi also in vivo. The latter approach might further substantiate the assumed correlation between reduced angiogenesis, hypoxia and tumor regression in DH82Ond pi xenotransplants.

On the other hand, the results of *in vitro* study 2 are suggestive of a MET process in DH82 cells driven by CDV infection, as shown by an increased expression of epithelial markers in DH82Ond pi cells. Additionally, CDV-driven MET seems to affect invasiveness and cell motility *in vitro*, most likely based on a rearrangement of cytoskeletal intermediate filaments. Nevertheless, future studies are warranted to detail the impact of the different factors involved in MET processes in DH82Ond pi cells. Taken together, the results obtained from the two *in vitro* studies will provide novel insights into basic mechanism mechanisms of histiocytic sarcomas biology and especially virus-induced modifications of tumor microenvironment, which might result in tumor regression. In the end these promising findings might lay down the basis for the first steps in order to establish CDV-Ond as a new potential therapeutic approach for locally aggressive histiocytic sarcomas.

APPENDIX

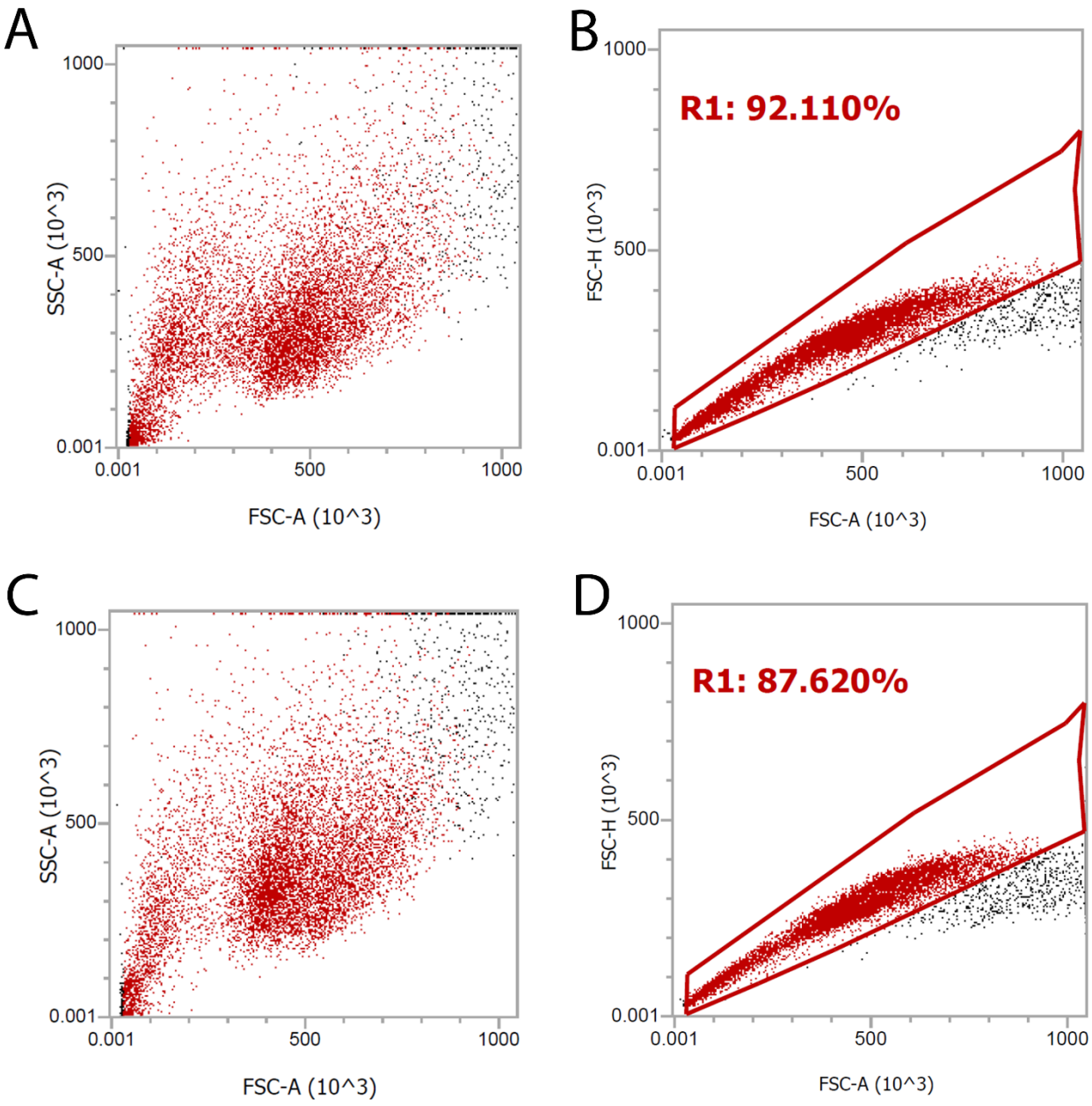

Supplementary Figure 1 Determination of oxidative burst by fluorescence activated cells sorting (FACS) in noninfected (A, B) and persistently canine distemper virus (CDV)-infected (C, D) DH82 cells. For quantification of the percentage of positive cells, doublets were excluded by FCS-A versus FSC-H gating (B, D) and only FL-1- positive cells (Gate 2) of all singlet cells (Gate 1) were quantified.

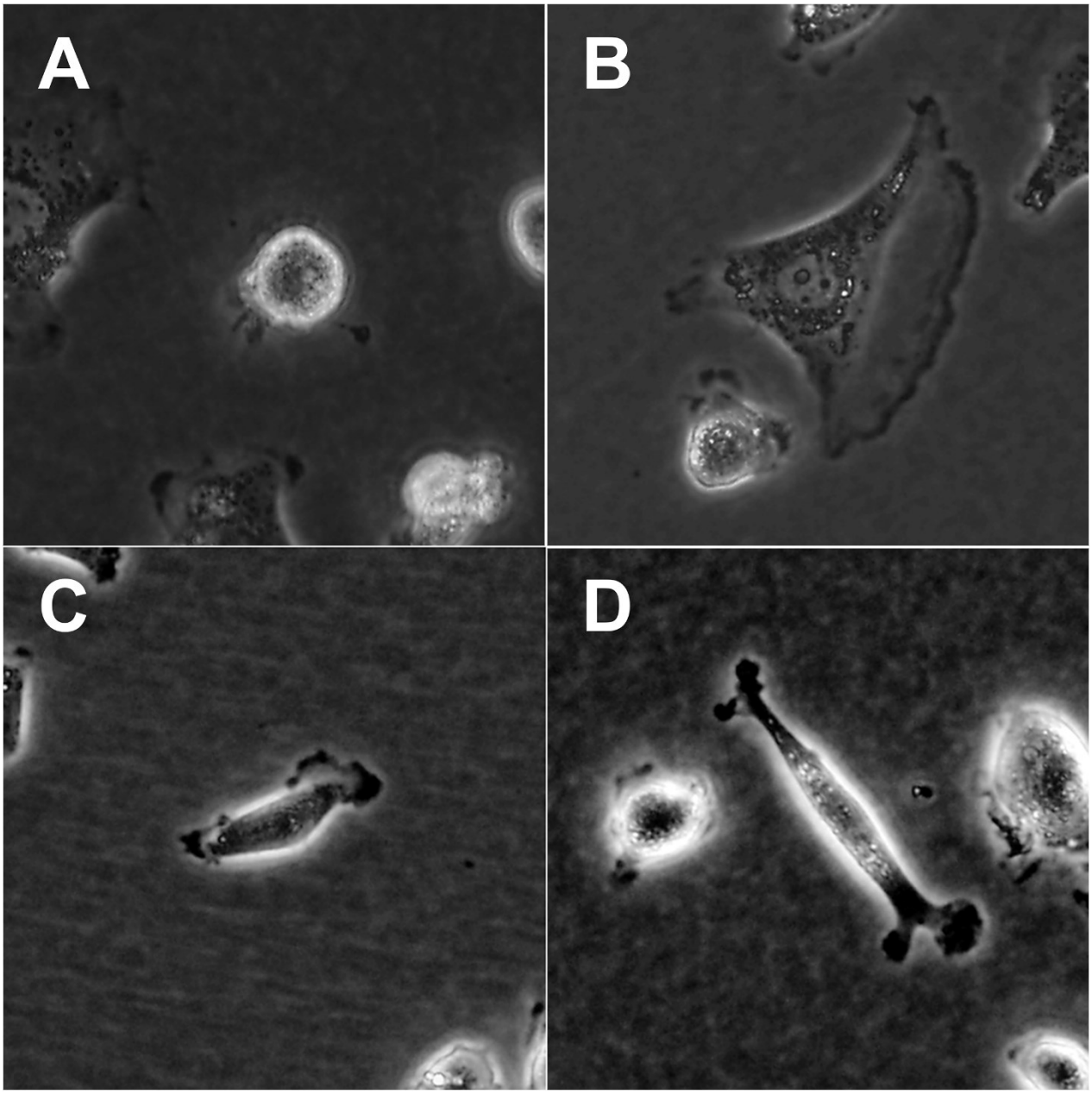

Supplemetary Figure 2: Representative pictures of the 4 different morphological phenotypes. Characteristical round (A), triangle-shaped (B), cigar-shaped (C) and slender cells (D) are shown.

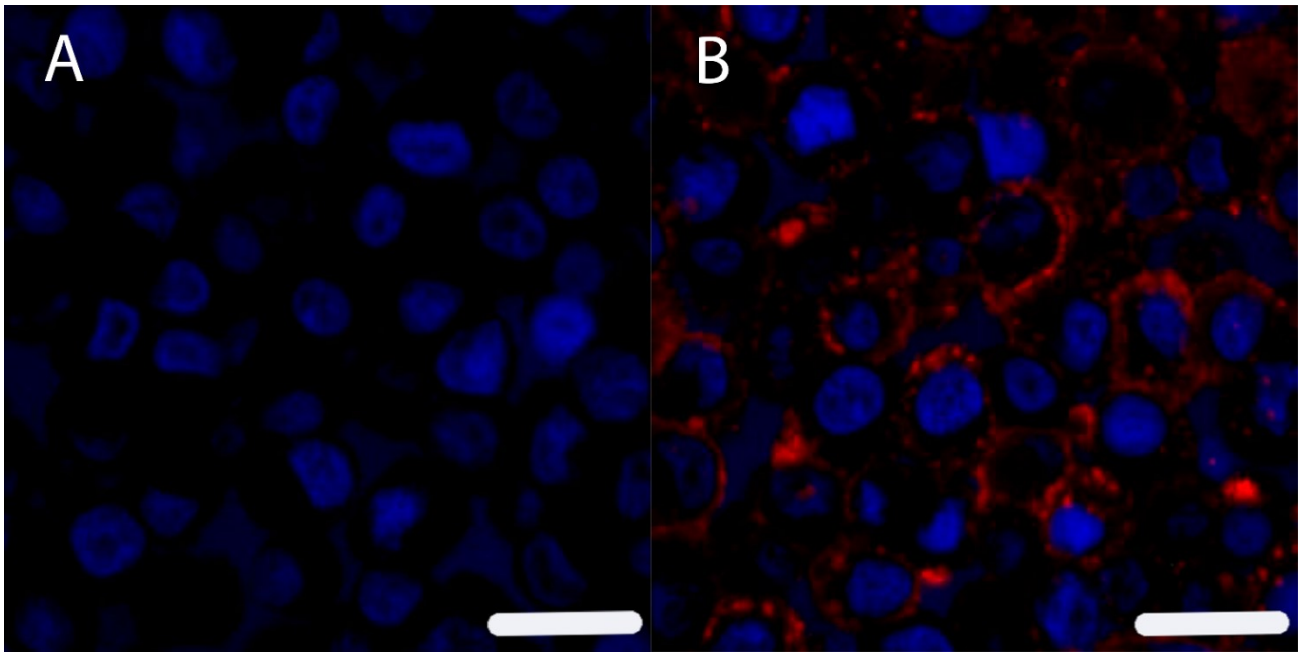

Supplementary Figure 3: Non-infected DH82 cells (A) lacked a canine distemper virus (CDV) specific signal using immunofluorescence for CDV nucleoprotein (CDV-NP, Cy3, red) whereas nearly all cells (median 99.65%, range 99.05-100.00%) express CDV-NP in persistently infected pellets (B). Nuclei were labeled with bisbenzimide (blue). Bar = 20µm

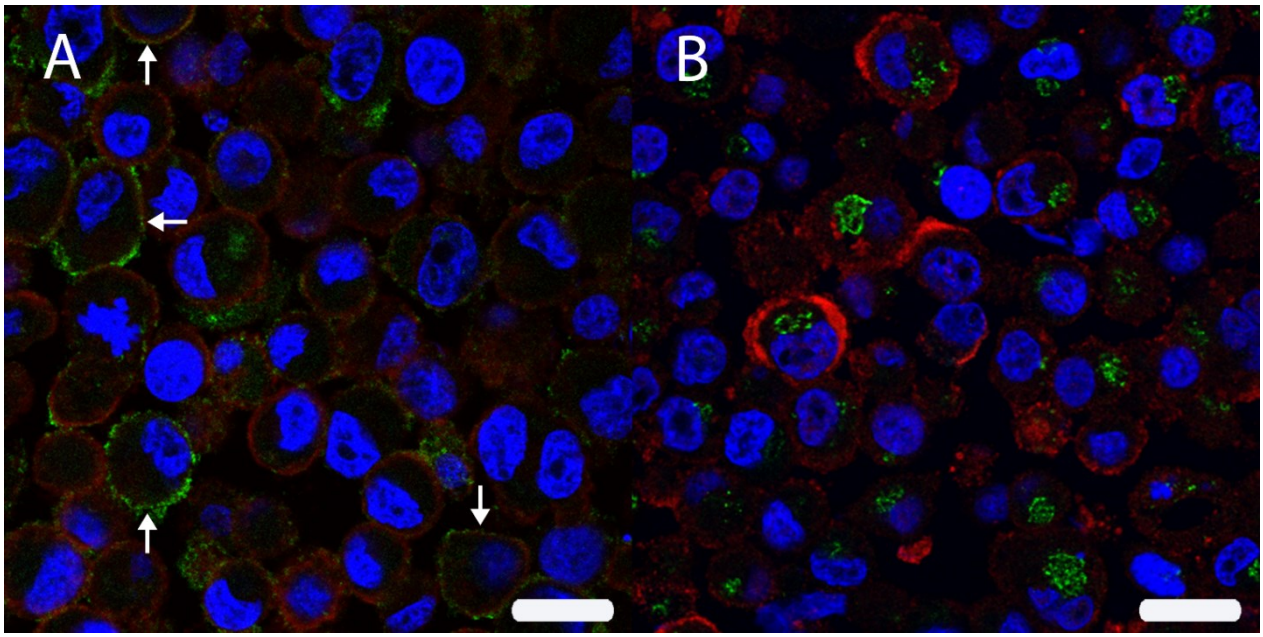

Supplementary Figure 4: (A) The intracellular localization of HIF-1α (Cy2, green) in persistently canine distemper virus (CDV)-infected DH82 cells was analyzed by double immunofluorescence with the cell membrane marker wheat germ agglutinin (WGA, Cy3, red). Furthermore a double labeling of HIF-1α (Cy3, red) and the golgi matrix protein GM-130 (Cy2, green) was performed in persistently CDV-infected DH82 cells (B). Scanning confocal laser microscopy revealed a membranous co-localization (arrows) for HIF-1α with the cell membrane (A). In contrast, no co-localization was present for HIF-1α and the golgi matrix protein GM-130, excluding the Golgi localization of the protein within the cell (B). Nuclei were stained with bisbenzimide (blue). Bar = 20µm. From Armando et al. 2020

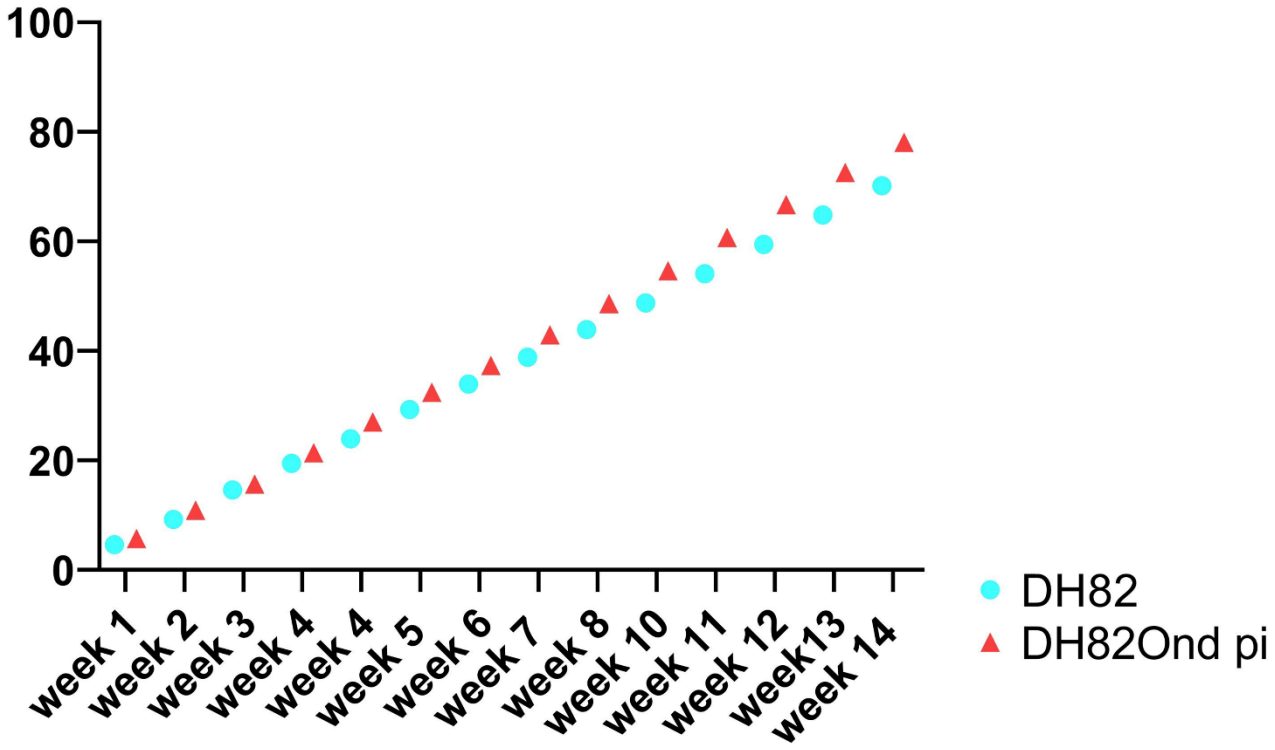

Supplementary Figure 5: Comparison of the cumulative population doubling of non-infected and persistently CDV-infected DH82 cells. The persistent infection state of CDV-Ond in DH82 cells did not influence proliferation as demonstrated by the lack of significance (p=0.6347) between the cell population doubling over 14 weeks. From Armando et al 2020.

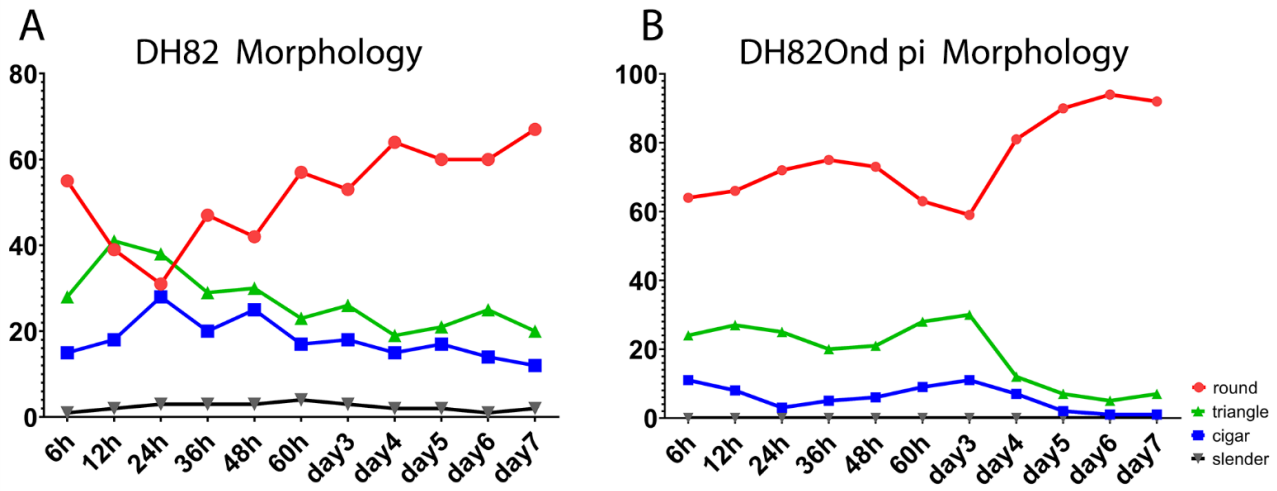

Supplementary Figure 6: Graphical outline of the morphological cellular changes in non-infected and persistently CDV-infected DH82 cells. Initially, non-infected DH82 cells (A) displayed a high percentage of round cells, which decreased during the first 24h followed by a constant increase of cells with this morphology. In contrast, DH82Ond pi cells (B) showed a constant high percentage of round cells during the first 48 h followed by a transient decrease. The percentage of triangle- and cigar-shaped cells slightly increased during the first 48 h followed by a reversion to the initial amount in non-infected (A) cells. In DH82Ond pi cells, the percentage of triangle- and cigar-shaped cells displayed a pronounced decrease starting at day 3 (B). In non-infected and DH82Ond pi cells, the percentage of cells with a slender morphology remained constant over time (A,B).

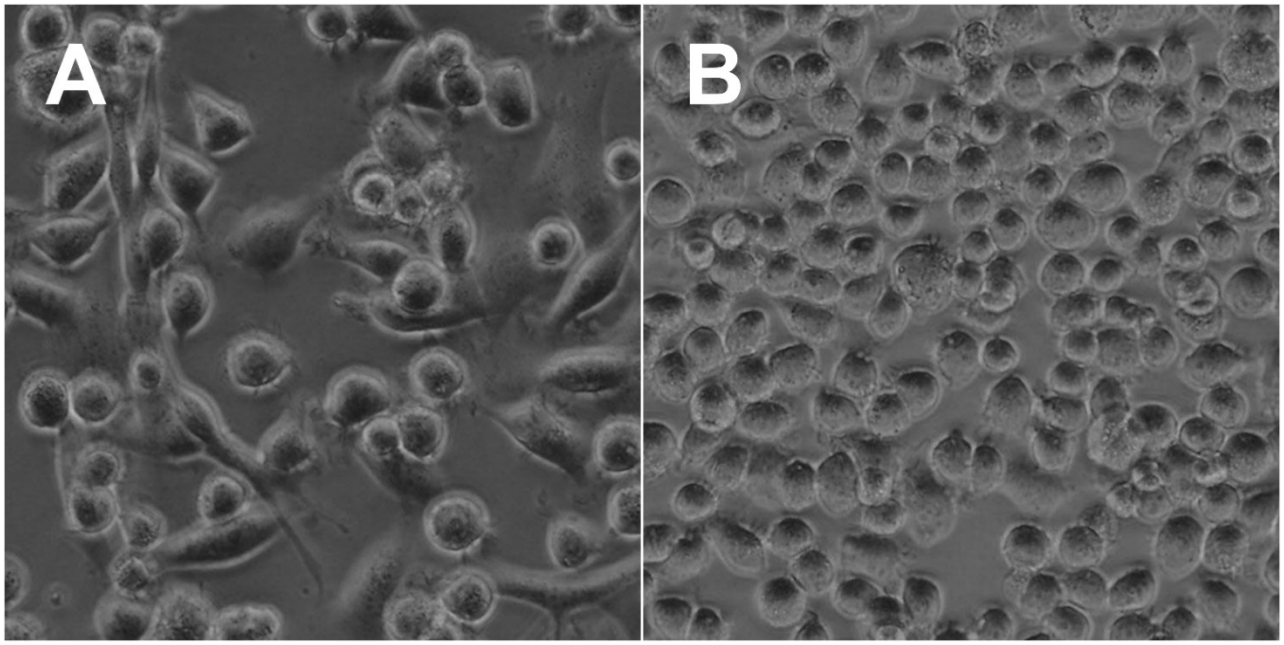

Supplementary Figure 7: Morphology of non-infected and persistently CDV-infected cell cultures. Non-infected DH82 cells (A) displayed a high pleomorphism while round cells predominated within the DH82Ond pi cell population (B).

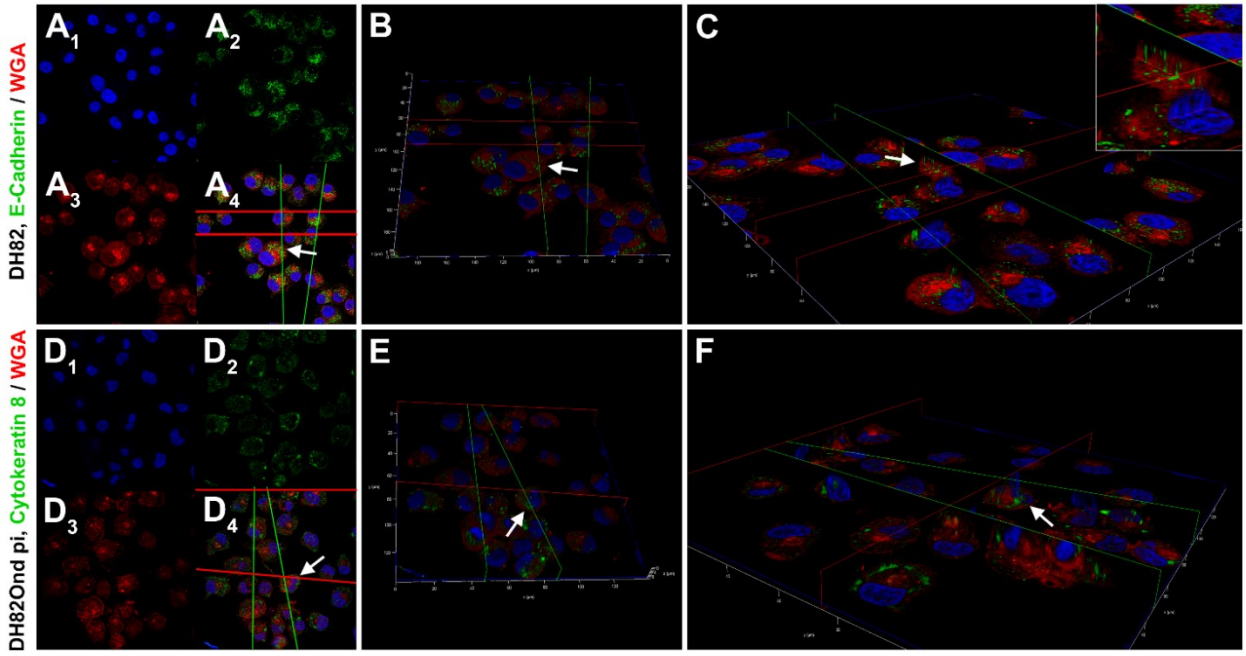

Supplementary Figure 8: 3D reconstructions from double labeling immunofluorescence of non-infected DH82 and DH82Ond pi cells stained respectively for E-cadherin / WGA (A-C) and cytokeratin 8 / WGA (D-F). (A) 2D pictures of non-infected DH82 cells from z-stacks obtained with laser scanning confocal microscopy. The single channel views are: nuclei in blue, stained with bisbenzimide (A1); E-cadherin in green, stained with Alexa Fluor 488 (A2); and WGA in red, conjugated with Alexa Fluor 633 (A3). In addition, the picture shows a merged 3 channels view (A4). (B) Top view of the 3D reconstruction obtained from the z-stack in (A), with the total cell volume represented by WGA in red. E-cadherin was characterized by a variably extended, membranous to cytoplasmic expression. (C) Section-view of the 3D reconstruction in (B), showing the model sectioned along the green and the red planes to better display the E-cadherin expression (green) within the cell volume (red). E-cadherin showed a membranous to cytoplasmic localization (C, insert), frequently intermingling with the cell membrane. Each arrow represent the same cell from the z-stack picture to the 3D section-view. 3D reconstruction of non-infected DH82 cells double immunolabeling for E-cadherin-WGA was obtained by 65 z-stack frames (0.13 µm steps). (D) 2D pictures of DH82Ond pi cells from z-stacks obtained with laser scanning confocal microscopy. The single channel views are: nuclei in blue, stained with bisbenzimide (D1); cytokeratin 8 in green, stained with Alexa Fluor 488 (D2); and WGA in red, conjugated with Alexa fluor 633 (D3). In addition, the picture shows a merged 3 channels view (D4). (E) Top view of the 3D reconstruction obtained from the z-stack in (D), with the total cell volume represented by WGA in red. Cytokeratin 8 expression was often detected on the cell surface, frequently arranging in variably sized aggregates. (F) Section-view of the 3D reconstruction in (E), showing the model sectioned along the green and the red planes to better display cytokeratin 8 expression (green) within the cell volume (red). the protein showed a membranous to cytoplasmic expression characterized by variably-sized, frequently sub-membranous immunopositive aggregates. Each arrow represents the same cell from the z-stack picture to the 3D section-view. 3D reconstruction of DH82Ond pi cells double immunolabeling for cytokeratin 8 / WGA was obtained by 82 z-stack frames (0.13 µm steps). From Armando et al 2020.

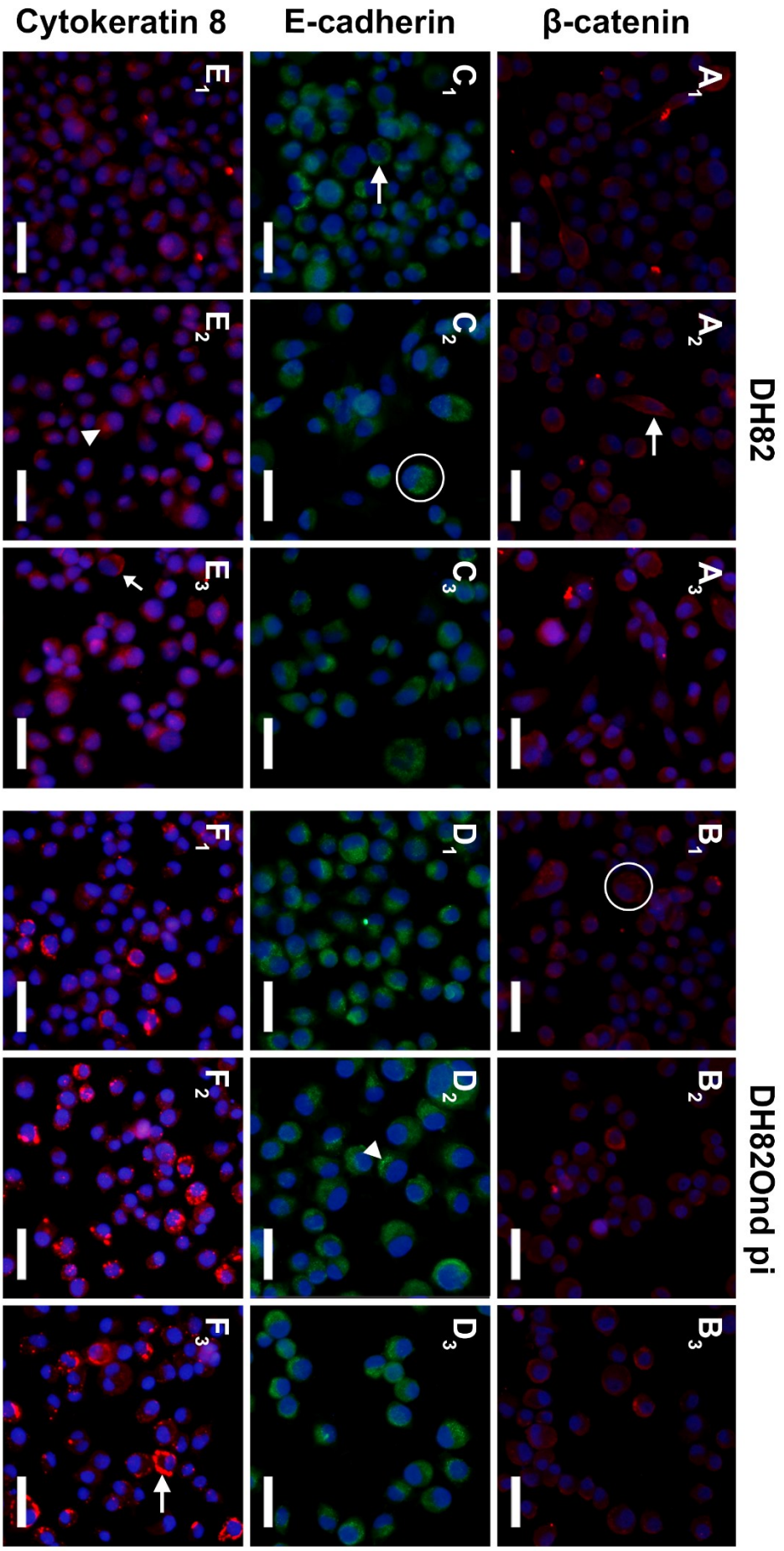
Cytokeratin 8
E-cadherin
β-catenin
DH82
DH82Ond pi
A1
A2
A3
B1
B2
B3
C1
C2
C3
D1
D2
D3
E1
E2
E3
F1
F2
F3

Supplementary Figure 9: Additional pictures of immunofluorescence for epithelial markers in non-infected (A, C, E) and persistently CDV-infected DH82 cells (B, D, F). Nuclei were labeled with bisbenzimide (blue). Staining for ß-catenin (Cy3, red) in non-infected (A1-3) and persistently CDV-infected DH82 cells (B1-3). Staining for E-cadherin (Cy2, green) in non-infected (C1-3) and persistently CDV-infected DH82 cells (D1-3). Staining for cytokeratin 8 (Cy3, red) in non-infected (E1-3) and persistently CDV-infected DH82 cells (F1-3). Non-infected DH82 (A1-3) and DH82Ond pi (B1-3) cells immunolabeled for ß-catenin showed a variable membranous to cytoplasmic (A2, arrow) and diffuse cytoplasmic (B1, encircled) protein expression. E-cadherin immunopositive cells in non-infected controls (C1-3) and DH82Ond pi (D1-3) displayed a membranous to cytoplasmic expression (C1, arrow), and a diffuse (C2, encircled) or focal (D2, arrowhead) cytoplasmic expression of this protein. Cytokeratin 8 immunostaining in non-infected DH82 cells frequently revealed a focal cytoplasmic (E2, arrowhead) expression while an only occasional membranous to cytoplasmic (E3, arrow) expression was detected (E1-3). Persistently CDV-Ond infected cells displaied a membranous to cytoplasmic expression (F3, arrow) of cytokeratin 8 (F1-3). Bar=20µm. From Armando et al 2020.

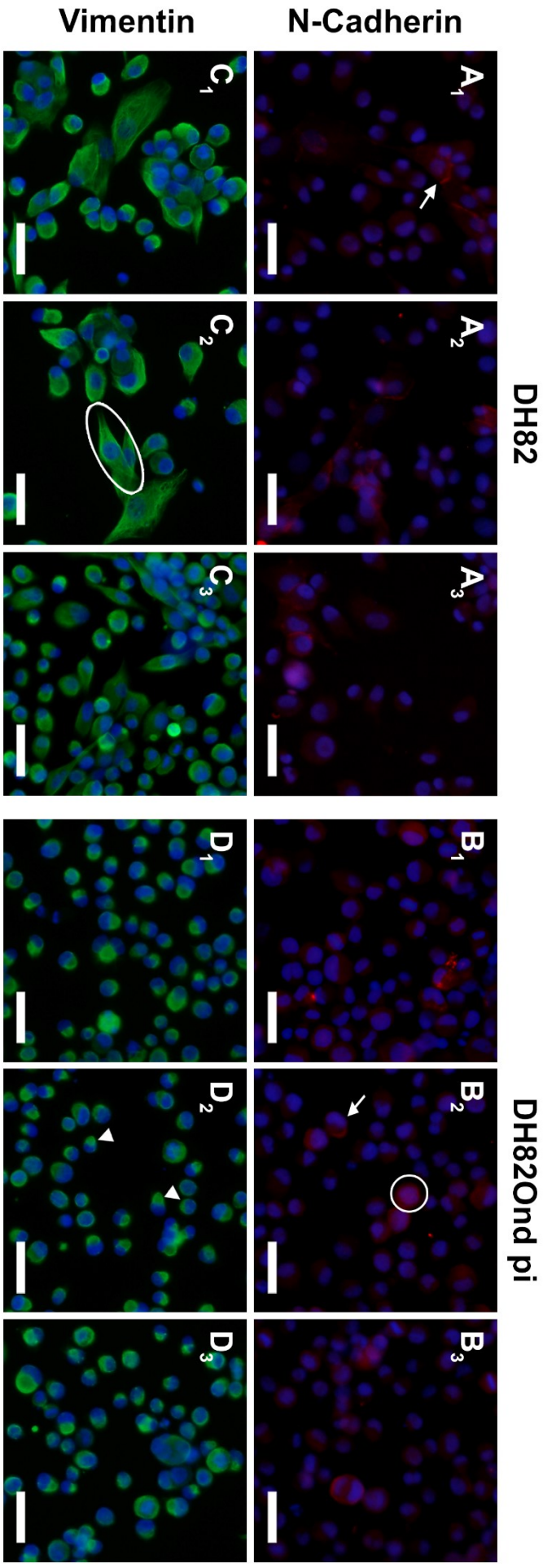
Vimentin
N-Cadherin
DH82
DH82Ond pi
A1
A2
A3
B1
B2
B3
C1
C2
C3
D1
D2
D3

Supplementary Figure 10: Additional pictures of immunofluorescence for mesenchymal markers in non-infected (A, C) and persistently CDV-infected DH82 cells (B, D). Nuclei were labeled with bisbenzimide (blue). Staining for N-cadherin (Cy3, red) in non-infected (A1-3) and persistently CDV-infected DH82 cells (B1-3). Staining for vimentin (Cy2, green) in non-infected (C1-3) and persistently CDV-infected DH82 cells (D1-3). Non-infected DH82 (A1-3) cells immunolabeled for N-cadherin showed more frequently a membranous protein expression (A1, arrow) while in DH82Ond pi cells (B1-3) the marker expression ranged from "membranous to cytoplasmic" (B2, encircled) to purely membranous (B2, arrow). Vimentin immunopositive cells in non-infected controls (C1-3) displayed a diffuse cytoplasmic expression within spindle shaped cells (C2, encircled) while DH82Ond pi (D1-3) cells often showed a focal cytoplasmic expression within round cells (D2, arrowhead). Bar=20µm. From Armando et al 2020.

SUPPLEMENTARY TABLE 1

Canine gene symbol	Fold change	p-value	Gene name	Functional group	References
TUBA4A	-196,540	<0.001	Ttubulin, alpha 4a	iInvasion and angiogenesis	Mendez, Kojima, and Goldman 2010
LAMA3	-52,000	<0.001	Laminin α3	iInvasion and angiogenesis	Lee et al. 2018
WLS	-51,940	<0.001	Wwntless	EMT/MET	Krock et al. 2011 , Das et al. 2012, Li et al. 2012
ITGA7	-30,730	<0.001	Integrin α7	iInvasion and angiogenesis	Lee et al. 2018
CXCR4	-13,485	<0,001	chemokine (C-X-C motif) receptor 4	Invasion and angiogenesis	Krock et al. 2011
LTBP1	-10,720	<0.001	Latent transforming growth factor beta binding protein 1	EMT/MET	Sun et al. 2017, Todorovic et al. 2011
CLTCL1	-8,998	<0.001	Clathrin, heavy chain-like1	EMT/MET	Todorovic et al. 2007
IGF2R	-7,350	<0.001	Insulin-like growth factor 2 receptor	Invasion and angiogenesis-;EMT/MET	Yang et al. 2014, Lee et al. 2018, Janda al. 2006

IGFBP7	-6,160	<0.001	Insulin-like growth factor binding protein 7	Invasion and angiogenesis-;EMT/MET	Yang et al. 2014, Lee et al. 2018, Janda al. 2006
BHLHE41	-4,320	<0.001	Basic helix loop helix e41	EMT/MET	Wu et al. 2019
RAB6B	-3,570	<0.001	RAB6B, member RAS oncogene family	EMT/MET	Govindarajalu et al. 2018
CAV1	-3,381	<0.001	Caveolin 1	EMT/MET	Zhang et al. 2017
RASA1	-3,300	<0.001	RAS p21 protein activator (GTPase activating protein) 1	EMT/MET	Govindarajalu et al. 2018
TGFB2	-3,200	<0.001	Transforming growth factor, beta 2	EMT/MET	Yang et al. 2014
CAV2	-3,030	<0.001	Caveolin 2	EMT/MET	Prunier and Howe 2005
FN1	-2,700	<0.001	Fibronectin 1	EMT/MET	Yang et al. 2014
ITGA6	-2,600	<0.001	Integrin α6	Iinvasion and angiogenesis	Lee et al. 2018
ITGB1	-2,540	<0.001	Integrin, beta 1	Iinvasion and angiogenesis -; EMT/MET	Lee et al. 2018
RAB13	-2,380	<0.001	RAB13, member RAS oncogene family	EMT/MET	Govindarajalu et al. 2018

LEF1	-2,290	<0.001	Lymphoid enhancer-binding factor 1	EMT/MET	Krock et al. 2011 , Das et al. 2012, Li et al. 2012
FZD2	-1,990	<0.001	Frizzled family receptor 2	EMT/MET	Krock et al. 2011 , Das et al. 2012, Li et al. 2012
MYOF	-1,900	<0.001	Myoferlin	Iinvasion and angiogenesis -; EMT/MET	Saito et al. 2006, Dong et al. 2019, Volakis et al. 2014
FGF2	-1,842	0,003	fibroblast growth factor 2 (basic)	Invasion and angiogenesis	Krock et al. 2011
LRP1	-1,721	0,002	low density lipoprotein receptor-related protein 1	Invasion and angiogenesis	Krock et al. 2011
AMFR	-1,528	0,042	autocrine motility factor receptor, E3 ubiquitin protein ligase	Invasion and angiogenesis	Krock et al. 2011
WNT7A	-1,517	0,049	wingless-type MMTV integration site family, member 7A	EMT/MET	Krock et al. 2011 , Das et al. 2012, Li et al. 2012
ILK	-1,517	0,025	integrin-linked kinase	Invasion and angiogenesis	Krock et al. 2011

PDGFRL	1,554	0,004	Platelet-derived growth factor receptor-like	EMT/MET	Dragoi et al. 2014
TGFBR1	1,700	<0.001	Ttransforming growth factor, beta receptor 1	EMT/MET	Yang et al. 2014
CSNK1G1	1,844	<0.001	Casein kinase 1, gamma 1	EMT/MET	Krock et al. 2011 , Das et al. 2012, Li et al. 2012
GSK3B	2,440	0,078	Glycogen synthase kinase 3 beta	EMT/MET	Krock et al. 2011 , Das et al. 2012, Li et al. 2012
CD44	2,650	<0.001	CD44 molecule (Indian blood group)	EMT/MET	Yang et al. 2014
SENP7	2,660	<0.001	SUMO/sentrin specific peptidase 7	EMT/MET	Lamouille and Derynck 2014
TWIST1	3,030	<0.001	Twist1	EMT/MET	Yang et al. 2014, Pfankuche, V.M., et al. 2016
CTNND1	3,060	<0,001	catenin (cadherin-associated protein), delta 1	EMT/MET	Yang et al. 2014
TGFBI	6,460	<0.001	Transforming growth factor, beta-induced	EMT/MET	Yang et al. 2014
KRT8	18,380	<0.001	Keratin 8	EMT/MET	Yang et al. 2014

CDH2	77,290	<0.001	Cadherin 2, type 1, N-cadherin (neuronal)	EMT/MET	Yang et al. 2014, Pfankuche, V.M., et al. 2016
LRP5	-1,320	0,040	low density lipoprotein receptor-related protein 5	EMT/MET	Krock et al. 2011 , Das et al. 2012, Li et al. 2012
CTNNB1	-1,293	<0,001	catenin (cadherin-associated protein), beta 1, 88kDa	EMT/MET	Yang et al. 2014
CTNNBL1	-1,242	<0,001	catenin, beta like 1	EMT/MET	Yang et al. 2014
CD34	-1,088	0,115	CD34 molecule	EMT/MET	Yang et al. 2014
GPI	-1,081	0,044	glucose-6-phosphate isomerase	Invasion and angiogenesis	Krock et al. 2011
VIM	-1,032	0,064	vimentin	EMT/MET	Yang et al. 2014
MTOR	-1,027	0,500	mechanistic target of rapamycin (serine/threonine kinase)	EMT/MET	Yang et al. 2014
CD99	-1,019	0,498	CD99 molecule	Invasion and angiogenesis	Krock et al. 2011
WNT9A	-1,001	0,296	wingless-type MMTV integration site	EMT/MET	Krock et al. 2011 , Das et al. 2012, Li et al. 2012

			family, member 9A		
WNT3	-1,001	0,343	wingless-type MMTV integration site family, member 3	EMT/MET	Krock et al. 2011 , Das et al. 2012, Li et al. 2012
SNAI2	-1,000	0,425	snail homolog 2 (Drosophila)	EMT/MET	Yang et al. 2014
KRT14	-1,000	0,419	Keratin14	Invasion and angiogenesis; EMT/MET	Krock et al. 2011, Yang et al. 2014
SMAD2 /// SMAD3	-1,000	0,364	SMAD family member 2 /// SMAD family member 3	EMT/MET	Yang et al. 2014, Wu et al. 2019
APC	1,000	1,000	adenomatous polyposis coli	EMT/MET	Krock et al. 2011 , Das et al. 2012, Li et al. 2012
CDH1	1,000	0,344	Cadherin 1, type 1, E-cadherin (epithelial)	EMT/MET	Yang et al. 2014
DES	1,000	1,000	desmin	EMT/MET	Yang et al. 2014
IGF2	1,000	1,000	insulin-like growth factor 2 (somatomedin A)	Invasion and angiogenesis	Krock et al. 2011
KRT18	1,000	1,000	Keratin18	Invasion and angiogenesis; EMT/MET	Krock et al. 2011, Yang et al. 2014

SMAD3	1,000	1,000	SMAD family member 3	EMT/MET	Yang et al. 2014, Wu et al. 2019
SNAI1	1,000	1,000	snail homolog 1 (Drosophila)	EMT/MET	Yang et al. 2014
SYP	1,000	1,000	synaptophysin	EMT/MET	Yang et al. 2014
WISP1	1,000	1,000	WNT1 inducible signaling pathway protein 1	EMT/MET	Krock et al. 2011 , Das et al. 2012, Li et al. 2012
WNT1	1,000	1,000	wingless-type MMTV integration site family, member 1	EMT/MET	Krock et al. 2011 , Das et al. 2012, Li et al. 2012
WNT10A	1,000	1,000	wingless-type MMTV integration site family, member 10A	EMT/MET	Krock et al. 2011 , Das et al. 2012, Li et al. 2012
WNT10B	1,000	1,000	wingless-type MMTV integration site family, member 10B	EMT/MET	Krock et al. 2011 , Das et al. 2012, Li et al. 2012
WNT11	1,000	1,000	wingless-type MMTV integration site family, member 11	EMT/MET	Krock et al. 2011 , Das et al. 2012, Li et al. 2012
WNT16	1,000	1,000	wingless-type MMTV integration site	EMT/MET	Krock et al. 2011 , Das et

			family, member 16		al. 2012, Li et al. 2012
WNT2	1,000	1,000	wingless-type MMTV integration site family, member 2	EMT/MET	Krock et al. 2011 , Das et al. 2012, Li et al. 2012
WNT4	1,000	1,000	wingless-type MMTV integration site family, member 4	EMT/MET	Krock et al. 2011 , Das et al. 2012, Li et al. 2012
WNT5A	1,000	1,000	wingless-type MMTV integration site family, member 5A	EMT/MET	Krock et al. 2011 , Das et al. 2012, Li et al. 2012
WNT5B	1,000	1,000	wingless-type MMTV integration site family, member 5B	EMT/MET	Krock et al. 2011 , Das et al. 2012, Li et al. 2012
WNT6	1,000	1,000	wingless-type MMTV integration site family, member 6	EMT/MET	Krock et al. 2011 , Das et al. 2012, Li et al. 2012
WNT7B	1,000	1,000	wingless-type MMTV integration site family, member 7B	EMT/MET	Krock et al. 2011 , Das et al. 2012, Li et al. 2012
WNT8A	1,000	1,000	wingless-type MMTV	EMT/MET	Krock et al. 2011 , Das et

			integration site family, member 8A		al. 2012, Li et al. 2012
WNT8B	1,000	1,000	wingless-type MMTV integration site family, member 8B	EMT/MET	Krock et al. 2011 , Das et al. 2012, Li et al. 2012
WNT9B	1,000	1,000	wingless-type MMTV integration site family, member 9B	EMT/MET	Krock et al. 2011 , Das et al. 2012, Li et al. 2012
CTNNA1	1,007	0,727	catenin (cadherin-associated protein), alpha 1, 102kDa	EMT/MET	Yang et al. 2014
AXIN1	1,009	0,25	axin 1	EMT/MET	Krock et al. 2011 , Das et al. 2012, Li et al. 2012
WIF1	1,013	0,328	WNT inhibitory factor 1	EMT/MET	Krock et al. 2011 , Das et al. 2012, Li et al. 2012
MMP2	1,028	0,342	matrix metallopeptidase 2 (gelatinase A, 72kDa gelatinase, 72kDa type IV collagenase)	Invasion and angiogenesis	Krock et al. 2011

CTNNA2	1,050	0,342	catenin (cadherin-associated protein), alpha 2	EMT/MET	Yang et al. 2014
CTNNA3	1,136	0,311	catenin (cadherin-associated protein), alpha 3	EMT/MET	Yang et al. 2014
ZEB1	1,185	0,005	zinc finger E-box binding homeobox 1	EMT/MET	Yang et al. 2014
SMAD2	1,277	<0,001	SMAD family member 2	EMT/MET	Yang et al. 2014, Wu et al. 2019
SNAI3	1,445	<0,001	snail homolog 3 (Drosophila)	EMT/MET	Yang et al. 2014
ZEB2	1,476	<0,001	zinc finger E-box binding homeobox 2	EMT/MET	Yang et al. 2014

SUPPLEMENTARY TABLE 2

Canine gene symbol	Fold change	p-value	Gene name	Functional group	References
ADM	**-1,665**	0,000	adrenomedullin	HIF-1a downstream	Krock et al. 2011
ALOX12	-1,133	0,209	arachidonate 12-lipoxygenase	ROS production	Galadari et al. 2017
ALOX12B	1,010	0,194	arachidonate 12-lipoxygenase, 12R type	ROS production	Galadari et al. 2017
ALOX15	1,000	1,000	arachidonate 15-lipoxygenase	ROS production	Galadari et al. 2017
ALOX15B	1,000	1,000	arachidonate 15-lipoxygenase, type B	ROS production	Galadari et al. 2017
ALOX5	1,000	1,000	arachidonate 5-lipoxygenase	ROS production	Galadari et al. 2017
ALOX5AP	**2,509**	0,000	arachidonate 5-lipoxygenase-activating protein	ROS production	Galadari et al. 2017
ALOXE3	-1,063	0,330	arachidonate lipoxygenase 3	ROS production	Galadari et al. 2017
ANGPT1	1,000	1,000	angiopoietin 1	HIF-1a downstream	Ushio-Fukai & Nakamura 2008; Semenza 2014; Krock et al. 2011
ANGPT2	1,026	0,342	angiopoietin 2	HIF-1a downstream	Ushio-Fukai & Nakamura 2008; Semenza

ARNT	1,014	0,276	aryl hydrocarbon receptor nuclear translocator	HIF-1a transcription&regulation	2014; Krock et al. 2011 Klaunig et al. 2010; Semenza 2014; Zepeda 2013; Krock et al. 2011
ATG5	-1,173	0,000	autophagy related 5	ER stress	Bhandary et al. 2013
BNIP3	1,000	1,000	BCL2/adenovirus E1B 19kDa interacting protein 3	ER stress	Galadari et al. 2017; Bhandary et al. 2013
BNIP3L	1,170	0,002	BCL2/adenovirus E1B 19kDa interacting protein 3-like	ER stress	Galadari et al. 2017; Bhandary et al. 2013
CALR	-1,277	0,071	calreticulin	ER stress	Brunner et al. 2012
CANX	**-2,780**	0,000	calnexin	ER stress	Brunner et al. 2012
CAT	**3,584**	0,000	Catalase	ROS scavenging	Mittal et al. 2014; Galadari et al. 2017
CCL2	**1,866**	0,000	chemokine (C-C motif) ligand 2	HIF-1a downstream	Mittal et al. 2014; 4; Krock et al. 2011
CCL28	1,000	1,000	chemokine (C-C motif) ligand 28	HIF-1a downstream	Semenza 2014
CD274	**-1,515**	0,025	CD274 molecule	HIF-1a downstream	Semenza 2014

COX1	-1,043	0,082	cytochrome c oxidase subunit I	ROS production; ER stress	Mittal et al. 2014; Galadari et al. 2017; Attig et al. 2019
COX17	**2,557**	0,001	COX17 homolog, cytochrome c oxidase assembly protein	ROS production; ER stress	Mittal et al. 2014; Galadari et al. 2017; Attig et al. 2019
COX2	-1,016	0,366	cytochrome c oxidase subunit II	ROS production; ER stress	Mittal et al. 2014; Galadari et al. 2017; Attig et al. 2019
COX3	-1,052	0,046	cytochrome c oxidase subunit III	ROS production; ER stress	Mittal et al. 2014; Galadari et al. 2017; Attig et al. 2019
COX4l1	-1,034	0,286	cytochrome c oxidase subunit IV isoform 1	ROS production; ER stress	Mittal et al. 2014; Galadari et al. 2017; Attig et al. 2019
COX4l2	-1,425	0,081	cytochrome c oxidase subunit IV isoform 2 (lung)	ROS production; ER stress	Mittal et al. 2014; Galadari et al. 2017; Attig et al. 2019
COX5A	-1,295	0,000	cytochrome c oxidase subunit Va	ROS production; ER stress	Mittal et al. 2014; Galadari et al. 2017; Attig et al. 2019

COX5B	1,074	0,046	cytochrome c oxidase polypeptide Vb	ROS production; ER stress	Mittal et al. 2014; Galadari et al. 2017; Attig et al. 2019
COX6A2	-1,026	0,342	cytochrome c oxidase subunit VIa polypeptide 2	ROS production; ER stress	Mittal et al. 2014; Galadari et al. 2017; Attig et al. 2019
COX7A1	-1,032	0,342	cytochrome c oxidase subunit VIIa polypeptide 1 (muscle)	ROS production; ER stress	Mittal et al. 2014; Galadari et al. 2017; Attig et al. 2019
COX7B2	**-6,015**	0,000	cytochrome c oxidase subunit VIIb2	ROS production; ER stress	Mittal et al. 2014; Galadari et al. 2017; Attig et al. 2019
COX8A	-1,099	0,009	cytochrome c oxidase subunit VIIIA (ubiquitous)	ROS production; ER stress	Mittal et al. 2014; Galadari et al. 2017; Attig et al. 2019
Cxcl12	**-3,683**	0,000	chemokine (C-X-C motif) ligand 12	HIF-1a downstream	Semenza 2014
CXCR4	**-13,485**	0,000	chemokine (C-X-C motif) receptor 4	HIF-1a downstream	Semenza 2014
CYBA	-1,448	0,000	cytochrome b-245, alpha polypeptide	ROS production	Mittal et al. 2014
CYBB	1,384	0,000	cytochrome b-245, beta polypeptide (chronic	ROS production	Mittal et al. 2014; Galadari et al. 2017

			granulomatous disease)		
CYCS	-1,222	0,000	cytochrome c, somatic	ROS production; ER stress	Mittal et al. 2014; Galadari et al. 2017; Bhandary et al. 2013
CYP19A1	1,005	0,342	cytochrome P450, family 17, subfamily A, polypeptide 1	ROS production; ER stress	Mittal et al. 2014; Galadari et al. 2017; Bhandary et al. 2013
CYP1A1	1,000	1,000	cytochrome P450, family 1, subfamily A, polypeptide 1	ROS production; ER stress	Mittal et al. 2014; Galadari et al. 2017; Bhandary et al. 2013
CYP1A2	1,000	1,000	cytochrome P450, family 1, subfamily A, polypeptide 2	ROS production; ER stress	Mittal et al. 2014; Galadari et al. 2017; Bhandary et al. 2013
CYP21A	1,000	1,000	cytochrome P450c21	ROS production; ER stress	Mittal et al. 2014; Galadari et al. 2017; Bhandary et al. 2013
CYP2A13	1,000	1,000	cytochrome P450 family 2 subfamily A polypeptide 13	ROS production; ER stress	Mittal et al. 2014; Galadari et al.

					2017; Bhandary et al. 2013
CYP2A25	not available in the data set	not available in the data set	not available in the data set	ROS production; ER stress	Mittal et al. 2014; Galadari et al. 2017; Bhandary et al. 2013
CYP2B6	-1,021	0,342	cytochrome P450 2B11	ROS production; ER stress	Mittal et al. 2014; Galadari et al. 2017; Bhandary et al. 2013
CYP2C21	not available in the data set	not available in the data set	not available in the data set	ROS production; ER stress	Mittal et al. 2014; Galadari et al. 2017; Bhandary et al. 2013
CYP2C41	1,000	1,000	cytochrome P450 2C41	ROS production; ER stress	Mittal et al. 2014; Galadari et al. 2017; Bhandary et al. 2013
CYP2D15	-1,000	0,431	cytochrome P450 2D	ROS production; ER stress	Mittal et al. 2014; Galadari et al. 2017; Bhandary et al. 2013

CYP2E1	1,026	0,342	cytochrome P450, family 2, subfamily E, polypeptide 1	ROS production; ER stress	Mittal et al. 2014; Galadari et al. 2017; Bhandary et al. 2013
CYP3A12 /// CYP3A4	1,000	1,000	cytochrome P-450 3A12 /// cytochrome P450, family 3, subfamily A, polypeptide 4	ROS production; ER stress	Mittal et al. 2014; Galadari et al. 2017; Bhandary et al. 2013
CYP3A12 /// CYP3A26	1,000	1,000	cytochrome P-450 3A12 /// cytochrome P450 3A26	ROS production; ER stress	Mittal et al. 2014; Galadari et al. 2017; Bhandary et al. 2013
CYP4A11	-1,001	0,345	cytochrome P450, family 4, subfamily A, polypeptide 11	ROS production; ER stress	Mittal et al. 2014; Galadari et al. 2017; Bhandary et al. 2013
CYP4A37	1,011	0,549	Cytochrome P450 4A37	ROS production; ER stress	Mittal et al. 2014; Galadari et al. 2017; Bhandary et al. 2013
CYP4A38	1,000	1,000	cytochrome P450 4A38	ROS production; ER stress	Mittal et al. 2014; Galadari et al. 2017;

CYTB	-1,292	0,000	cytochrome b	ROS production; ER stress	Bhandary et al. 2013 Attig et al. 2019
DDIT3	**-2,087**	0,000	DNA-damage-inducible transcript 3	ER stress	Brunner et al. 2012
DLL4	1,000	1,000	delta-like 4 (Drosophila)	HIF-1a downstream	Krock et al. 2011
DUOX1	1,000	1,000	dual oxidase 1	ROS production	Mittal et al. 2014; Galadari et al. 2017
DUOX2	1,000	0,400	dual oxidase 2	ROS production	Mittal et al. 2014; Galadari et al. 2017
EDN1	**-47,795**	0,000	endothelin 1	HIF-1a downstream	Krock et al. 2011
LOC100856705	1,000	1,000	ephrin-A3-like	HIF-1a downstream	Krock et al. 2011
EGFR	1,277	0,082	epidermal growth factor receptor	HIF-1a downstream	Semenza 2014
EGLN1	**-1,976**	0,001	Egl nine homolog 1 (C. elegans)	HIF-1a transcription&regulation	Klaunig et al. 2010; Semenza 214, Zepeda 2013; Krock et al. 2011
EGLN2	1,000	1,000	egl nine homolog 2 (C. elegans)	HIF-1a transcription&regulation	Klaunig et al. 2010; Semenza 214, Zepeda 2013; Krock et al. 2011

EGLN3	**-1,875**	0,004	egl nine homolog 3 (C. elegans)	HIF-1a transcription&regulation	Klaunig et al. 2010; Semenza 214, Zepeda 2013; Krock et al. 2011
ENTPD1	1,000	1,000	ectonucleoside triphosphate diphosphohydrolase 1	HIF-1a downstream	Semenza 2014
Ep300	1,000	1,000	E1A binding protein p300	HIF-1a transcription&regulation	Semenza 2014
EPAS1	-1,287	0,045	endothelial PAS domain protein 1	HIF-1a transcription&regulation	Semenza 2014; Zepeda 2013; Krock et al. 2011
EPO	1,012	0,342	erythropoietin	HIF-1a downstream	Semenza 2014
EPOR	-1,033	0,342	erythropoietin receptor	HIF-1a downstream	Semenza 2014
ERO1L	**-3,995**	0,000	ERO1-like (S. cerevisiae)	ROS production; ER stress	Bhandary et al. 2013
ERO1LB	-1,362	0,029	ERO1-like beta (S. cerevisiae)	ROS production; ER stress	Bhandary et al. 2013
FGF2	**-1,842**	0,003	fibroblast growth factor 2 (basic)	HIF-1a downstream	Krock et al. 2011
FLT1	-1,327	0,001	fms-related tyrosine kinase 1 (vascular endothelial growth factor/vascular permeability factor receptor)	HIF-1a downstream	Semenza 2014; Zepeda 2013
FLT4	-1,075	0,331	fms-related tyrosine kinase 4	HIF-1a downstream	Semenza 2014; Zepeda 2013

GCLC	1,103	0,059	glutamate-cysteine ligase, catalytic subunit	ROS scavenging; ER stress	Bhandary et al. 2013
GCLM	**-1,565**	0,000	glutamate-cysteine ligase , modifier subunit	ROS scavenging; ER stress	Bhandary et al. 2013
GPX1	1,064	0,168	glutathione peroxidase 1	ROS scavenging	Mittal et al. 2014; Galadari et al. 2017
GPX2	1,042	0,447	glutathione peroxidase 2 (gastrointestinal)	ROS scavenging	Mittal et al. 2014; Galadari et al. 2017
GPX3	1,015	0,342	glutathione peroxidase 3 (plasma)	ROS scavenging	Mittal et al. 2014; Galadari et al. 2017
Gpx4	not available in the data set	not available in the data set	not available in the data set	ROS scavenging	Mittal et al. 2014; Galadari et al. 2017
GPX5	1,000	1,000	glutathione peroxidase 5 (epididymal androgen-related protein)	ROS scavenging	Attig et al. 2019
GPX7	1,000	1,000	glutathione peroxidase 7	ROS scavenging	Attig et al. 2019
GSR	-1,375	0,000	glutathione reductase	ROS scavenging	Mittal et al. 2014; Galadari et al. 2017
GSS	**-1,648**	0,001	glutathione synthetase	ROS scavenging; ER stress	Bhandary et al. 2013

HIF1A	1,256	0,178	hypoxia inducible factor 1, alpha subunit (basic helix-loop-helix transcription factor)	HIF-1a transcription&regulation	Mittal et al. 2014; Klaunig et al. 2010; Semenza 2014; Zepeda 2013; Krock et al. 2011
HIF1AN	-1,035	0,579	hypoxia inducible factor 1, alpha subunit inhibitor	HIF-1a transcription&regulation	Semenza 2014
HMOX1	**1,940**	0,000	heme oxygenase (decycling) 1	ROS scavenging	Mittal et al. 2014
HSP90AA1	-1,260	0,000	heat shock protein 90kDa alpha (cytosolic), class A member 1	HIF-1a transcription&regulation	Zepeda 2013
IGF1R /// LOC100687483	1,129	0,218	insulin-like growth factor 1 receptor /// uncharacterized LOC100687483	HIF-1a downstream	Semenza 2014
IGF2	1,000	1,000	insulin-like growth factor 2 (somatomedin A)	HIF-1a downstream	Semenza 2014
HIF3A	-1,000	0,527	hypoxia inducible factor 3, alpha subunit	HIF-1a transcription&regulation	Zepeda 2013
ITPR1	**1,844**	0,001	inositol 1,4,5-triphosphate receptor, type 1	ER stress	Bhandary et al. 2013
ITPR2	1,062	0,729	inositol 1,4,5-trisphosphate receptor, type 2	ER stress	Bhandary et al. 2013
ITPR3	**-4,646**	0,000	inositol 1,4,5-triphosphate receptor, type 3	ER stress	Bhandary et al. 2013

KDR	1,000	0,984	kinase insert domain receptor (a type III receptor tyrosine kinase)	HIF-1a downstream	Galadari et al. 2017; Ushio-Fukai & Nakamura 2008; Semenza 2014
KIT	1,017	0,342	v-kit Hardy-Zuckerman 4 feline sarcoma viral oncogene homolog	HIF-1a downstream	Semenza 2014
KITLG	**4,174**	0,000	KIT ligand	HIF-1a downstream	Semenza 2014 Ushio-Fukai & Nakamura 2008; Krock et al. 2011
LEP	-1,013	0,231	leptin	HIF-1a downstream	
LONP1	**1,850**	0,001	lon peptidase 1, mitochondrial	ER stress	Bhandary et al. 2013
LOC100856534	1,084	0,120	lon protease homolog 2, peroxisomal-like	ER stress	Bhandary et al. 2013
MMP2	1,028	0,342	matrix metallopeptidase 2 (gelatinase A, 72kDa gelatinase, 72kDa type IV collagenase)	HIF-1a downstream	Ushio-Fukai & Nakamura 2008; Krock et al. 2011
MPO	1,000	1,000	myeloperoxidase	ROS production	Mittal et al. 2014
NCF1	1,004	0,798	neutrophil cytosolic factor 1	ROS production	Mittal et al. 2014; Ushio-Fukai & Nakamura 2008

NCF2	**1,639**	0,004	neutrophil cytosolic factor 2	ROS production	Mittal et al. 2014
NCF4	**67,304**	0,000	neutrophil cytosolic factor 4, 40kDa	ROS production	Mittal et al. 2014; Ushio-Fukai & Nakamura 2008
ND1	-1,139	0,008	NADH dehydrogenase subunit 1	ROS production; ER stress	Mittal et al. 2014; Galadari et al. 2017
ND2	-1,143	0,001	NADH dehydrogenase subunit 2	ROS production; ER stress	Mittal et al. 2014; Galadari et al. 2017
ND3	-1,179	0,001	NADH dehydrogenase subunit 3	ROS production; ER stress	Mittal et al. 2014; Galadari et al. 2017
ND4	-1,102	0,008	NADH dehydrogenase subunit 4	ROS production; ER stress	Mittal et al. 2014; Galadari et al. 2017
ND4L	-1,228	0,000	NADH dehydrogenase subunit 4L	ROS production; ER stress	Mittal et al. 2014; Galadari et al. 2017
ND5	-1,269	0,006	NADH dehydrogenase subunit 5	ROS production; ER stress	Mittal et al. 2014; Galadari et al. 2017
ND6	-1,131	0,136	NADH dehydrogenase subunit 6	ROS production; ER stress	Mittal et al. 2014; Galadari et al. 2017

NDUFA1	-1,091	0,073	NADH dehydrogenase (ubiquinone) 1 alpha subcomplex, 1, 7.5kDa	ROS production; ER stress	Mittal et al. 2014; Galadari et al. 2017
NDUFA10	**2,009**	0,000	NADH dehydrogenase (ubiquinone) 1 alpha subcomplex, 10, 42kDa	ROS production; ER stress	Mittal et al. 2014; Galadari et al. 2017
NDUFA11	1,309	0,007	NADH dehydrogenase (ubiquinone) 1 alpha subcomplex, 11, 14.7kDa	ROS production; ER stress	Mittal et al. 2014; Galadari et al. 2017
NDUFA12	1,293	0,000	NADH dehydrogenase (ubiquinone) 1 alpha subcomplex, 12	ROS production; ER stress	Mittal et al. 2014; Galadari et al. 2017
NDUFA13	1,145	0,005	NADH dehydrogenase (ubiquinone) 1 alpha subcomplex, 13	ROS production; ER stress	Mittal et al. 2014; Galadari et al. 2017
NDUFA2	-1,303	0,000	NADH dehydrogenase (ubiquinone) 1 alpha subcomplex, 2, 8kDa	ROS production; ER stress	Mittal et al. 2014; Galadari et al. 2017
LOC100855914 /// NDUFA3	-1,077	0,228	NADH dehydrogenase [ubiquinone] 1 alpha subcomplex subunit 3-like /// NADH dehydrogenase (ubiquinone) 1 alpha subcomplex, 3, 9kDa	ROS production; ER stress	Mittal et al. 2014; Galadari et al. 2017

LOC100856334	-1,038	0,072	NADH dehydrogenase [ubiquinone] 1 alpha subcomplex subunit 4-like	ROS production; ER stress	Mittal et al. 2014; Galadari et al. 2017
NDUFA4L2	1,000	1,000	NADH dehydrogenase (ubiquinone) 1 alpha subcomplex, 4-like 2	ROS production; ER stress	Mittal et al. 2014; Galadari et al. 2017
NDUFA5	1,086	0,003	NADH dehydrogenase (ubiquinone) 1 alpha subcomplex, 5, 13kDa	ROS production; ER stress	Mittal et al. 2014; Galadari et al. 2017
NDUFA6	-1,062	0,038	NADH dehydrogenase (ubiquinone) 1 alpha subcomplex, 6, 14kDa	ROS production; ER stress	Mittal et al. 2014; Galadari et al. 2017
NDUFA7	1,251	0,008	NADH dehydrogenase (ubiquinone) 1 alpha subcomplex, 7, 14.5kDa	ROS production; ER stress	Mittal et al. 2014; Galadari et al. 2017
NDUFA8	-1,157	0,007	NADH dehydrogenase (ubiquinone) 1 alpha subcomplex, 8, 19kDa	ROS production; ER stress	Mittal et al. 2014; Galadari et al. 2017
NDUFA9	-1,145	0,007	NADH dehydrogenase (ubiquinone) 1 alpha subcomplex, 9, 39kDa	ROS production; ER stress	Mittal et al. 2014; Galadari et al. 2017

NDUFAB1	**-2,261**	0,000	NADH dehydrogenase (ubiquinone) 1, alpha/beta subcomplex, 1, 8kDa	ROS production; ER stress	Mittal et al. 2014; Galadari et al. 2017
NDUFAF1	1,275	0,000	NADH dehydrogenase (ubiquinone) complex I, assembly factor 1	ROS production; ER stress	Mittal et al. 2014; Galadari et al. 2017
NDUFAF2	**-2,292**	0,000	NADH dehydrogenase (ubiquinone) 1 alpha subcomplex, assembly factor 2	ROS production; ER stress	Mittal et al. 2014; Galadari et al. 2017
NDUFB10	1,225	0,001	NADH dehydrogenase (ubiquinone) 1 beta subcomplex, 10, 22kDa	ROS production; ER stress	Mittal et al. 2014; Galadari et al. 2017
NDUFB11	-1,070	0,226	NADH dehydrogenase (ubiquinone) 1 beta subcomplex, 11, 17.3kDa	ROS production; ER stress	Mittal et al. 2014; Galadari et al. 2017
LOC100855975	1,104	0,000	NADH dehydrogenase [ubiquinone] 1 beta subcomplex subunit 3-like	ROS production; ER stress	Mittal et al. 2014; Galadari et al. 2017
NDUFB4	-1,096	0,032	NADH dehydrogenase (ubiquinone) 1 beta subcomplex, 4, 15kDa	ROS production; ER stress	Mittal et al. 2014; Galadari et al. 2017

NDUFB5	1,167	0,031	NADH dehydrogenase (ubiquinone) 1 beta subcomplex, 5, 16kDa	ROS production; ER stress	Mittal et al. 2014; Galadari et al. 2017
NDUFB6	-1,116	0,010	NADH dehydrogenase (ubiquinone) 1 beta subcomplex, 6, 17kDa	ROS production; ER stress	Mittal et al. 2014; Galadari et al. 2017
NDUFB7	1,273	0,012	NADH dehydrogenase (ubiquinone) 1 beta subcomplex, 7, 18kDa	ROS production; ER stress	Mittal et al. 2014; Galadari et al. 2017
NDUFB8	-1,210	0,000	NADH dehydrogenase (ubiquinone) 1 beta subcomplex, 8, 19kDa	ROS production; ER stress	Mittal et al. 2014; Galadari et al. 2017
NDUFB9	-1,370	0,000	NADH dehydrogenase (ubiquinone) 1 beta subcomplex, 9, 22kDa	ROS production; ER stress	Mittal et al. 2014; Galadari et al. 2017
NDUFC1	-1,449	0,000	NADH dehydrogenase (ubiquinone) 1, subcomplex unknown, 1, 6kDa	ROS production; ER stress	Mittal et al. 2014; Galadari et al. 2017
NDUFC2	**-1,630**	0,001	NADH dehydrogenase (ubiquinone) 1, subcomplex unknown, 2, 14.5kDa	ROS production; ER stress	Mittal et al. 2014; Galadari et al. 2017

NDUFS1	**1,622**	0,000	NADH dehydrogenase (ubiquinone) Fe-S protein 1, 75kDa (NADH-coenzyme Q reductase)	ROS production; ER stress	Mittal et al. 2014; Galadari et al. 2017
NDUFS2	1,296	0,000	NADH dehydrogenase (ubiquinone) Fe-S protein 2, 49kDa (NADH-coenzyme Q reductase)	ROS production; ER stress	Mittal et al. 2014; Galadari et al. 2017
NDUFS3	1,124	0,068	NADH dehydrogenase (ubiquinone) Fe-S protein 3, 30kDa (NADH-coenzyme Q reductase)	ROS production; ER stress	Mittal et al. 2014; Galadari et al. 2017
NDUFS4	-1,074	0,023	NADH dehydrogenase (ubiquinone) Fe-S protein 4, 18kDa (NADH-coenzyme Q reductase)	ROS production; ER stress	Mittal et al. 2014; Galadari et al. 2017
NDUFS5	1,283	0,000	NADH dehydrogenase (ubiquinone) Fe-S protein 5, 15kDa (NADH-coenzyme Q reductase)	ROS production; ER stress	Mittal et al. 2014; Galadari et al. 2017
NDUFS6	1,494	0,000	NADH dehydrogenase (ubiquinone) Fe-S protein 6, 13kDa	ROS production; ER stress	Mittal et al. 2014; Galadari et al. 2017

			(NADH-coenzyme Q reductase)		
NDUFS7	**1,846**	0,000	NADH dehydrogenase (ubiquinone) Fe-S protein 7, 20kDa (NADH-coenzyme Q reductase)	ROS production; ER stress	Mittal et al. 2014; Galadari et al. 2017
NDUFS8	-1,266	0,005	NADH dehydrogenase (ubiquinone) Fe-S protein 8, 23kDa (NADH-coenzyme Q reductase)	ROS production; ER stress	Mittal et al. 2014; Galadari et al. 2017
NDUFV1	-1,290	0,000	NADH dehydrogenase (ubiquinone) flavoprotein 1, 51kDa	ROS production; ER stress	Mittal et al. 2014; Galadari et al. 2017
NDUFV2	1,242	0,000	NADH dehydrogenase (ubiquinone) flavoprotein 2, 24kDa	ROS production; ER stress	Mittal et al. 2014; Galadari et al. 2017
NDUFV3	**2,362**	0,000	NADH dehydrogenase (ubiquinone) flavoprotein 3	ROS production; ER stress	Mittal et al. 2014; Galadari et al. 2017
NOS1	-1,001	0,347	nitric oxide synthase 1 (neuronal)	ROS production; ER stress	Bhandary et al. 2013
NOS2	1,000	1,000	nitric oxide synthase 2, inducible	ROS production; ER stress	Bhandary et al. 2013
NOS3	1,000	1,000	nitric oxide synthase 3 (endothelial cell)	ROS production	Mittal et al. 2014
NOX1	1,000	1,000	NADPH oxidase 1	ROS production	Mittal et al. 2014;

NOX3	-1,013	0,342	NADPH oxidase 3	ROS production	Galadari et al. 2017 Mittal et al. 2014; Galadari et al. 2017
NOX4	-1,007	0,243	NADPH oxidase 4	ROS production; ER stress	Mittal et al. 2014; Galadari et al. 2017; Bhandary et al. 2013
NOX5	1,000	1,000	NADPH oxidase, EF-hand calcium binding domain 5	ROS production	Mittal et al. 2014; Galadari et al. 2017
NOXA1	1,052	0,342	NADPH oxidase activator 1	ROS production	Mittal et al. 2014
NOXO1	-1,005	0,344	NADPH oxidase organizer 1	ROS production	Mittal et al. 2014
NQO1	**3,868**	0,000	NAD(P)H dehydrogenase, quinone 1	ROS scavenging	Mittal et al. 2014
NT5E	**-3,041**	0,000	5'-nucleotidase, ecto (CD73)	HIF-1a downstream	Semenza 2014
KAT2B	-1,002	0,975	K(lysine) acetyltransferase 2B	HIF-1a transcription&regulation	Krock et al. 2011
PDGFA	**2,089**	0,000	platelet-derived growth factor alpha polypeptide	HIF-1a downstream	Semenza 2014
PDGFB	1,009	0,501	platelet-derived growth factor beta polypeptide	HIF-1a downstream	Semenza 2014
PDGFC	**6,578**	0,000	platelet derived growth factor C	HIF-1a downstream	Semenza 2014

PDGFD	1,000	1,000	platelet derived growth factor D	HIF-1a downstream	Semenza 2014
PDGFRA	-1,018	0,658	platelet-derived growth factor receptor, alpha polypeptide	HIF-1a downstream	Semenza 2014
PDGFRB	1,000	1,000	platelet-derived growth factor receptor, beta polypeptide	HIF-1a downstream	Semenza 2014
PDGFRL	**1,554**	0,004	platelet-derived growth factor receptor-like	HIF-1a downstream	Semenza 2014
PDIA3	**-1,533**	0,001	protein disulfide isomerase family A, member 3	ROS production; ER stress	Bhandary et al. 2013
PDIA4	**-1,678**	0,010	protein disulfide isomerase family A, member 4	ROS production; ER stress	Bhandary et al. 2013
PDIA5	-1,294	0,005	protein disulfide isomerase family A, member 5	ROS production; ER stress	Bhandary et al. 2013
PDIA6	**-1,801**	0,000	protein disulfide isomerase family A, member 6	ROS production; ER stress	Bhandary et al. 2013
LOC100855780	1,000	1,000	placenta growth factor-like	HIF-1a downstream	Semenza 2014; Zepeda 2013
PPID	**2,286**	0,000	peptidylprolyl isomerase D (cyclophilin D)	ER stress	Mittal et al. 2014; Galadari et al. 2017
PRDX1	1,158	0,000	peroxiredoxin 1	ROS scavenging	Mittal et al. 2014;

					Galadari et al. 2017
LOC100856470	**5,351**	0,000	peroxiredoxin-2-like	ROS scavenging	Mittal et al. 2014; Galadari et al. 2017
PRDX3	1,019	0,422	peroxiredoxin 3	ROS scavenging	Mittal et al. 2014; Galadari et al. 2017
LOC100856588	-1,413	0,000	peroxiredoxin-4-like	ROS scavenging; ER stress	Mittal et al. 2014; Galadari et al. 2017; Bhandary et al. 2013
PLCB3 /// PRDX5	-1,405	0,001	phospholipase C, beta 3 (phosphatidylinositol-specific) /// peroxiredoxin 5	ROS scavenging	Mittal et al. 2014; Galadari et al. 2017
PRDX6	**-1,895**	0,000	peroxiredoxin 6	ROS scavenging	Mittal et al. 2014; Galadari et al. 2017
PTGS2	-1,235	0,129	prostaglandin-endoperoxide synthase 2 (prostaglandin G/H synthase and cyclooxygenase)	HIF-1a downstream	Ushio-Fukai & Nakamura 2008; Krock et al. 2011
RAC2	-1,156	0,073	ras-related C3 botulinum toxin substrate 2 (rho	ROS production	Attig et al. 2019

			family, small GTP binding protein Rac2) guanine nucleotide binding protein (G protein), beta polypeptide 2-like 1		
GNB2L1	1,052	0,098		HIF-1a transcription&regulation	Zepeda 2013
RHOA	1,453	0,000	ras homolog family member A	ROS production; ER stress	Mittal et al. 2014; Bhandary et al. 2013
RYR1	not available in the data set	not available in the data set	not available in the data set	ER stress	Bhandary et al. 2013
RYR2	-1,027	0,342	Ryanodine receptor 2 (cardiac)	ER stress	Bhandary et al. 2013
RYR3	-1,478	0,015	ryanodine receptor 3	ER stress	Bhandary et al. 2013
SDHC	1,211	0,004	succinate dehydrogenase complex, subunit C, integral membrane protein, 15kDa	ROS production; ER stress	Mittal et al. 2014; Galadari et al. 2017
SDHD	**-1,857**	0,000	succinate dehydrogenase complex, subunit D, integral membrane protein	ROS production; ER stress	Mittal et al. 2014; Galadari et al. 2017
SEMA4D	1,000	1,000	sema domain, immunoglobulin domain (Ig), transmembrane domain (TM) and short cytoplasmic	HIF-1a downstream	Krock et al. 2011

			domain, (semaphorin) 4D		
SERPINE1	**-13,116**	0,000	serine (or cysteine) peptidase inhibitor, clade E, member 1	HIF-1a downstream	Ushio-Fukai & Nakamura 2008; Krock et al. 2011
SIRT1	1,217	0,024	sirtuin 1	HIF-1a transcription&regulation	Krock et al. 2011
SLC25A31	1,000	1,000	solute carrier family 25 (mitochondrial carrier; adenine nucleotide translocator), member 31	ER stress	Mittal et al. 2014; Galadari et al. 2017
SLC25A4	1,386	0,002	solute carrier family 25 (mitochondrial carrier; adenine nucleotide translocator), member 4	ER stress	Mittal et al. 2014; Galadari et al. 2017
SLC25A5	-1,027	0,295	solute carrier family 25 (mitochondrial carrier; adenine nucleotide translocator), member 5	ER stress	Mittal et al. 2014; Galadari et al. 2017
SLC25A6	-1,135	0,014	solute carrier family 25 (mitochondrial carrier; adenine nucleotide translocator), member 6	ER stress	Mittal et al. 2014; Galadari et al. 2017
SOD1	**-1,712**	0,000	superoxide dismutase 1, soluble	ROS scavenging	Mittal et al. 2014;

					Galadari et al. 2017
SOD2	-1,422	0,019	superoxide dismutase 2, mitochondrial	ROS scavenging	Mittal et al. 2014; Galadari et al. 2017
SOD3	1,000	1,000	superoxide dismutase 3, extracellular	ROS scavenging	Mittal et al. 2014; Galadari et al. 2017
SUMO1	1,336	0,000	SMT3 suppressor of mif two 3 homolog 1 (S. cerevisiae)	HIF-1a transcription&regulation	Ushio-Fukai & Nakamura 2008; Krock et al. 2011
TEK	**5,639**	0,000	endothelial-specific receptor tyrosine kinase	HIF-1a downstream	Ushio-Fukai & Nakamura 2008; Semenza 2014; Krock et al. 2011
Tgfa	-1,021	0,096	transforming growth factor, alpha	HIF-1a downstream	Semenza 2014
THBS1	**-4,461**	0,000	thrombospondin 1	HIF-1a downstream	Krock et al. 2011
THBS2	**-451,295**	0,000	thrombospondin 2	HIF-1a downstream	Krock et al. 2011
TIE1	1,000	0,352	tyrosine kinase with immunoglobulin-like and EGF-like domains 1	HIF-1a downstream	Ushio-Fukai & Nakamura 2008; Semenza 2014; Krock et al. 2011
TRPC1	-1,062	0,269	transient receptor potential cation	ER stress	Mittal et al. 2014

TRPC3	-1,004	0,342	channel, subfamily C, member 1 transient receptor potential cation channel, subfamily C, member 3	ER stress	Mittal et al. 2014
TRPC4	-1,014	0,194	transient receptor potential cation channel, subfamily C, member 4	ER stress	Mitttal 2014
TRPC6	1,000	1,000	transient receptor potential cation channel, subfamily C, member 6	ER stress	Mittal et al. 2014
TXN2	1,165	0,022	thioredoxin 2	ROS scavenging	Mittal et al. 2014; Galadari et al. 2017
TXNIP	**11,227**	0,001	thioredoxin interacting protein	ROS scavenging	Mittal et al. 2014
TXNL1	-1,067	0,020	thioredoxin-like 1	ROS scavenging	Mittal et al. 2014; Galadari et al. 2017; Ushio-Fukai & Nakamura 2008
TXNL4B	-1,205	0,162	thioredoxin-like 4B	ROS scavenging	Mittal et al. 2014; Galadari et al. 2017; Ushio-Fukai & Nakamura 2008

TXNRD1	-1,303	0,081	thioredoxin reductase 1	ROS scavenging	Mittal et al. 2014; Galadari et al. 2017
TXNRD2	1,180	0,443	thioredoxin reductase 2	ROS scavenging	Mittal et al. 2014; Galadari et al. 2017
TXNRD3	**-2,464**	0,000	thioredoxin reductase 3	ROS scavenging	Mittal et al. 2014; Galadari et al. 2017
UQCC	-1,303	0,001	ubiquinol-cytochrome c reductase complex chaperone	ROS production; ER stress	Mittal et al. 2014; Galadari et al. 2017
UQCR11	**1,563**	0,002	ubiquinol-cytochrome c reductase (6.4kD) subunit	ROS production; ER stress	Mittal et al. 2014; Galadari et al. 2017
LOC477944	-1,110	0,015	cytochrome b-c1 complex subunit 7-like	ROS production; ER stress	Mittal et al. 2014; Galadari et al. 2017
UQCRC1	**1,678**	0,000	ubiquinol-cytochrome c reductase core protein 1	ROS production; ER stress	Mittal et al. 2014; Galadari et al. 2017
UQCRC2	**1,590**	0,021	ubiquinol cytochrome c reductase core protein 2	ROS production; ER stress	Mittal et al. 2014; Galadari et al. 2017
UQCRFS1	-1,034	0,315	ubiquinol-cytochrome c reductase, Rieske	ROS production; ER stress	Mittal et al. 2014;

			iron-sulfur polypeptide 1		Galadari et al. 2017
UQCRH	1,392	0,000	ubiquinol-cytochrome c reductase hinge protein	ROS production; ER stress	Mittal et al. 2014; Galadari et al. 2017
UQCRQ	-1,181	0,003	ubiquinol-cytochrome c reductase, complex III subunit VII, 9.5kDa	ROS production; ER stress	Mittal et al. 2014; Galadari et al. 2017
VDAC1	1,084	0,001	voltage-dependent anion channel 1	ER stress	Mittal et al. 2014; Galadari et al. 2017
VDAC2	-1,149	0,000	voltage-dependent anion channel 2	ER stress	Mittal et al. 2014; Galadari et al. 2017
VDAC3	1,049	0,029	voltage-dependent anion channel 3	ER stress	Mittal et al. 2014; Galadari et al. 2017
VEGFA	-1,666	0,169	vascular endothelial growth factor A	HIF-1a downstream	Mittal et al. 2014; Galadari et al. 2017; Ushio-Fukai & Nakamura 2008; Semenza 2014; Zepeda 2013
VEGFB	**-593,197**	0,000	vascular endothelial growth factor B	HIF-1a downstream	Mittal et al. 2014; Galadari et al.

					2017; Ushio-Fukai & Nakamura 2008; Semenza 2014; Zepeda 2013
VEGFC	-1,097	0,088	vascular endothelial growth factor C	HIF-1a downstream	Mittal et al. 2014; Galadari et al. 2017; Ushio-Fukai & Nakamura 2008; Semenza 2014; Zepeda 2013
VEGFD	not available in the data set	not available in the data set	not available in the data set	HIF-1a downstream	Mittal et al. 2014; Galadari et al. 2017; Ushio-Fukai & Nakamura 2008; Semenza 2014; Zepeda 2013
VHL	**-1,771**	0,005	von Hippel-Lindau tumor suppressor, E3 ubiquitin protein ligase	HIF-1a transcription&regulation	Galadari et al. 2017; Klaunig et al. 2010; Semenza 214, Zepeda 2013; Krock et al. 2011

XDH	**3,913**	0,002	xanthine dehydrogenase	ROS production; ER stress	Mittal et al. 2014; Galadari et al. 2017; Bhandary et al. 2013

List of papers published during the PhD in Medical-Veterinary Science

1. Maria A. Ernandes, Anna M. Cantoni, **Federico Armando**, Attilio Corradi, Lorenzo Ressel, Alice Tamborini. "*Feline coronavirus-associated myocarditis in a domestic longhair cat*", Journal of Feline Medicine and Surgery Open Reports, 1–5, 2019

2. **Federico Armando***, Matteo Gambini*, Attilio Corradi, Chiara Giudice, Vanessa M. Pfankuche, Graham Brogden, Friederike Attig, Maren von Köckritz-Blickwede, Wolfgang Baumgärtner, Christina Puff. "*Oxidative Stress in Canine Histiocytic Sarcoma Cells Induced by an Infection with Canine Distemper Virus Led to a Dysregulation of HIF-1α Downstream Pathway Resulting in a Reduced Expression of VEGF-B In Vitro*", Viruses,12(2) 200, 2020. *these authors contributed equally to this work

3. **Federico Armando***, Matteo Gambini*, Attilio Corradi, Kathrin Becker, Katarzyna Marek, Vanessa M. Pfankuche, Ahmed E. Mergani, Graham Brogden, Nicole de Buhr, Maren von Köckritz-Blickwede, Hassan Y. Naim, Wolfgang Baumgärtner, Christina Puff. "*Mesenchymal to epithelial transition driven by canine distemper virus infection of canine histiocytic sarcoma cells contributes to a reduced cell motility in vitro"*, Journal of Cellular and Molecular Medicine, 24:9332-9348, 2020. *these authors contributed equally to this work

4. Cristina Marchetti, Paolo Borghetti, Antonio Cacchioli, Luca Ferrari, **Federico Armando**, Attilio Corradi, Anna M. Cantoni. "*Profile of gamma-delta (γδ) T lymphocytes in the peripheral blood of crossbreed dogs during stages of life and implication in aging*", BMC Veterinary Research, 16:278-290, 2020

5. **Federico Armando***, Luca Ferrari*, Maria L. Arcari*, Giacomo Azzali, Davide Dallatana, Maura Ferrari, Guerino Lombardi, Matteo Zanfabro, Rosanna Di Lecce, Paolo Lunghi, Ewan R. Cameron, Anna M. Cantoni*, Attilio Corradi*. "*Endocanalicular transendothelial crossing (ETC): a novel intravasation mode used by HEK-EBNA293-3 VEGF-D cells during the metastatic process in a xenograft model*", PlosOne Oct 21;15(10) 2020.*these authors contributed equally to this work

6. **Federico Armando***, Claudio Pigoli*, Matteo Gambini*, Andrea Ghidelli, Gabriele Ghisleni, Attilio Corradi, Benedetta Passeri, Mario Caniatti, Valeria Grieco, Wolfgang Baumgärtner, Christina Puff. "*Peripheral nerve sheath tumors resembling human atypical neurofibroma in goldfish (Carassius auratus)*". Under review in Veterinary Pathology.

7. **Federico Armando**, Francesco Godizzi, Elisabetta Razzuoli, Attilio Corradi, Luca Ferrari, Benedetta Passeri "*Epithelial to Mesenchymal Transition (EMT) in a Laryngeal Squamous Cell Carcinoma of a Horse*: futurLe perspectives". Under eview in Animals.

8. Marco Genchi, Alice Vismarra, Alessandra Favilli, Paolo Bonilauri, Paola Prati, Lavinia Ciuca, Benedetta Passeri, **Federico Armando**, Laura Kramer " First report of Echinococcus granulosus sensu lato genotype G7 in domestic pigs from Italy". Under review Veterinary Parasitology: Regional Studies and Reports

CONFERENCES:

1. LXXII SISVET Congress in veterinary medicine, Turin, 20-22 June 2018; Oral presentation: "MORPHOLOGICAL STUDY OF NEOPLASTIC CELL INTRAVASATION": Federico Armando, Anna Maria Cantoni, Giacomo Azzali, Maria Luisa Arcari, Rosanna Di Lecce, Attilio Corradi

2. LXXIII SISVET Congress in veterinary medicine, Olbia, 19-22 June 2019; poster: "A CASE OF EQUINE DYSAUTONOMIA": Benedetta Passeri, Mario Angelone, Isabella Nicolasi, Federico Armando, Attilio Corradi, Anna Maria Cantoni

3. LXXIII SISVET Congress in veterinary medicine, Olbia, 19-22 June 2019; poster: "SQUAMOUS CELL CARCINOMA OF THE EPIGLOTTIS AND LARYNGEAL MUCOSA IN A HORSE": Benedetta Passeri, Federico Armando, Laura Pecorari, Francesca Altomare, Attilio Corradi, Anna Maria Cantoni

4. ESVP/ECVP Joint congress of European Veterinary Pathology and veterinary clinical pathology, Arhnem, 25-28 september 2019; poster: "INFLUENCE OF CANINE DISTEMPER VIRUS ON MESENCHYMAL TO EPITHELIAL TRANSITION IN CANINE HISTIOCYTIC SARCOMA CELL LINE" Federico Armando, Vanessa Maria Pfankuche, Wolfgang Baumagärtner, Christina Puff

5. LXIII German pathologists national congress, Fulda 6-8 March 2020; poster: "OXIDATIVE STRESS IN CANINE HISTIOCYTIC SARCOMA CELLS (DH82 CELLS) INDUCED BY A PERSISTENT CANINE DISTEMPER VIRUS INFECTION LEADS TO IMPAIRMENT OF THE HIF-1A DOWNSTREAM PATHWAY IN VITRO" Federico Armando, Matteo Gambini, Attilio Corradi, Chiara Giudice, Vanessa M. Pfankuche, Graham Brogden, Friederike Attig, Maren von Köckritz-Blickwede, Wolfgang Baumgärtner, Christina Puff.

6. LXIII German pathologists national congress, Fulda 6-8 March 2020; oral presentation: "CANINE DISTEMPER VIRUS TRIGGERS MESENCHYMAL TO EPITHELIAL TRANSITION IN CANINE HISTIOCYTIC SARCOMA CELLS" Federico Armando, Matteo Gambini*, Attilio Corradi, Vanessa M. Pfankuche, Ahmed E. Mergani, Graham Brogden, Maren von Köckritz-Blickwede, Wolfgang Baumgärtner, Christina Puff

ACKNOWLEDGEMENTS

I would like to express my sincere gratitude to all people who have helped and inspired me during these years. The results I have obtained today would never been possible to be presented without the precious help and support that I received from everyone.

First and foremost, I would like to express my utmost gratitude to my two tutors that believed in me and helped me to set up my future career, Prof. Attilio Corradi and Prof. Wolfgang Baumgärtner. Prof Cantoni and Prof Passeri for the precious support within the everyday lab-life. Dr. Christina Puff for the big patience and the precious suggestion and support that helped me to give shape to the current project. A huge “thank you” must be said to all my colleagues from TiHo that helped me in everyday life both inside and outside the lab. Dr. Luca Ferrari for the support in the hardest moments and to be always ready for helping and transmitting the so-called love for Science. Dr. Matteo Gambini for inspiring me with his infinite energy and skills, inspiring me inside and outside working life. In the end, everything would have been nothing without my family beside me, this is for Isabella, Cesare, Paolo, Corina, Ines, Walter, Silvia, Anna. The last, but not the least, to Samuela for being always from my side in every moment, supporting me for any choice and decision during the best and even the worse moments.

REFERENCES

1. Moore PF. A review of histiocytic diseases of dogs and cats. Vet Pathol. 2014;51(1):167–84.
2. Kraje AC, Patton CS, Edwards DF. Malignant histiocytosis in 3 cats. J Vet Intern Med. 2001;15(3):252–6.
3. D’Agostino PM, Gottfried-Blackmore A, Anandasabapathy N, Bulloch K. Brain dendritic cells: biology and pathology. Acta Neuropathol. 2012;124(5):599–614.
4. Pires I, Queiroga FL, Alves A, Silva F, Lopes C. Decrease of E-cadherin expression in canine cutaneous histiocytoma appears to be related to its

spontaneous regression. Anticancer Res. 2009;29(7):2713–7.

5. Coomer AR, Liptak JM. Canine histiocytic diseases. Compend Contin Educ Pract Vet Am Ed. 2008;30(4):202.
6. Fulmer AK, Mauldin GE. Canine histiocytic neoplasia: an overview. Can Vet J. 2007;48(10):1041.
7. Kelly DF. Canine Cutaneous Histiocytoma A Light and Electron Microscopic Study. Pathol Vet. 1970;7(1):12–27.
8. Dobson JM, Samuel S, Milstein H, Rogers K, Wood JLN. Canine neoplasia in the UK: estimates of incidence rates from a population of insured dogs. J Small Anim Pract. 2002;43(6):240–6.
9. Puff C, Risha E, Baumgärtner W. Regression of canine cutaneous histiocytoma is associated with an orchestrated expression of matrix metalloproteinases. J Comp Pathol. 2013;149(2–3):208–15.
10. Faller M, Lamm C, Affolter VK, Valerius K, Schwartz S, Moore PF. Retrospective characterisation of solitary cutaneous histiocytoma with lymph node metastasis in eight dogs. J Small Anim Pract. 2016;57(10):548–52.

11. Taylor DON, Dorn CR, Luis OH. Morphologic and biologic characteristics of the canine cutaneous histiocytoma. Cancer Res. 1969;29(1):83–92.
12. Kaim U, Moritz A, Failing K, Baumgärtner W. The regression of a canine Langerhans cell tumour is associated with increased expression of IL-2, TNF-α, IFN-γ and iNOS mRNA. Immunology. 2006;118(4):472–82.
13. Guvenc T, Haligur M, Orman MN, al. et. Mitosis and apoptosis in canine cutaneous histiocytoma and transmissible venereal tumour. Acta Vet Hung. 2002;50(3):315–21.
14. Pires I, Rodrigues P, Alves A, Queiroga FL, Silva F, Lopes C. Immunohistochemical and immunoelectron study of major histocompatibility complex class-II antigen in canine cutaneous histiocytoma: Its relation to tumor regression. In Vivo (Brooklyn). 2013;27(2):257–62.
15. Marchal T, Dezutter-Dambuyant C, Fournel C, Magnol JP, Schmitt D. Immunophenotypic and ultrastructural evidence of the Langerhans cell origin of the canine cutaneous histiocytoma. Cells Tissues Organs. 1995;153(3):189–202.
16. Moore PF, Schrenzel MD, Affolter VK, Olivry T, Naydan D. Canine cutaneous histiocytoma is an epidermotropic langerhans cell histiocytosis that expresses CD1 and specific β2-integrin molecules. Am J Pathol. 1996;148(5):1699–708.
17. Affolter VK, Moore PF. Canine cutaneous and systemic histiocytosis: reactive histiocytosis of dermal dendritic cellsNANA. Am J Dermatopathol. 2000;22(1):40–8.
18. Mays MB, Bergeron JA. Cutaneous histiocytosis in dogs. J Am Vet Med Assoc. 1986;188(4):377–81.
19. Palmeiro BS, Morris DO, Goldschmidt MH, Mauldin EA. Cutaneous reactive histiocytosis in dogs: a retrospective evaluation of 32 cases. Vet Dermatol. 2007;18(5):332–40.
20. Moore PF. Systemic histiocytosis of Bernese mountain dogs. Vet Pathol. 1984;21(6):554–63.

21. Moore PF, Rosin A. Malignant histiocytosis of Bernese mountain dogs. Vet Pathol. 1986;23(1):1–10.
22. Padgett GA, Madewell BR, Keller ET, Jodar L, Packard M. Inheritance of histiocytosis in Bernese mountain dogs. J Small Anim Pract. 1995;36(3):93–8.
23. Ide T, Uchida K, Kagawa Y, Suzuki K, Nakayama H. Pathological and immunohistochemical features of subdural histiocytic sarcomas in 15 dogs. J Vet Diagnostic Investig. 2011;23(1):127–32.
24. Poirier VJ, Burgess KE, Adams WM, Vail DM. Toxicity, dosage, and efficacy of vinorelbine (Navelbine) in dogs with spontaneous neoplasia. J Vet Intern Med. 2004;18(4):536–9.
25. Merlo DF, Rossi L, Pellegrino C, Ceppi M, Cardellino U, Capurro C, et al. Cancer incidence in pet dogs: findings of the Animal Tumor Registry of Genoa, Italy. J Vet Intern Med. 2008;22(4):976–84.
26. Patil SS, Gentschev I, Nolte I, Ogilvie G, Szalay AA. Oncolytic virotherapy in veterinary medicine: Current status and future prospects for canine patients. J Transl Med [Internet]. 2012;10(1):3. Available from: http://www.translational-medicine.com/content/10/1/3
27. Sinkovics J, Horvath J. New developments in the virus therapy of cancer: a historical review. Intervirology. 1993;36(4):193–214.
28. Sinkovics JG, Horvath JC. Newcastle disease virus (NDV): brief history of its oncolytic strains. J Clin Virol. 2000;16(1):1–15.
29. Southam CM, Moore AE. Clinical studies of viruses as antineoplastic agents, with particular reference to Egypt 101 virus. Cancer. 1952;5(5):1025–34.
30. Pack GT. Note on the experimental use of rabies vaccine for melanomatosis. AMA Arch dermatology Syphilol. 1950;62(5):694–5.
31. Southam CM, Hilleman MR, Werner JH. Pathogenicity and oncolytic capacity of RI virus strain RI-67 in man. J Lab Clin Med. 1956;47(4):573–82.
32. Asada T. Treatment of human cancer with mumps virus. Cancer. 1974;34(6):1907–28.

33. Okuno Y, Asada T, Yamanishi K, Otsuka T, Takahashi M, Tanioka T, et al. Studies on the use of mumps virus for treatment of human cancer. Biken J. 1978;21(2):37.
34. Vähä-Koskela MJV, Heikkilä JE, Hinkkanen AE. Oncolytic viruses in cancer therapy. Cancer Lett. 2007;254(2):178–216.
35. Phuangsab A, Lorence RM, Reichard KW, Peeples ME, Walter RJ. Newcastle disease virus therapy of human tumor xenografts: antitumor effects of local or systemic administration. Cancer Lett. 2001;172(1):27–36.
36. Hirasawa K, Nishikawa SG, Norman KL, Coffey MC, Thompson BG, Yoon C-S, et al. Systemic reovirus therapy of metastatic cancer in immune-competent mice. Cancer Res. 2003;63(2):348–53.
37. De Palma M, Venneri MA, Naldini L. In vivo targeting of tumor endothelial cells by systemic delivery of lentiviral vectors. Hum Gene Ther. 2003;14(12):1193–206.
38. Fu X, Zhang X. Delivery of herpes simplex virus vectors through liposome formulation. Mol Ther. 2001;4(5):447–53.
39. Shafren DR, Au GG, Nguyen T, Newcombe NG, Haley ES, Beagley L, et al. Systemic therapy of malignant human melanoma tumors by a common cold-producing enterovirus, coxsackievirus a21. Clin cancer Res. 2004;10(1):53–60.
40. Tseng J-C, Levin B, Hurtado A, Yee H, De Castro IP, Jimenez M, et al. Systemic tumor targeting and killing by Sindbis viral vectors. Nat Biotechnol. 2004;22(1):70–7.
41. Vähä-Koskela MJ V, Kallio JP, Jansson LC, Heikkilä JE, Zakhartchenko VA, Kallajoki MA, et al. Oncolytic capacity of attenuated replicative semliki forest virus in human melanoma xenografts in severe combined immunodeficient mice. Cancer Res. 2006;66(14):7185–94.
42. Reddy PS, Burroughs KD, Hales LM, Ganesh S, Jones BH, Idamakanti N, et al. Seneca Valley virus, a systemically deliverable oncolytic picornavirus, and the treatment of neuroendocrine cancers. J Natl cancer Inst. 2007;99(21):1623–33.

43. Zhang Q, Yong AY, Wang E, Chen N, Danner RL, Munson PJ, et al. Eradication of solid human breast tumors in nude mice with an intravenously injected light-emitting oncolytic vaccinia virus. Cancer Res. 2007;67(20):10038–46.
44. Lun X, Yang W, Alain T, Shi Z-Q, Muzik H, Barrett JW, et al. Myxoma virus is a novel oncolytic virus with significant antitumor activity against experimental human gliomas. Cancer Res. 2005;65(21):9982–90.
45. Evgin L, Vähä-Koskela M, Rintoul J, Falls T, Le Boeuf F, Barrett JW, et al. Potent oncolytic activity of raccoonpox virus in the absence of natural pathogenicity. Mol Ther. 2010;18(5):896–902.
46. Jourdier TM, Moste C, Bonnet MC, Delisle F, Tafani JP, Devauchelle P, et al. Local immunotherapy of spontaneous feline fibrosarcomas using recombinant poxviruses expressing interleukin 2 (IL2). Gene Ther. 2003;10(26):2126–32.
47. Paoloni M, Khanna C. Translation of new cancer treatments from pet dogs to humans. Nat Rev Cancer. 2008;8(2):147–56.
48. Khanna C, London C, Vail D, Mazcko C, Hirschfeld S. Guiding the optimal translation of new cancer treatments from canine to human cancer patients. Clin cancer Res. 2009;15(18):5671–7.
49. De Maria R, Olivero M, Iussich S, Nakaichi M, Murata T, Biolatti B, et al. Spontaneous feline mammary carcinoma is a model of HER2 overexpressing poor prognosis human breast cancer. Cancer Res. 2005;65(3):907–12.
50. Tang J, Le S, Sun L, Yan X, Zhang M, MacLeod J, et al. Copy number abnormalities in sporadic canine colorectal cancers. Genome Res. 2010;20(3):341–50.
51. Rowell JL, McCarthy DO, Alvarez CE. Dog models of naturally occurring cancer. Trends Mol Med. 2011;17(7):380–8.
52. Wypij JM. A naturally occurring feline model of head and neck squamous cell carcinoma. Patholog Res Int. 2013;2013.
53. Vail DM, Macewen EG. Spontaneously occurring tumors of companion animals as models for human cancer. Cancer Invest. 2000;18(8):781–92.

54. Gentschev I, Patil SS, Petrov I, Cappello J, Adelfinger M, Szalay AA. Oncolytic virotherapy of canine and feline cancer. Viruses. 2014;6(5):2122–37.
55. Lapp S, Pfankuche VM, Baumgärtner W, Puff C. Viral oncolysis - Can insights from measles be transferred to canine distemper virus? Viruses. 2014;6(6):2340–75.
56. Zhang S-C, Wang W-L, Cai W-S, Jiang K-L, Yuan Z-W. Engineered measles virus Edmonston strain used as a novel oncolytic viral system against human hepatoblastoma. BMC Cancer. 2012;12(1):1–10.
57. Zhao D, Chen P, Yang H, Wu Y, Zeng X, Zhao Y, et al. Live attenuated measles virus vaccine induces apoptosis and promotes tumor regression in lung cancer. Oncol Rep. 2013;29(1):199–204.
58. Parato KA, Senger D, Forsyth PAJ, Bell JC. Recent progress in the battle between oncolytic viruses and tumours. Nat Rev Cancer. 2005;5(12):965–76.
59. Allavena P, Sica A, Garlanda C, Mantovani A. The Yin-Yang of tumor-associated macrophages in neoplastic progression and immune surveillance. Immunol Rev. 2008;222(1):155–61.
60. Mantovani A, Allavena P, Sica A. Tumour-associated macrophages as a prototypic type II polarised phagocyte population: role in tumour progression. Eur J Cancer. 2004;40(11):1660–7.
61. Schmieder A, Michel J, Schönhaar K, Goerdt S, Schledzewski K. Differentiation and gene expression profile of tumor-associated macrophages. In: Seminars in cancer biology. Elsevier; 2012. p. 289–97.
62. Guo C, Buranych A, Sarkar D, Fisher PB, Wang X-Y. The role of tumor-associated macrophages in tumor vascularization. Vasc Cell. 2013;5(1):1–12.
63. Hagemann T, Lawrence T, McNeish I, Charles KA, Kulbe H, Thompson RG, et al. “Re-educating” tumor-associated macrophages by targeting NF-κB. J Exp Med. 2008;205(6):1261–8.

64. Dalton DK, Pitts-Meek S, Keshav S, Figari IS, Bradley A, Stewart TA. Multiple defects of immune cell function in mice with disrupted interferon-gamma genes. Science (80-). 1993;259(5102):1739–42.
65. Gordon S. Alternative activation of macrophages. Nat Rev Immunol. 2003;3(1):23–35.
66. Yao L, Sgadari C, Furuke K, Bloom ET, Teruya-Feldstein J, Tosato G. Contribution of natural killer cells to inhibition of angiogenesis by interleukin-12. Blood, J Am Soc Hematol. 1999;93(5):1612–21.
67. Yao L, Pike SE, Setsuda J, Parekh J, Gupta G, Raffeld M, et al. Effective targeting of tumor vasculature by the angiogenesis inhibitors vasostatin and interleukin-12. Blood, J Am Soc Hematol. 2000;96(5):1900–5.
68. Yao L, Pike SE, Pittaluga S, Cherney B, Gupta G, Jaffe ES, et al. Anti-tumor activities of the angiogenesis inhibitors interferon-inducible protein-10 and the calreticulin fragment vasostatin. Cancer Immunol Immunother. 2002;51(7):358–66.
69. Angiolillo AL, Sgadari C, Taub DD, Liao F, Farber JM, Maheshwari S, et al. Human interferon-inducible protein 10 is a potent inhibitor of angiogenesis in vivo. J Exp Med. 1995;182(1):155–62.
70. Sgadari C, Angiolillo AL, Tosato G. Inhibition of angiogenesis by interleukin-12 is mediated by the interferon-inducible protein 10. 1996;
71. Schuster M, Nechansky A, Kircheis R. Cancer immunotherapy. Biotechnol J Healthc Nutr Technol. 2006;1(2):138–47.
72. Sinkovics JG, Horvath JC. Evidence accumulating in support of cancer vaccines combined with chemotherapy: a pragmatic review of past and present efforts. Int J Oncol. 2006;29(4):765–77.
73. Cassel WA, Garrett RE. Newcastle disease virus as an antineoplastic agent. Cancer. 1965;18(7):863–8.

74. Csatary LK, Gosztonyi G, Szeberenyi J, Fabian Z, Liszka V, Bodey B, et al. MTH-68/H oncolytic viral treatment in human high-grade gliomas. J Neurooncol. 2004;67(1–2):83–93.
75. Saika S, Kidokoro M, Kubonoya H, Ito K, Ohkawa T, Aoki A, et al. Development and biological properties of a new live attenuated mumps vaccine. Comp Immunol Microbiol Infect Dis. 2006;29(2–3):89–99.
76. Yan Y-F, Chen X, Zhu Y, Wu J-G, Dong C-Y. Selective cytolysis of tumor cells by mumps virus S79. Intervirology. 2005;48(5):292–6.
77. Taqi AM, Abdurrahman MB, Yakubu AM, Fleming AF. Regression of Hodgkin's disease after measles. Lancet. 1981;317(8229):1112.
78. Grote D, Russell SJ, Cornu TI, Cattaneo R, Vile R, Poland GA, et al. Live attenuated measles virus induces regression of human lymphoma xenografts in immunodeficient mice. Blood, J Am Soc Hematol. 2001;97(12):3746–54.
79. Peng K-W, TenEyck CJ, Galanis E, Kalli KR, Hartmann LC, Russell SJ. Intraperitoneal therapy of ovarian cancer using an engineered measles virus. Cancer Res. 2002;62(16):4656–62.
80. Heinzerling L, Künzi V, Oberholzer PA, Kündig T, Naim H, Dummer R. Oncolytic measles virus in cutaneous T-cell lymphomas mounts antitumor immune responses in vivo and targets interferon-resistant tumor cells. Blood. 2005;106(7):2287–94.
81. Kinoh H, Inoue M, Washizawa K, Yamamoto T, Fujikawa S, Tokusumi Y, et al. Generation of a recombinant Sendai virus that is selectively activated and lyses human tumor cells expressing matrix metalloproteinases. Gene Ther. 2004;11(14):1137–45.
82. Sato H, Yoneda M, Honda T, Kai C. Morbillivirus receptors and tropism: multiple pathways for infection. Front Microbiol. 2012;3:75.
83. Pratakpiriya W, Seki F, Otsuki N, Sakai K, Fukuhara H, Katamoto H, et al. Nectin4 is an epithelial cell receptor for canine distemper virus and involved in neurovirulence. J Virol. 2012;86(18):10207–10.

84. Suter SE, Chein MB, Von Messling V, Yip B, Cattaneo R, Vernau W, et al. In vitro canine distemper virus infection of canine lymphoid cells: a prelude to oncolytic therapy for lymphoma. Clin Cancer Res. 2005;11(4):1579–87.
85. Tatsuo H, Ono N, Yanagi Y. Morbilliviruses use signaling lymphocyte activation molecules (CD150) as cellular receptors. J Virol. 2001;75(13):5842–50.
86. Zipperle L, Langedijk JPM, Örvell C, Vandevelde M, Zurbriggen A, Plattet P. Identification of key residues in virulent canine distemper virus hemagglutinin that control CD150/SLAM-binding activity. J Virol. 2010;84(18):9618–24.
87. Von Messling V, Oezguen N, Zheng Q, Vongpunsawad S, Braun W, Cattaneo R. Nearby clusters of hemagglutinin residues sustain SLAM-dependent canine distemper virus entry in peripheral blood mononuclear cells. J Virol. 2005;79(9):5857–62.
88. Tatsuo H, Ono N, Tanaka K, Yanagi Y. SLAM (CDw150) is a cellular receptor for measles virus. Nature. 2000;406(6798):893–7.
89. Pfankuche VM, Spitzbarth I, Lapp S, Ulrich R, Deschl U, Kalkuhl A, et al. Reduced angiogenic gene expression in morbillivirus-triggered oncolysis in a translational model for histiocytic sarcoma. J Cell Mol Med. 2017;21(4):816–30.
90. Gröne A, Fonfara S, Baumgärtner W. Cell type-dependent cytokine expression after canine distemper virus infection. Viral Immunol. 2002;15(3):493–505.
91. Puff C, Krudewig C, Imbschweiler I, Baumgärtner W, Alldinger S. Influence of persistent canine distemper virus infection on expression of RECK, matrix-metalloproteinases and their inhibitors in a canine macrophage/monocytic tumour cell line (DH82). Vet J. 2009;182(1):100–7.
92. Pfankuche VM, Sayed-Ahmed M, Contioso VB, Spitzbarth I, Rohn K, Ulrich R, et al. Persistent morbillivirus infection leads to altered cortactin distribution in histiocytic sarcoma cells with decreased cellular migration capacity. PLoS One. 2016;11(12):e0167517.

93. Beineke A, Puff C, Seehusen F, Baumgärtner W. Pathogenesis and immunopathology of systemic and nervous canine distemper. Vet Immunol Immunopathol. 2009;127(1–2):1–18.
94. Hanahan D, Folkman J. Patterns and emerging mechanisms of the angiogenic switch during tumorigenesis. Cell. 1996;86(3):353–64.
95. Baeriswyl V, Christofori G. The angiogenic switch in carcinogenesis. In: Seminars in cancer biology. Elsevier; 2009. p. 329–37.
96. Bergers G, Benjamin LE. Tumorigenesis and the angiogenic switch. Nat Rev cancer. 2003;3(6):401–10.
97. Ferrara N. Vascular endothelial growth factor. Arterioscler Thromb Vasc Biol. 2009;29(6):789–91.
98. Gabhann F Mac, Popel AS. Systems biology of vascular endothelial growth factors. Microcirculation. 2008;15(8):715–38.
99. Carmeliet P. VEGF as a key mediator of angiogenesis in cancer. Oncology. 2005;69(Suppl. 3):4–10.
100. Bertout JA, Patel SA, Simon MC. The impact of O 2 availability on human cancer. Nat Rev Cancer. 2008;8(12):967–75.
101. Challapalli A, Carroll L, Aboagye EO. Molecular mechanisms of hypoxia in cancer. Clin Transl imaging. 2017;5(3):225–53.
102. Pisoschi AM, Pop A. The role of antioxidants in the chemistry of oxidative stress: A review. Eur J Med Chem. 2015;97:55–74.
103. Mittal M, Siddiqui MR, Tran K, Reddy SP, Malik AB. Reactive oxygen species in inflammation and tissue injury. Antioxid Redox Signal. 2014;20(7):1126–67.
104. Schieber M, Chandel NS. ROS function in redox signaling and oxidative stress. Curr Biol. 2014;24(10):R453–62.
105. Fiaschi T, Chiarugi P. Oxidative stress, tumor microenvironment, and metabolic reprogramming: a diabolic liaison. Int J Cell Biol. 2012;2012.

106. Attig F, Spitzbarth I, Kalkuhl A, Deschl U, Puff C, Baumgärtner W, et al. Reactive oxygen species are key mediators of demyelination in canine distemper leukoencephalitis but not in Theiler's murine encephalomyelitis. Int J Mol Sci. 2019;20(13):3217.
107. Bürge T, Griot C, Vandevelde M, Peterhans E. Antiviral antibodies stimulate production of reactive oxygen species in cultured canine brain cells infected with canine distemper virus. J Virol. 1989;63(6):2790–7.
108. Griot C, Bürge T, Vandevelde M, Peterhans E. Antibody-induced generation of reactive oxygen radicals by brain macrophages in canine distemper encephalitis: a mechanism for bystander demyelination. Acta Neuropathol. 1989;78(4):396–403.
109. Karadeniz A, Hanedan B, Cemek M, Borku MK. Relationship between canine distemper and oxidative stress in dogs. Rev Med Vet. 2008;159:462–7.
110. Stein VM, Czub M, Schreiner N, Moore PF, Vandevelde M, Zurbriggen A, et al. Microglial cell activation in demyelinating canine distemper lesions. J Neuroimmunol. 2004;153(1–2):122–31.
111. Semenza GL, Wang GL. A nuclear factor induced by hypoxia via de novo protein synthesis binds to the human erythropoietin gene enhancer at a site required for transcriptional activation. Mol Cell Biol. 1992;12(12):5447–54.
112. Wang GL, Semenza GL. Characterization of hypoxia-inducible factor 1 and regulation of DNA binding activity by hypoxia. J Biol Chem. 1993;268(29):21513–8.
113. Wang GL, Jiang B-H, Rue EA, Semenza GL. Hypoxia-inducible factor 1 is a basic-helix-loop-helix-PAS heterodimer regulated by cellular O2 tension. Proc Natl Acad Sci. 1995;92(12):5510–4.
114. Kewley RJ, Whitelaw ML, Chapman-Smith A. The mammalian basic helix–loop–helix/PAS family of transcriptional regulators. Int J Biochem Cell Biol. 2004;36(2):189–204.

115. Kaelin Jr WG, Ratcliffe PJ. Oxygen sensing by metazoans: the central role of the HIF hydroxylase pathway. Mol Cell. 2008;30(4):393–402.
116. Jiang B-H, Zheng JZ, Leung SW, Roe R, Semenza GL. Transactivation and inhibitory domains of hypoxia-inducible factor 1α modulation of transcriptional activity by oxygen tension. J Biol Chem. 1997;272(31):19253–60.
117. Pugh CW, O'Rourke JF, Nagao M, Gleadle JM, Ratcliffe PJ. Activation of hypoxia-inducible factor-1; definition of regulatory domains within the α subunit. J Biol Chem. 1997;272(17):11205–14.
118. Wenger RH, Stiehl DP, Camenisch G. Integration of oxygen signaling at the consensus HRE. Sci STKE. 2005;2005(306):re12–re12.
119. Minet E, Michel G, Mottet D, Raes M, Michiels C. Transduction pathways involved in Hypoxia-Inducible Factor-1 phosphorylation and activation. Free Radic Biol Med. 2001;31(7):847–55.
120. Bae S-H, Jeong J-W, Park JA, Kim S-H, Bae M-K, Choi S-J, et al. Sumoylation increases HIF-1α stability and its transcriptional activity. Biochem Biophys Res Commun. 2004;324(1):394–400.
121. Sumbayev V V, Budde A, Zhou J, Brüne B. HIF-1α protein as a target for S-nitrosation. FEBS Lett. 2003;535(1–3):106–12.
122. Jung F, Palmer LA, Zhou N, Johns RA. Hypoxic regulation of inducible nitric oxide synthase via hypoxia inducible factor-1 in cardiac myocytes. Circ Res. 2000;86(3):319–25.
123. Fong G-H. Mechanisms of adaptive angiogenesis to tissue hypoxia. Angiogenesis. 2008;11(2):121–40.
124. Krock BL, Skuli N, Simon MC. Hypoxia-Induced Angiogenesis: Good and Evil. Genes and Cancer. 2011;2(12):1117–33.
125. Folkman J. Angiogenesis in cancer, vascular, rheumatoid and other disease. Nat Med. 1995;1(1):27–30.

126. Parangi S, O'Reilly M, Christofori G, Holmgren L, Grosfeld J, Folkman J, et al. Antiangiogenic therapy of transgenic mice impairs de novo tumor growth. Proc Natl Acad Sci. 1996;93(5):2002–7.
127. Ravi R, Mookerjee B, Bhujwalla ZM, Sutter CH, Artemov D, Zeng Q, et al. Regulation of tumor angiogenesis by p53-induced degradation of hypoxia-inducible factor 1α. Genes Dev. 2000;14(1):34–44.
128. Selak MA, Armour SM, MacKenzie ED, Boulahbel H, Watson DG, Mansfield KD, et al. Succinate links TCA cycle dysfunction to oncogenesis by inhibiting HIF-α prolyl hydroxylase. Cancer Cell. 2005;7(1):77–85.
129. Kikuchi H, Pino MS, Zeng M, Shirasawa S, Chung DC. Oncogenic KRAS and BRAF differentially regulate hypoxia-inducible factor-1α and-2α in colon cancer. Cancer Res. 2009;69(21):8499–506.
130. Maxwell PH, Dachs GU, Gleadle JM, Nicholls LG, Harris AL, Stratford IJ, et al. Hypoxia-inducible factor-1 modulates gene expression in solid tumors and influences both angiogenesis and tumor growth. Proc Natl Acad Sci. 1997;94(15):8104–9.
131. Ceradini DJ, Kulkarni AR, Callaghan MJ, Tepper OM, Bastidas N, Kleinman ME, et al. Progenitor cell trafficking is regulated by hypoxic gradients through HIF-1 induction of SDF-1. Nat Med. 2004;10(8):858–64.
132. Kioi M, Vogel H, Schultz G, Hoffman RM, Harsh GR, Brown JM. Inhibition of vasculogenesis, but not angiogenesis, prevents the recurrence of glioblastoma after irradiation in mice. J Clin Invest. 2010;120(3):694–705.
133. Kawanaka T, Ikushima H, Osaki K, Furutani S, Kubo A, Kudoh T, et al. Prognostic Significance of HIF-2alpha Expression on Tumor Infiltrating Macrophages in Patients with FIGO Stage IIIb Uterine Cervical Cancer undergoing Radiotherapy. Int J Radiat Oncol Biol Phys. 2008;72(1):S369.
134. Cramer T, Yamanishi Y, Clausen BE, Förster I, Pawlinski R, Mackman N, et al. HIF-1α is essential for myeloid cell-mediated inflammation. Cell. 2003;112(5):645–57.

135. Thiery JP, Acloque H, Huang RYJ, Nieto MA. Epithelial-Mesenchymal Transitions in Development and Disease. Cell. 2009;139(5):871–90.
136. Wheelock MJ, Shintani Y, Maeda M, Fukumoto Y, Johnson KR. Cadherin switching. J Cell Sci. 2008;121(6):727–35.
137. Scarpa E, Szabó A, Bibonne A, Theveneau E, Parsons M, Mayor R. Cadherin switch during EMT in neural crest cells leads to contact inhibition of locomotion via repolarization of forces. Dev Cell. 2015;34(4):421–34.
138. Huang RYJ, Guilford P, Thiery JP. Early events in cell adhesion and polarity during epithelialmesenchymal transition. J Cell Sci. 2012;125(19):4417–22.
139. Greenburg G, Hay ED. Epithelia suspended in collagen gels can lose polarity and express characteristics of migrating mesenchymal cells. J Cell Biol. 1982;95(1):333–9.
140. Bedi U, Mishra VK, Wasilewski D, Scheel C, Johnsen SA. Epigenetic plasticity: a central regulator of epithelial-to-mesenchymal transition in cancer. Oncotarget. 2014;5(8):2016.
141. Meyer-Schaller N, Cardner M, Diepenbruck M, Saxena M, Tiede S, Lüönd F, et al. A hierarchical regulatory landscape during the multiple stages of EMT. Dev Cell. 2019;48(4):539–53.
142. Baranwal S, Alahari SK. Molecular mechanisms controlling E-cadherin expression in breast cancer. Biochem Biophys Res Commun. 2009;384(1):6–11.
143. Serrano-Gomez SJ, Maziveyi M, Alahari SK. Regulation of epithelial-mesenchymal transition through epigenetic and post-translational modifications. Mol Cancer. 2016;15(1):1–14.
144. Puisieux A, Brabletz T, Caramel J. Oncogenic roles of EMT-inducing transcription factors. Nat Cell Biol. 2014;16(6):488–94.
145. Batlle E, Sancho E, Francí C, Domínguez D, Monfar M, Baulida J, et al. The transcription factor snail is a repressor of E-cadherin gene expression in epithelial tumour cells. Nat Cell Biol. 2000;2(2):84–9.

146. Barbera MJ, Puig I, Domínguez D, Julien-Grille S, Guaita-Esteruelas S, Peiro S, et al. Regulation of Snail transcription during epithelial to mesenchymal transition of tumor cells. Oncogene. 2004;23(44):7345–54.
147. Grille SJ, Bellacosa A, Upson J, Klein-Szanto AJ, Van Roy F, Lee-Kwon W, et al. The protein kinase Akt induces epithelial mesenchymal transition and promotes enhanced motility and invasiveness of squamous cell carcinoma lines. Cancer Res. 2003;63(9):2172–8.
148. Ordoñez-Moreno A, Rodriguez-Monterrosas C, Cortes-Reynosa P, Perez-Carreon JI, Perez Salazar E. Erythropoietin Induces an Epithelial to Mesenchymal Transition-Like Process in Mammary Epithelial Cells MCF10A. J Cell Biochem. 2017;118(9):2983–92.
149. Peinado H, Quintanilla M, Cano A. TGFβ-1 induces snail transcription factor in epithelial cell lines: mechanisms for epithelial mesenchymal transitions. J Biol Chem. 2003;278(21):113–23.
150. Zhou BP, Hung M-C. Wnt, hedgehog, and snail: sister pathways that control by GSK-3beta and beta-Trcp in the regulation of metastasis. Cell Cycle. 2005;4(6):772–6.
151. Yook JI, Li X-Y, Ota I, Fearon ER, Weiss SJ. Wnt-dependent regulation of the E-cadherin repressor snail. J Biol Chem. 2005;280(12):11740–8.
152. Radisky DC, Levy DD, Littlepage LE, Liu H, Nelson CM, Fata JE, et al. Rac1b and reactive oxygen species mediate MMP-3-induced EMT and genomic instability. Nature. 2005;436(7047):123–7.
153. Imai T, Horiuchi A, Wang C, Oka K, Ohira S, Nikaido T, et al. Hypoxia attenuates the expression of E-cadherin via up-regulation of SNAIL in ovarian carcinoma cells. Am J Pathol. 2003;163(4):1437–47.
154. Yang S, Zhang Z, Hao Y, Zhao Y, Qian F, Shi Y, et al. HIF-1α induces the epithelial-mesenchymal transition in gastric cancer stem cells through the Snail pathway. Oncotarget. 2017;8(6):9535.

155. Laffin B, Wellberg E, Kwak H-I, Burghardt RC, Metz RP, Gustafson T, et al. Loss of singleminded-2s in the mouse mammary gland induces an epithelial-mesenchymal transition associated with up-regulation of slug and matrix metalloprotease 2. Mol Cell Biol. 2008;28(6):1936–46.
156. Chakrabarti R, Hwang J, Blanco MA, Wei Y, Romano R, Smalley K, et al. HHS Public Access. 2013;14(11):1212–22.
157. Gras B, Jacqueroud L, Wierinckx A, Lamblot C, Fauvet F, Lachuer J, et al. Snail family members unequally trigger EMT and thereby differ in their ability to promote the neoplastic transformation of mammary epithelial cells. PLoS One. 2014;9(3):e92254.
158. Guaita S, Puig I, Francí C, Garrido M, Domínguez D, Batlle E, et al. Snail induction of epithelial to mesenchymal transition in tumor cells is accompanied by MUC1 repression andZEB1 expression. J Biol Chem. 2002;277(42):39209–16.
159. Dollfus H, Kumaramanickavel G, Biswas P, Stoetzel C, Quillet R, Denton M, et al. Identification of a new TWIST mutation (7p21) with variable eyelid manifestations supports locus homogeneity of BPES at 3q22. J Med Genet. 2001;38(7):470–2.
160. Castanon I, Baylies MK. A Twist in fate: evolutionary comparison of Twist structure and function. Gene. 2002;287(1–2):11–22.
161. Yang J. Mani SA, Donaher JL, Ramaswamy S, Itzykson RA, Come C, Savagner P, Gitelman I, Richardson A, Weinberg RA. Twist a master Regul Morphog Play an Essent role tumor metastasis Cell. 2004;117:927–39.
162. Yang J, Weinberg RA. Epithelial-mesenchymal transition: at the crossroads of development and tumor metastasis. Dev Cell. 2008;14(6):818–29.
163. Casas E, Kim J, Bendesky A, Ohno-Machado L, Wolfe CJ, Yang J. Snail2 is an essential mediator of Twist1-induced epithelial mesenchymal transition and metastasis. Cancer Res. 2011;71(1):245–54.

164. Gheldof A, Hulpiau P, Van Roy F, De Craene B, Berx G. Evolutionary functional analysis and molecular regulation of the ZEB transcription factors. Cell Mol Life Sci. 2012;69(15):2527–41.
165. Grooteclaes ML, Frisch SM. Evidence for a function of CtBP in epithelial gene regulation and anoikis. Oncogene. 2000;19(33):3823–8.
166. Vandewalle C, Van Roy F, Berx G. The role of the ZEB family of transcription factors in development and disease. Cell Mol life Sci. 2009;66(5):773–87.
167. Goossens S, Vandamme N, Van Vlierberghe P, Berx G. EMT transcription factors in cancer development re-evaluated: Beyond EMT and MET. Biochim Biophys Acta (BBA)-Reviews Cancer. 2017;1868(2):584–91.
168. Byles V, Zhu L, Lovaas JD, Chmilewski LK, Wang J, Faller D V, et al. SIRT1 induces EMT by cooperating with EMT transcription factors and enhances prostate cancer cell migration and metastasis. Oncogene. 2012;31(43):4619–29.
169. Kim DH, Xing T, Yang Z, Dudek R, Lu Q, Chen Y-H. Epithelial mesenchymal transition in embryonic development, tissue repair and cancer: a comprehensive overview. J Clin Med. 2018;7(1):1.
170. Schedl A. Renal abnormalities and their developmental origin. Nat Rev Genet. 2007;8(10):791–802.
171. Luna-Zurita L, Prados B, Grego-Bessa J, Luxán G, Del Monte G, Benguría A, et al. Integration of a Notch-dependent mesenchymal gene program and Bmp2-driven cell invasiveness regulates murine cardiac valve formation. J Clin Invest. 2010;120(10):3493–507.
172. Sugi Y, Yamamura H, Okagawa H, Markwald RR. Bone morphogenetic protein-2 can mediate myocardial regulation of atrioventricular cushion mesenchymal cell formation in mice. Dev Biol. 2004;269(2):505–18.
173. Ma L, Lu M-F, Schwartz RJ, Martin JF. Bmp2 is essential for cardiac cushion epithelial-mesenchymal transition and myocardial patterning. Development. 2005;132(24):5601–11.

174. Bosada FM, Devasthali V, Jones KA, Stankunas K. Wnt/β-catenin signaling enables developmental transitions during valvulogenesis. Development. 2016;143(6):1041–54.
175. Bischoff J. Endothelial-to-mesenchymal transition: Purposeful versus maladaptive differentiation. Circ Res. 2019;124(8):1163–5.
176. Ubil E, Duan J, Pillai ICL, Rosa-Garrido M, Wu Y, Bargiacchi F, et al. Mesenchymal–endothelial transition contributes to cardiac neovascularization. Nature. 2014;514(7524):585–90.
177. Yan C, Grimm WA, Garner WL, Qin L, Travis T, Tan N, et al. Epithelial to mesenchymal transition in human skin wound healing is induced by tumor necrosis factor-α through bone morphogenic protein-2. Am J Pathol. 2010;176(5):2247–58.
178. You S, Avidan O, Tariq A, Ahluwalia I, Stark PC, Kublin CL, et al. Role of epithelial–mesenchymal transition in repair of the lacrimal gland after experimentally induced injury. Invest Ophthalmol Vis Sci. 2012;53(1):126–35.
179. Xue Z-F, Wu X-M, Liu M. Hepatic regeneration and the epithelial to mesenchymal transition. World J Gastroenterol WJG. 2013;19(9):1380.
180. Liu Y. Cellular and molecular mechanisms of renal fibrosis. Nat Rev Nephrol. 2011;7(12):684.
181. Krenning G, Zeisberg EM, Kalluri R. The origin of fibroblasts and mechanism of cardiac fibrosis. J Cell Physiol. 2010;225(3):631–7.
182. Travers JG, Kamal FA, Robbins J, Yutzey KE, Blaxall BC. Cardiac fibrosis: the fibroblast awakens. Circ Res. 2016;118(6):1021–40.
183. Zhou B, von Gise A, Ma Q, Hu YW, Pu WT. Genetic fate mapping demonstrates contribution of epicardium-derived cells to the annulus fibrosis of the mammalian heart. Dev Biol. 2010;338(2):251–61.
184. Rout-Pitt N, Farrow N, Parsons D, Donnelley M. Epithelial mesenchymal transition (EMT): a universal process in lung diseases with implications for cystic fibrosis pathophysiology. Respir Res. 2018;19(1):136.

185. Giampieri S, Manning C, Hooper S, Jones L, Hill CS, Sahai E. Localized and reversible TGFβ signalling switches breast cancer cells from cohesive to single cell motility. Nat Cell Biol. 2009;11(11):1287–96.
186. Hazan BR, Phillips RG, Qiao FR. Norton, l., Aaronson, AS (2000). Exogenous Expression of N-Cadherin in Breast Cancer Cells Induces Cell Migration. Invasion, Metastasis J Cell Biol. 148:779–90.
187. Maeda M, Johnson KR, Wheelock MJ. Cadherin switching: essential for behavioral but not morphological changes during an epithelium-to-mesenchyme transition. J Cell Sci. 2005;118(5):873–87.
188. Huttenlocher A, Horwitz AR. Cold Spring Harbor Perspect. Biol. 2011;3(9):a005074.
189. Hynes RO. Integrins: bidirectional, allosteric signaling machines. Cell. 2002;110(6):673–87.
190. Sawada K, Mitra AK, Radjabi AR, Bhaskar V, Kistner EO, Tretiakova M, et al. Loss of E-cadherin promotes ovarian cancer metastasis via α5-integrin, which is a therapeutic target. Cancer Res. 2008;68(7):2329–39.
191. Xu W, Zhou W, Cheng M, Wang J, Liu Z, He S, et al. Hypoxia activates Wnt/β-catenin signaling by regulating the expression of BCL9 in human hepatocellular carcinoma. Sci Rep [Internet]. 2017;7(209):1–13. Available from: http://dx.doi.org/10.1038/srep40446
192. Kalluri R, Weinberg RA. The basics of epithelial-mesenchymal transition. J Clin Invest. 2009;119(6):1420–8.
193. Hamidi H, Ivaska J. Every step of the way: integrins in cancer progression and metastasis. Nat Rev Drug Discov. 2018;17(3):31–46.
194. Mercurio AM, Rabinovitz I, Shaw LM. The α6β4 integrin and epithelial cell migration. Curr Opin Cell Biol. 2001;13(5):541–5.

195. Lecharpentier A, Vielh P, Perez-Moreno P, Planchard D, Soria JC, Farace F. Detection of circulating tumour cells with a hybrid (epithelial/mesenchymal) phenotype in patients with metastatic non-small cell lung cancer. Br J Cancer. 2011;105(9):1338–41.
196. Yang J, Mani SA, Donaher JL, Ramaswamy S, Itzykson RA, Come C, et al. Twist, a master regulator of morphogenesis, plays an essential role in tumor metastasis. Cell. 2004;117(7):927–39.
197. Yu M, Bardia A, Wittner BS, Stott SL, Smas ME, Ting DT, et al. Circulating breast tumor cells exhibit dynamic changes in epithelial and mesenchymal composition. Science (80-). 2013;339(6119):580–4.
198. Rhim AD, Mirek ET, Aiello NM, Maitra A, Bailey JM, McAllister F, et al. EMT and dissemination precede pancreatic tumor formation. Cell. 2012;148(1–2):349–61.
199. Fischer KR, Durrans A, Lee S, Sheng J, Li F, Wong S, et al. HHS Public Access. 2016;527(7579):472–6.
200. Christiansen JJ, Rajasekaran AK. Reassessing epithelial to mesenchymal transition as a prerequisite for carcinoma invasion and metastasis. Cancer Res. 2006;66(17):8319–26.
201. Friedl P, Wolf K. Plasticity of cell migration: a multiscale tuning model. J Cell Biol. 2010;188(1):11–9.
202. Brierley J, O'Sullivan B, Asamura H, Byrd D, Huang SH, Lee A, et al. Global Consultation on Cancer Staging: promoting consistent understanding and use. Nat Rev Clin Oncol. 2019;1–9.
203. Zeisberg M, Neilson EG. Biomarkers for epithelial-mesenchymal transitions. J Clin Invest. 2009;119(6):1429–37.
204. Heimann R, Lan F, McBride R, Hellman S. Separating favorable from unfavorable prognostic markers in breast cancer: the role of E-cadherin. Cancer Res. 2000;60(2):298–304.

205. Aktas B, Tewes M, Fehm T, Hauch S, Kimmig R, Kasimir-Bauer S. Stem cell and epithelial-mesenchymal transition markers are frequently overexpressed in circulating tumor cells of metastatic breast cancer patients. Breast cancer Res. 2009;11(4):R46.
206. Gamba CO, Rodrigues MA, Gomes DA, Estrela-Lima A, Ferreira E, Cassali GD. The relationship between E-cadherin and its transcriptional repressors in spontaneously arising canine invasive micropapillary mammary carcinoma. J Comp Pathol. 2015;153(4):256–65.
207. Gama A, Paredes J, Gärtner F, Alves A, Schmitt F. Expression of E-cadherin, P-cadherin and β-catenin in canine malignant mammary tumours in relation to clinicopathological parameters, proliferation and survival. Vet J. 2008;177(1):45–53.
208. Elloul S, Bukholt Elstrand M, Nesland JM, Tropé CG, Kvalheim G, Goldberg I, et al. Snail, Slug, and Smad-interacting protein 1 as novel parameters of disease aggressiveness in metastatic ovarian and breast carcinoma. Cancer Interdiscip Int J Am Cancer Soc. 2005;103(8):1631–43.
209. Elloul S, Silins I, Tropé CG, Benshushan A, Davidson B, Reich R. Expression of E-cadherin transcriptional regulators in ovarian carcinoma. Virchows Arch. 2006;449(5):520–8.
210. Cai M-Y, Luo R-Z, Chen J-W, Pei X-Q, Lu J-B, Hou J-H, et al. Overexpression of ZEB2 in peritumoral liver tissue correlates with favorable survival after curative resection of hepatocellular carcinoma. PLoS One. 2012;7(2):e32838.
211. Miyoshi A, Kitajima Y, Kido S, Shimonishi T, Matsuyama S, Kitahara K, et al. Snail accelerates cancer invasion by upregulating MMP expression and is associated with poor prognosis of hepatocellular carcinoma. Br J Cancer. 2005;92(2):252–8.
212. Zhao J, Dong D, Sun L, Zhang G, Sun L. Prognostic significance of the epithelial-to-mesenchymal transition markers e-cadherin, vimentin and twist in bladder cancer. Int braz j urol. 2014;40(2):179–89.

213. Knowles MA, Hurst CD. Molecular biology of bladder cancer: new insights into pathogenesis and clinical diversity. Nat Rev cancer. 2015;15(1):25–41.
214. Kim J, Hong SJ, Park JY, Park JH, Yu Y, Park SY, et al. Epithelial–mesenchymal transition gene signature to predict clinical outcome of hepatocellular carcinoma. Cancer Sci. 2010;101(6):1521–8.
215. Maglennon GA, Murphy S, Adams V, Miller J, Smith K, Blunden A, et al. Association of Ki67 index with prognosis for intermediate-grade canine cutaneous mast cell tumours. Vet Comp Oncol. 2008;6(4):268–74.
216. Cheang MCU, Chia SK, Voduc D, Gao D, Leung S, Snider J, et al. Ki67 index, HER2 status, and prognosis of patients with luminal B breast cancer. JNCI J Natl Cancer Inst. 2009;101(10):736–50.
217. Pasquier J, Abu-Kaoud N, Al Thani H, Rafii A. Epithelial to mesenchymal transition in a clinical perspective. J Oncol. 2015;2015.
218. Rafii A, Touboul C, Al Thani H, Suhre K, Malek JA. Where cancer genomics should go next: a clinician's perspective. Hum Mol Genet. 2014;23(R1):R69–75.
219. Celià-Terrassa T, Meca-Cortés Ó, Mateo F, De Paz AM, Rubio N, Arnal-Estapé A, et al. Epithelial-mesenchymal transition can suppress major attributes of human epithelial tumor-initiating cells. J Clin Invest. 2012;122(5):1849–68.
220. Korpal M, Ell BJ, Buffa FM, Ibrahim T, Blanco MA, Celià-Terrassa T, et al. Direct targeting of Sec23a by miR-200s influences cancer cell secretome and promotes metastatic colonization. Nat Med. 2011;17(9):1101.
221. Kalluri R, Neilson EG. Epithelial-mesenchymal transition and its implications for fibrosis. J Clin Invest. 2003;112(12):1776–84.
222. Sarrió D, Rodriguez-Pinilla SM, Hardisson D, Cano A, Moreno-Bueno G, Palacios J. Epithelial-mesenchymal transition in breast cancer relates to the basal-like phenotype. Cancer Res. 2008;68(4):989–97.
223. Elloul S, Vaksman O, Stavnes HT, Trope CG, Davidson B, Reich R. Mesenchymal-to-epithelial transition determinants as characteristics of ovarian carcinoma effusions. Clin Exp Metastasis. 2010;27(3):161–72.

224. Wells A, Yates C, Shepard CR. E-cadherin as an indicator of mesenchymal to epithelial reverting transitions during the metastatic seeding of disseminated carcinomas. Clin Exp Metastasis. 2008;25(6):621–8.
225. Saito T, Nagai M, Ladanyi M. SYT-SSX1 and SYT-SSX2 interfere with repression of E-cadherin by snail and slug: a potential mechanism for aberrant mesenchymal to epithelial transition in human synovial sarcoma. Cancer Res. 2006;66(14):6919–27.
226. Yang J, Eddy JA, Pan Y, Hategan A, Tabus I, Wang Y, et al. Integrated proteomics and genomics analysis reveals a novel mesenchymal to epithelial reverting transition in leiomyosarcoma through regulation of slug. Mol Cell Proteomics. 2010;9(11):2405–13.
227. Yang J, Du X, Wang G, Sun Y, Chen K, Zhu X, et al. Mesenchymal to epithelial transition in sarcomas. Eur J Cancer [Internet]. 2014;50(3):593–601. Available from: http://dx.doi.org/10.1016/j.ejca.2013.11.006
228. Fitzgerald MP, Gourronc F, Teoh MLT, Provenzano MJ, Case AJ, Martin JA, et al. Human chondrosarcoma cells acquire an epithelial-like gene expression pattern via an epigenetic switch: evidence for mesenchymal-epithelial transition during sarcomagenesis. Sarcoma. 2011;2011.
229. Zhang L, Lei W, Wang X, Tang Y, Song J. Glucocorticoid induces mesenchymal-to-epithelial transition and inhibits TGF-β1-induced epithelial-to-mesenchymal transition and cell migration. FEBS Lett. 2010;584(22):4646–54.
230. Niinaka Y, Harada K, Fujimuro M, Oda M, Haga A, Hosoki M, et al. Silencing of autocrine motility factor induces mesenchymal-to-epithelial transition and suppression of osteosarcoma pulmonary metastasis. Cancer Res. 2010;70(22):9483–93.
231. Li R, Liang J, Ni S, Zhou T, Qing X, Li H, et al. A mesenchymal-to-epithelial transition initiates and is required for the nuclear reprogramming of mouse fibroblasts. Cell Stem Cell. 2010;7(1):51–63.

232. Liao B, Bao X, Liu L, Feng S, Zovoilis A, Liu W, et al. MicroRNA cluster 302–367 enhances somatic cell reprogramming by accelerating a mesenchymal-to-epithelial transition. J Biol Chem. 2011;286(19):17359–64.
233. Lahat G, Zhu Q-S, Huang K-L, Wang S, Bolshakov S, Liu J, et al. Vimentin is a novel anti-cancer therapeutic target; insights from in vitro and in vivo mice xenograft studies. PLoS One. 2010;5(4):e10105.
234. Saito T, Oda Y, Kawaguchi K, Sugimachi K, Yamamoto H, Tateishi N, et al. E-cadherin mutation and Snail overexpression as alternative mechanisms of E-cadherin inactivation in synovial sarcoma. Oncogene. 2004;23(53):8629–38.
235. Nakajima G, Patiño-Garcia A, Bruheim S, Xi Y, San Julian M, Lecanda F, et al. CDH11 expression is associated with survival in patients with osteosarcoma. Cancer Genomics-Proteomics. 2008;5(1):37–42.
236. Polyak K, Weinberg RA. Transitions between epithelial and mesenchymal states: acquisition of malignant and stem cell traits. Nat Rev Cancer. 2009;9(4):265–73.
237. Guo Y, Zi X, Koontz Z, Kim A, Xie J, Gorlick R, et al. Blocking Wnt/LRP5 signaling by a soluble receptor modulates the epithelial to mesenchymal transition and suppresses met and metalloproteinases in osteosarcoma Saos-2 cells. J Orthop Res. 2007;25(7):964–71.
238. Tian W, Wang G, Yang J, Pan Y, Ma Y. Prognostic role of E-cadherin and Vimentin expression in various subtypes of soft tissue leiomyosarcomas. Med Oncol. 2013;30(1):401.
239. Saad AG, Collins MH. Prognostic value of MIB-1, E-cadherin, and CD44 in pediatric chordomas. Pediatr Dev Pathol. 2005;8(3):362–8.
240. Adams VJ, Evans KM, Sampson J, Wood JLN. Methods and mortality results of a health survey of purebred dogs in the UK. J Small Anim Pract. 2010;51(10):512–24.
241. Abadie J, Hédan B, Cadieu E, De Brito C, Devauchelle P, Bourgain C, et al. Epidemiology, pathology, and genetics of histiocytic sarcoma in the Bernese mountain dog breed. J Hered. 2009;100(suppl_1):S19–27.

242. Moore PF. A Review of Histiocytic Diseases of Dogs and Cats. Vet Pathol. 2014;51(1):167–84.
243. Schlick K, Aigelsreiter A, Pichler M, Reitter S, Neumeister P, Hoefler G, et al. Histiocytic sarcoma–targeted therapy: novel therapeutic options? a series of 4 cases. Oncol Res Treat. 2012;35(7–8):447–50.
244. Fidel J, Schiller I, Hauser B, Jausi Y, Rohrer-Bley C, Roos M, et al. Histiocytic sarcomas in flat-coated retrievers: a summary of 37 cases (November 1998–March 2005). Vet Comp Oncol. 2006;4(2):63–74.
245. Hornick JL, Jaffe ES, Fletcher CDM. Extranodal histiocytic sarcoma: clinicopathologic analysis of 14 cases of a rare epithelioid malignancy. Am J Surg Pathol. 2004;28(9):1133–44.
246. Wellman ML, Krakowka S, Jacobs RM, Kociba GJ. A macrophage-monocyte cell line from a dog with malignant histiocytosis. Vitr Cell Dev Biol. 1988;24(3):223–9.
247. Fayyad A, Lapp S, Risha E, Pfankuche VM, Rohn K, Barthel Y, et al. Matrix metalloproteinases expression in spontaneous canine histiocytic sarcomas and its xenograft model. Vet Immunol Immunopathol. 2018;198:54–64.
248. Semenza GL. Oxygen sensing, hypoxia-inducible factors, and disease pathophysiology. Annu Rev Pathol Mech Dis. 2014;9:47–71.
249. Dabral S, Muecke C, Valasarajan C, Schmoranzer M, Wietelmann A, Semenza GL, et al. A RASSF1A-HIF1α loop drives Warburg effect in cancer and pulmonary hypertension. Nat Commun. 2019;10(1):2130.
250. Kolesnikov N, Hastings E, Keays M, Melnichuk O, Tang YA, Williams E, et al. ArrayExpress update—simplifying data submissions. Nucleic Acids Res. 2015;43(D1):D1113–6.
251. Brunner JM, Plattet P, Doucey MA, Rosso L, Curie T, Montagner A, et al. Morbillivirus glycoprotein expression induces ER stress, alters Ca 2+ homeostasis and results in the release of vasostatin. PLoS One. 2012;7(3):1–12.

252. Bhandary B, Marahatta A, Kim H-R, Chae H-J. An involvement of oxidative stress in endoplasmic reticulum stress and its associated diseases. Int J Mol Sci. 2013;14(1):434–56.
253. Zepeda AB, Pessoa Jr A, Castillo RL, Figueroa CA, Pulgar VM, Farías JG. Cellular and molecular mechanisms in the hypoxic tissue: role of HIF-1 and ROS. Cell Biochem Funct. 2013;31(6):451–9.
254. Ushio-Fukai M, Nakamura Y. Reactive oxygen species and angiogenesis: NADPH oxidase as target for cancer therapy. Cancer Lett. 2008;266(1):37–52.
255. Galadari S, Rahman A, Pallichankandy S, Thayyullathil F. Reactive oxygen species and cancer paradox: to promote or to suppress? Free Radic Biol Med. 2017;104:144–64.
256. Klaunig JE, Kamendulis LM, Hocevar BA. Oxidative stress and oxidative damage in carcinogenesis. Toxicol Pathol. 2010;38(1):96–109.
257. Yates B, Braschi B, Gray KA, Seal RL, Tweedie S, Bruford EA. Genenames. org: the HGNC and VGNC resources in 2017. Nucleic Acids Res. 2016;gkw1033.
258. Dalman MR, Deeter A, Nimishakavi G, Duan Z-H. Fold change and p-value cutoffs significantly alter microarray interpretations. In: BMC bioinformatics. Springer; 2012. p. S11.
259. Greenwood SK, Hill RB, Sun JT, Armstrong MJ, Johnson TE, Gara JP, et al. Population doubling: a simple and more accurate estimation of cell growth suppression in the in vitro assay for chromosomal aberrations that reduces irrelevant positive results. Environ Mol Mutagen. 2004;43(1):36–44.
260. Dahlgren C, Karlsson A, Bylund J. Intracellular neutrophil oxidants: from laboratory curiosity to clinical reality. J Immunol. 2019;202(11):3127–34.
261. Zhou J, Yu Q, Chng W-J. TXNIP (VDUP-1, TBP-2): a major redox regulator commonly suppressed in cancer by epigenetic mechanisms. Int J Biochem Cell Biol. 2011;43(12):1668–73.

262. Cha YJ, Baik JE, Rhee WJ. Inhibition of endoplasmic reticulum stress-induced apoptosis by silkworm storage protein 1. Biotechnol Bioprocess Eng. 2018;23(2):194–200.
263. Kaufman RJ. Stress signaling from the lumen of the endoplasmic reticulum: coordination of gene transcriptional and translational controls. Genes Dev. 1999;13(10):1211–33.
264. Malhotra JD, Kaufman RJ. The endoplasmic reticulum and the unfolded protein response. In: Seminars in cell & developmental biology. Elsevier; 2007. p. 716–31.
265. Szegezdi E, Logue SE, Gorman AM, Samali A. Mediators of endoplasmic reticulum stress-induced apoptosis. EMBO Rep. 2006;7(9):880–5.
266. Aga M, Bentz GL, Raffa S, Torrisi MR, Kondo S, Wakisaka N, et al. Exosomal HIF1α supports invasive potential of nasopharyngeal carcinoma-associated LMP1-positive exosomes. Oncogene. 2014;33(37):4613–22.
267. Marie JC, Saltel F, Jurdic P, Wild TF, Horvat B. Cell surface delivery of the measles virus nucleoprotein: a viral strategy to induce immunosuppression. J Virol. 2004;78(21):11952–61.
268. Lu W, Kang Y. Epithelial-Mesenchymal Plasticity in Cancer Progression and Metastasis. Dev Cell. 2019;49(3):361–74.
269. Lamouille S, Xu J, Derynck R. Molecular mechanisms of epithelial–mesenchymal transition. Nat Rev Mol cell Biol. 2014;15(3):178–96.
270. Dong Y, Kang H, Liu H, Wang J, Guo Q, Song C, et al. Myoferlin, a Membrane Protein with Emerging Oncogenic Roles. Biomed Res Int. 2019;2019.
271. Li R, Ackerman IV WE, Mihai C, Volakis LI, Ghadiali S, Kniss DA. Myoferlin depletion in breast cancer cells promotes mesenchymal to epithelial shape change and stalls invasion. PLoS One. 2012;7(6):e39766.

272. Lee C-C, Cheng Y-C, Chang C-Y, Lin C-M, Chang J-Y. Alpha-tubulin acetyltransferase/MEC-17 regulates cancer cell migration and invasion through epithelial–mesenchymal transition suppression and cell polarity disruption. Sci Rep. 2018;8(1):1–15.
273. Das S, Yu S, Sakamori R, Stypulkowski E, Gao N. Wntless in Wnt secretion: molecular, cellular and genetic aspects. Front Biol (Beijing). 2012;7(6):587–93.
274. Sun L, Liu T, Zhang S, Guo K, Liu Y. Oct4 induces EMT through LEF1/β-catenin dependent WNT signaling pathway in hepatocellular carcinoma. Oncol Lett. 2017;13(4):2599–606.
275. Todorovic V, Frendewey D, Gutstein DE, Chen Y, Freyer L, Finnegan E, et al. Long form of latent TGF-β binding protein 1 (Ltbp1L) is essential for cardiac outflow tract septation and remodeling. Development. 2007;134(20):3723–32.
276. Janda E, Nevolo M, Lehmann K, Downward J, Beug H, Grieco M. Raf plus TGF β-dependent EMT is initiated by endocytosis and lysosomal degradation of E-cadherin. Oncogene. 2006;25(54):7117–30.
277. Wang H fan, Wang S sha, Zheng M, Dai L ling, Wang K, Gao X lei, et al. Hypoxia promotes vasculogenic mimicry formation by vascular endothelial growth factor A mediating epithelial-mesenchymal transition in salivary adenoid cystic carcinoma. Cell Prolif. 2019;52(3):1–11.
278. Zhang X, Cheng Q, Yin H, Yang G. Regulation of autophagy and EMT by the interplay between p53 and RAS during cancer progression. Int J Oncol. 2017;51(1):18–24.
279. Yang B, Wang N, Wang S, Li X, Zheng Y, Li M, et al. Network-pharmacology-based identification of caveolin-1 as a key target of Oldenlandia diffusa to suppress breast cancer metastasis. Biomed Pharmacother. 2019;112:108607.
280. Prunier C, Howe PH. Disabled-2 (Dab2) is required for transforming growth factor β-induced epithelial to mesenchymal transition (EMT). J Biol Chem. 2005;280(17):17540–8.

281. Dragoi A-M, Swiss R, Gao B, Agaisse H. Novel strategies to enforce an epithelial phenotype in mesenchymal cells. Cancer Res. 2014;74(14):3659–72.
282. Volakis LI, Li R, Ackerman IV WE, Mihai C, Bechel M, Summerfield TL, et al. Loss of myoferlin redirects breast cancer cell motility towards collective migration. PLoS One. 2014;9(2):e86110.
283. Wojton J, Kaur B. Impact of tumor microenvironment on oncolytic viral therapy. Cytokine Growth Factor Rev. 2010;21(2–3):127–34.
284. Hanahan D, Weinberg RA. Hallmarks of cancer: The next generation. Cell [Internet]. 2011;144(5):646–74. Available from: http://dx.doi.org/10.1016/j.cell.2011.02.013
285. Pani G, Galeotti T, Chiarugi P. Metastasis: cancer cell's escape from oxidative stress. Cancer Metastasis Rev. 2010;29(2):351–78.
286. Van Horssen J, Schreibelt G, Drexhage J, Hazes T, Dijkstra CD, Van der Valk P, et al. Severe oxidative damage in multiple sclerosis lesions coincides with enhanced antioxidant enzyme expression. Free Radic Biol Med. 2008;45(12):1729–37.
287. Théry C, Witwer KW, Aikawa E, Alcaraz MJ, Anderson JD, Andriantsitohaina R, et al. Minimal information for studies of extracellular vesicles 2018 (MISEV2018): a position statement of the International Society for Extracellular Vesicles and update of the MISEV2014 guidelines. J Extracell vesicles. 2018;7(1):1535750.
288. Stephenson JR, Ter Meulen V. Antigenic relationships between measles and canine distemper viruses: comparison of immune response in animals and humans to individual virus-specific polypeptides. Proc Natl Acad Sci. 1979;76(12):6601–5.
289. Lal N, Puri K, Rodrigues B. Vascular endothelial growth factor B and its signaling. Front Cardiovasc Med. 2018;5:39.
290. Bry M, Kivelä R, Leppänen V-M, Alitalo K. Vascular endothelial growth factor-B in physiology and disease. Physiol Rev. 2014;94(3):779–94.

291. Li X, Lee C, Tang Z, Zhang F, Arjunan P, Li Y, et al. VEGF-B: a survival, or an angiogenic factor? Cell Adh Migr. 2009;3(4):322–7.
292. Abd-Aziz N, Stanbridge EJ, Shafee N. Newcastle disease virus degrades HIF-1α through proteasomal pathways independent of VHL and p53. J Gen Virol. 2016;97(12):3174.
293. Sun BC, Sun Y, Zhao XL, Liu YX, Zhang SW. Expressions and significance of E-cadherin and beta-catenin in synovial sarcoma. Zhonghua Zhong Liu Za Zhi. 2005;27(12):727–30.
294. Suster S. Epithelioid leiomyosarcoma of the skin and subcutaneous tissue: clinicopathologic, immunohistochemical, and ultrastructural study of five cases. Am J Surg Pathol. 1994;18(3):232–40.
295. Saito T, Oda Y, Yamamoto H, Kawaguchi K, Tanaka K, Matsuda S, et al. Nuclear β-catenin correlates with cyclin D1 expression in spindle and pleomorphic sarcomas but not in synovial sarcoma. Hum Pathol. 2006;37(6):689–97.
296. Sannino G, Marchetto A, Kirchner T, Grünewald TGP. Epithelial-to-mesenchymal and mesenchymal-to-epithelial transition in mesenchymal tumors: a paradox in sarcomas? Cancer Res. 2017;77(17):4556–61.
297. Fortier A-M, Asselin E, Cadrin M. Keratin 8 and 18 loss in epithelial cancer cells increases collective cell migration and cisplatin sensitivity through claudin1 up-regulation. J Biol Chem. 2013;288(16):11555–71.
298. Busch T, Armacki M, Eiseler T, Joodi G, Temme C, Jansen J, et al. Keratin 8 phosphorylation regulates keratin reorganization and migration of epithelial tumor cells. J Cell Sci. 2012;125(9):2148–59.
299. Sanghvi-Shah R, Weber GF. Intermediate filaments at the junction of mechanotransduction, migration, and development. Front cell Dev Biol. 2017;5:81.

300. Mendez MG, Kojima S, Goldman RD. Vimentin induces changes in cell shape, motility, and adhesion during the epithelial to mesenchymal transition. FASEB J. 2010;24(6):1838–51.
301. Seehusen F, Orlando EA, Wewetzer K, Baumgärtner W. Vimentin-positive astrocytes in canine distemper: A target for canine distemper virus especially in chronic demyelinating lesions? Acta Neuropathol. 2007;114(6):597–608.
302. Battaglia RA, Delic S, Herrmann H, Snider NT. Vimentin on the move: new developments in cell migration. F1000Research. 2018;7.